ACT LAUNCH Project No 299662

The LAUNCH project is funded through the ACT programme (Accelerating CCS Technologies, Horizon2020 Project No 299662).
Financial contributions have been made by Ministry of Economic Affairs and Climate Policy, the Netherlands; The Federal Ministry for Economic Affairs and Energy, Germany; Gassnova of Norway through the CLIMIT program; and the Department for Business, Energy & Industrial Strategy, UK, with extra funding from the US Department of Energy. All funders are gratefully acknowledged.

Netherlands Enterprise Agency

Supported by: Federal Ministry for Economic Affairs and Energy on the basis of a decision by the German Bundestag

GASSNOVA

Department for Business, Energy & Industrial Strategy

LAUNCH

Lowering **A**bsorption process **UN**certainty, risks and **C**osts by predicting and controlling amine degradation

Deliverable Nr. D3.1.1

Effect of PZ degradation on corrosion of carbon and stainless steel

Dissemination level	Public	
Written By	Ching-Ting Liu (University of Texas)	Date: 04.01.2023
Checked by WP3 Leader	Hanna Knuutila (NTNU)	Date: 04.01.2023
Approved by the coordinator	Peter van Os (TNO)	Date: 04.01.2023
Issue date	04.01.2023	

The Dissertation Committee for Ching-Ting Liu Certifies that this is the approved version of the following Dissertation:

Corrosion of Stainless and Carbon Steel in Aqueous Piperazine for CO_2 Capture

Committee:

Gary T. Rochelle, Supervisor

Kyra L. Sedransk Campbell

John G. Ekerdt

Gyeong S. Hwang

Corrosion of Stainless and Carbon Steel in Aqueous Piperazine for CO_2 Capture

by

Ching-Ting Liu

Dissertation

Presented to the Faculty of the Graduate School of

The University of Texas at Austin

in Partial Fulfillment

of the Requirements

for the Degree of

Doctor of Philosophy

The University of Texas at Austin

August 2022

Dedication

To my family

Acknowledgements

I would like to first thank Dr. Rochelle. His knowledge, curiosity, and passion to research inspired me to learn, to stay curious, and to make contributions. His patience, warmth, and positive attitude towards life and family are the qualities I will always admire.

I would like to thank my committee members: Dr.'s Kyra Sedransk Campbell, John Ekerdt, and Gyeong Hwang. They provided important feedback to my work and many insightful questions. I also appreciate working with Dr. Eric Chen and Dr. Fred Closmann. They were never hesitant to share with others their knowledge and experience in academia and industry. Thanks to Maeve Cooney for proofreading my reports and taking care of all the administrative issues before I even noticed that they existed.

My graduate study would not be successful without interactions with the Texas Carbon Engineers in the Rochelle research group. I would like to thank Dr. Kent Fischer, whose work I inherited. He trained me how to design and fabricate experimental equipment to get valuable corrosion data. He also trained me how to work safely and responsibly in labs and pilot plants. I also want to thank former and current group members: Dr. Ye Yuan, Dr. Paul Nielsen, Dr. Tianyu Gao, Dr. Korede Akinpelumi, Dr. Yuying Wu, Joe Selinger, Athreya Suresh, Miguel Abreu, Benjamin Drewry, Chih-I Chen, Ariel Plantz, Jorge Marteroll, and James Obute. I was very lucky to know and have worked with them. They have been not only colleagues but also great friends for the past five years.

I would like to thank Tony Wu, Graham Bingham, Laura Uhrig and all the engineers and operators at the National Carbon Capture Center pilot plant. Thanks also to Dr. Frank Seibert, Juan-Ramon Campos, Robert Montgomery, and all the personnel at the UT Separations Research Program.

I am also grateful for the assistance of Dr. Andrei Dolocan with scanning electronic microscopes and surface profilometers, Dr. Vincent Lynch with X-ray diffraction, and Shallaco McDonald and David Gray for assistance in fabricating equipment.

I gratefully acknowledge the financial support from our sponsors in the Texas Carbon Management Program, US Department of Energy, CCP4, and the LAUNCH project.

Finally, I would like to thank my family. Even though the pandemic has kept us apart physically, your love has always been with me. Without your love and support, all of this would not have been possible.

Abstract

Corrosion of Stainless and Carbon Steel in Aqueous Piperazine for CO_2 Capture

Ching-Ting Liu, Ph.D.

The University of Texas at Austin, 2022

Supervisor: Gary T. Rochelle

Current obstacles that prevent commercial implementation of amine-scrubbing CO_2 capture are the high costs. Reducing capital costs by appropriate selection of construction materials, which requires knowledge of material corrosion performance for the process, will improve the economic feasibility of this technology.

Corrosion was evaluated in three pilot plant campaigns using aqueous piperazine with the Advanced Stripper (PZAS). 316L stainless steel (SS) experienced higher corrosion than 304 SS and 2205 duplex SS, and the corrosion rate showed strong dependence on the temperature. 304 and 2205 performed well at all locations and should be good construction materials for PZAS. Degraded PZ exacerbated 316L corrosion, and removal of PZ degradation products using a carbon adsorption bed significantly reduced corrosion. Carbon steel (CS) corrosion showed a weak temperature effect because the corrosion was more dependent on the protective siderite film. The protectiveness of the films was related to fluid velocity. Ni-based alloys corroded in PZ, and the rate increased with temperature.

Corrosion of C1010 CS and SS (304, 316L, 430) was measured at absorber and water wash conditions on the bench-scale. Corrosion rate decreases with increasing PZ.

With more than 0.003 m PZ in solution, CS has acceptable corrosion performance. Corrosion of CS increases with increasing partial pressure of CO_2, suggesting loading is another dominant parameter for carbon steel corrosion. Temperature has a less significant effect than PZ concentration and loading. CS corrosion increases with increasing flow velocity at both absorber and water wash conditions. SS had little corrosion at this lower temperature.

Performance of siderite ($FeCO_3$) protective films on CS was studied at representative stripper conditions on the bench-scale. Siderite films can deposit on the surface of CS in CO_2-loaded PZ solution at temperatures >100 °C and protect CS from corrosion. The protection may fail in degraded PZ. Ethylenediamine (EDA) is one of the major contributors for the loss of film protectiveness or can be the surrogate for the effect of PZ degradation on siderite film protection. A link between protectiveness and the apparent density of siderite films was discovered. The apparent density of siderite films decreases with increasing flow velocity and decreasing CO_2 loading, resulting in higher corrosion of CS.

Table of Contents

List of Tables

List of Figures

Chapter 1: Introduction

1.1 POST-COMBUSTION CO_2 CAPTURE (PCCC)

The atmospheric CO_2 concentration, which is strongly related to the average global temperature, has been rising steadily since industrialization. According to the Intergovernmental Panel on Climate Change (IPCC), emissions of greenhouse gas due to human activities are likely responsible for about 1 °C of global warming above pre-industrial levels. The increase in global temperature is likely to reach 1.5 °C before 2050 if it continues to increase at the current rate (IPCC, 2018). Rise in global temperature can cause several negative effects including loss of human habitat due to rise of sea level, reduction of major crops production, reduction of fresh surface and underground water, and loss of marine biodiversity. Significant reductions in greenhouse gas emissions are required to prevent the worst effects of global warming.

Post-combustion CO_2 capture (PCCC) systems separate CO_2 from the flue gas produced by combustion of fossil fuels. As the second largest emission source of CO_2 in the US, electricity generation accounted for more than 25% of CO_2 emissions in 2019. Although the complete transition from burning fossil fuels to the use of renewable clean energy is the long-term goal, PCCC technologies allow for the continued use of fossil fuels, a smoother transition, and a continuing reliable back-up for renewable fuels. Removing CO_2 from the flue gas from coal- and gas-fired power plants is particularly attractive because these emissions are from relatively few and concentrated point sources.

1.1.1 CO_2 Capture using Amine-Scrubbing

Amine-scrubbing has been used to remove acid gases from large gas point sources since 1930 (Bottoms, 1930). It is currently the most mature and promising technology for PCCC because of its long history in natural gas sweetening and the flexibility of retrofitting to existing power plants. Recent demonstration projects have demonstrated the feasibility of using amine scrubbing in medium and large-scale PCCC plants: the Boundary Dam plant in Canada captures CO_2 from a 110 MW coal-fired power plant (Preston et al., 2018) and the Petra Nova plant near Houston captures from a slipstream equivalent to 240 MWe from a coal-fired plant (Kennedy, 2020).

1.1.2 Piperazine with the Advanced Stripper (PZAS)

Aqueous piperazine (PZ) is considered a better solvent than the current benchmark monoethanolamine (MEA) solvent for PCCC due to its high absorption rate, low energy requirement for regeneration, and excellent thermal stability (Rochelle et al., 2011). The use of the Advanced Stripper along with PZ enhances the energy performance and provides an opportunity to reduce operating costs (Rochelle et al., 2019).

Figure 1-1 shows a simplified flow diagram of the PZAS (piperazine with advanced stripper) process. Flue gas containing 4–12% CO_2 from coal-fired or natural gas-fired boilers enters the absorber from the bottom. The 5 m PZ comes in from the top and contacts the flue gas counter-currently in the absorber. The absorber operates at low temperature (~40 °C) to ensure sufficient driving force for CO_2 mass transfer from the gas phase into the liquid phase. The CO_2-stripped gas then flows through a water wash column, which mitigates amine emissions and controls water balance of the entire system. The CO_2-rich

solvent first goes through heat exchangers and then is sent to the stripper for regeneration. The high temperature (~150 °C) in the stripper reverses the adsorption reactions, releasing CO_2 from the liquid to the gas phase. Steam is usually the heat source for an amine-scrubbing process. The released gas stream from the solvent, which contains mostly CO_2 and water, is first cooled to condense out water, and then the pure CO_2 is compressed to 150 bar for future transportation and storage. The regenerated, hot lean solvent is sent to exchangers to exchange heat with the cold rich solvent to recover some sensible heat. Before going back to the absorber top to start the next cycle, the lean solvent is cooled by a trim cooler to remove any excess heat.

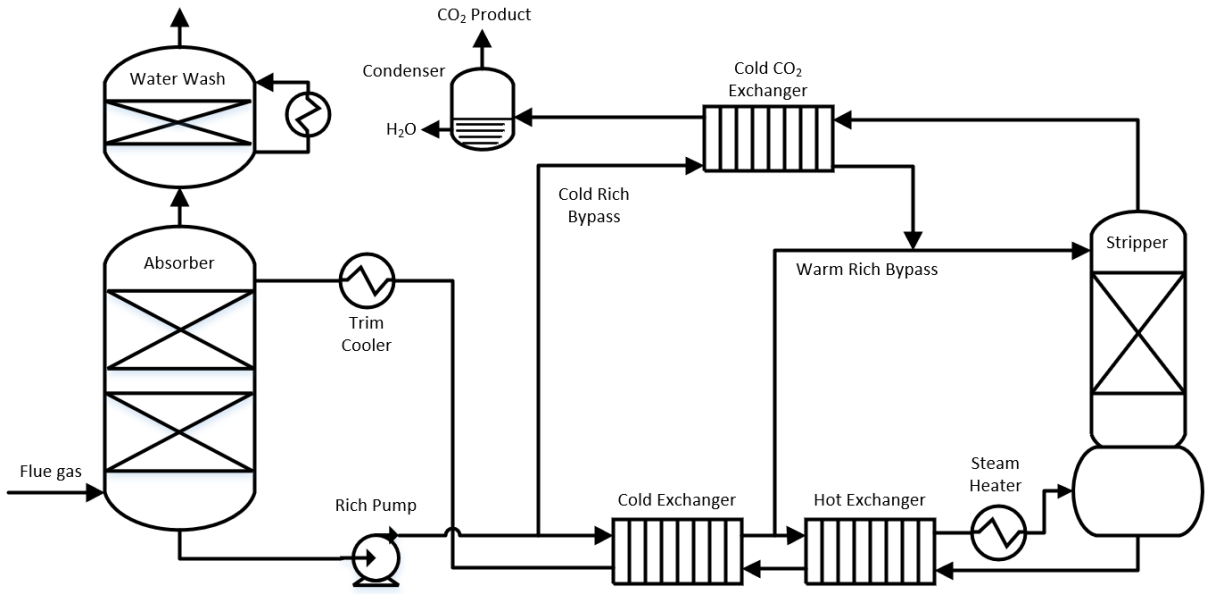

Figure 1-1: Simplified process flow diagram for PZAS

1.1.3 Motivation for Corrosion Study for PCCC

The main challenges for the commercialization of PCCC using amine-scrubbing are the energy and capital costs. PZ has demonstrated its better energy performance as a solvent for CO_2 capture than MEA. The energy requirement of a PZAS system measured at pilot plants is as low as 2.1 to 2.5 GJ/MT CO_2 (Chen et al. 2017; Rochelle et al. 2019), much lower than the energy requirements for systems using MEA (3.6 to 4.0 GJ/MT CO_2) (Cousins et al., 2012). Significant improvements in the energy performance of PCCC will be difficult because extensive solvent selection and process optimization have been done, and the thermodynamic efficiency of the overall process is already high (>50 %) (Lin et al., 2016). Further improvement in economic feasibility will need to come from reducing capital costs. Capital cost is largely affected by the selection of construction materials, in which appropriate corrosion performance of materials is often a major consideration. Reducing capital costs through optimal choices of construction materials requires thorough understanding of material corrosion behavior in these systems.

Corrosion may also cause some operational issues of a PCCC plant. As CS or SS corrodes, dissolved metals (Fe, Cr, Ni, Mn, etc.) may accumulate in the solvent, posing risks of contaminating the environment in the event of leakage or spill. Some metal ions may catalyze amine solvent degradation, resulting in more frequent solvent replacement required to maintain good capture performance and higher costs of disposing of the degraded solvent. Good understanding of corrosion in the system can help prevent these operational issues.

1.2 CORROSION STUDY FOR PCCC

Stainless steel construction for a post-combustion CO_2 capture (PCCC) unit is chosen largely based on experience with concentrated aqueous monoethanolamine (MEA). Piperazine (PZ), as a secondary amine, has intrinsically lower corrosivity than primary amines like MEA (Kohl et al., 1997; Gunasekaran et al., 2013; Gunasekaran et al., 2017). A protective siderite ($FeCO_3$) layer has been reported to form on CS in several second-generation amines at elevated temperature (Zheng et al., 2014a; Zheng et al., 2014b; Campbell et al., 2016). CS A106 coupons exposed to PZ at 80 °C show a tight, coherent layer of $FeCO_3$, but coupons exposed to MEA show a porous, loose layer of Fe_3C. (Zheng et al., 2014a). Fischer (2019) proposed that siderite film formation is promoted at high temperature, high loading, and in amines with low Fe^{2+} solubility. It explains the frequent observation of siderite films in hot PZ in the stripper but not the absorber. It also explains the lack of siderite in MEA because of higher Fe^{2+} solubility in MEA.

Siderite protective films were also observed in methyldiethanolamine (MDEA) and 2-amino-2-methyl-1-propanol (AMP) (Campbell et al., 2016; Yu et al., 2016). Some researchers have found that the addition of degradation products and oxygen in MDEA leads to the breakdown of the protective film, which causes high corrosion of unprotected CS substrate. The breakdown of films was attributed to the strong chelation between Fe^{2+} and degradation products, which reduces the activity of Fe^{2+} and $FeCO_3$ formation (Xiang, et al., 2014). The loss of film protectivity may also be caused by other parameters, such as CO_2 loading, temperature, and liquid velocity. More understanding of the mechanism of $FeCO_3$ film formation and the relationship between film protectivity and process conditions in PZ is necessary to determine if CS is an appropriate material.

Most of the current PCCC pilot plants are constructed with stainless steel with the assumption that stainless steel is always passivated at the operating conditions based on the previous experience with MEA. However, bench-scale study shows that stainless steel can be de-passivated and attacked at high temperature, O_2 depleted conditions in PZ (Fischer et al., 2017). The high corrosion rate of stainless steel may be due to the higher operating temperature in a PZAS system (150 °C) than in a traditional MEA system. The active/passive behavior of stainless steel depends on the redox potential of the solution, which can be affected by the amount of O_2 dissolved and other charge-transfer reactions occurring in the solution. However, until more understanding of SS corrosion in PZ is obtained, PZ units cannot be built with stainless steel or should be operated with considerable care. Other alloys, such as duplex stainless steel and Ni-based alloys, should also be evaluated as alternative construction materials.

In the absence of dissolved O_2, the conversion of dissolved metal ions from higher to lower oxidation states, such as Fe^{3+} to Fe^{2+}, has been suggested as the cause of PZ oxidative degradation (Nielsen, 2018). This hypothesis was supported by the observation of corrosion products in previous pilot plants using PZ where Fe^{3+} products were seen in the rich amine streams, and Fe^{2+} products were seen in the lean amine stream after Fe^{3+} ions had oxidized PZ (Fischer, 2019). Therefore, although higher dissolved Fe in PZ solution is preferred for faster formation of siderite protective films, it may accelerate PZ oxidation because of the increased amount of oxygen carriers in the solvent. The increase in carried-over oxygen may have an opposite effect on SS corrosion because more oxidizing solvent may reduce the risk of SS de-passivation (Fischer, 2019). In addition to the dissolved Fe concentration, other operations related to mitigation of PZ oxidation—for

example, removal of dissolved O_2 by N_2 sparging, reduced residence time in hot piping and stripper sump, and removal of NO_2 from the flue gas—may also alter the corrosion environment. The effects of these operations will need to be evaluated in long-term pilot testing because they are difficult to be performed in simpler bench-scale corrosion apparatus.

Corrosion results from previous pilot-scale testing have demonstrated that CS shows good performance in a PZAS absorber (Fischer, 2019). Even without the siderite protective layer that was only observed in the Advanced Stripper at high temperature (120–155 °C), CS generally showed acceptable corrosion performance (<300 μm/yr) in the absorber area at pilot plants. However, to ensure smooth operation of pilot plants, the flexibility of adjusting parameters independently was limited. Corrosion data were collected only at a handful of sets of conditions, and correlations between corrosion and each process variable, such as temperature, CO_2 loading, flow velocity, and PZ degradation could not be established based on only the pilot-scale data. In addition to the lack of correlation between corrosion and process variables at absorber conditions, there are few corrosion data for the water wash of an amine-scrubbing system available in the literature. The presence of PZ can result in increased pH, which is expected to lower the solution corrosivity. To better understand the corrosion performance and provide material recommendations for the absorber and water wash in PZAS, corrosion measurements need to be performed on the bench-scale where each variable can be tuned over a wider span.

1.3 RESEARCH OBJECTIVES

1.3.1 Measure corrosion at representative conditions in pilot plants and identify correlations between corrosion and critical process parameters.

- Quantify the corrosion performance of stainless and carbon steel in PZAS pilot plants to understand the effect of temperature, loading, and fluid velocity on SS and CS corrosion
- Study the relationship between corrosion and PZ oxidation. Evaluate effect of PZ oxidation mitigation on corrosion in long-term pilot testing.
- Evaluate performance of alternative materials, including duplex stainless steel and Ni-based alloys.

1.3.2 Understand mechanism of carbon steel protection by $FeCO_3$ films in PZ.

- Evaluate the effect of process parameters, including temperature and loading, on film protectivity using corrosion measurement and surface characterization of corrosion coupons using bench-scale apparatuses.
- $FeCO_3$ films were usually found in PZ at elevated temperature but sometimes failed to protect carbon steel when PZ degradation exceeds a critical level. Quantify the relationship between PZ degradation and film protectivity and identify degradation products that cause the loss of protection.
- Liquid flow rate appears to affect the protectivity of $FeCO_3$ films in pilot plants. Construct a new bench-scale corrosion apparatus to enable control on the liquid flow rate inside the loop along with other process parameters.

1.3.3 Evaluate carbon steel corrosion in the absorber and water wash of PZAS where siderite films are normally not present.

- Measure CS corrosion at absorber and water wash conditions on the bench-scale to quantify the effect of PZ concentration, temperature, loading, and flow velocity on CS corrosion in the low temperature region of PZAS.

1.3.4 Recommend material selection for each part of the PZAS process.

- Identify any process conditions in PZAS that cause acute corrosion failure based on the bench- and pilot-scale corrosion data.
- Determine the process conditions under which it is safe to use CS or SS in a PZ system.
- Recommend acceptable materials of construction for each unit operation for PZAS.

Chapter 2: Corrosion in PZAS at Pilot Plants[1]

This chapter describes the corrosion study with the PZAS process during three pilot plant campaigns: NCCC 2018 campaign, NCCC 2019 campaign, and SRP 2021 campaign. Details of each pilot campaign are given in the following sections of this chapter. The corrosion study in the NCCC 2018 campaign was done by Fischer (2019), and the results were incorporated with those from the NCCC 2019 campaign and published as a peer-reviewed paper in Industrial & Engineering Chemistry Research with the dissertation author as the primary author (Liu et al., 2020). Corrosion study during the NCCC 2019 and SRP 2021 was the original work by the author.

2.1 Literature Review on Corrosion at PCCC Pilot Plants

2.1.1 Corrosion in Pilot Plants Using MEA

Evaluation of aqueous monoethanolamine (MEA) for post-combustion carbon capture (PCCC) at the pilot scale has been performed at several locations worldwide. This section provides summaries of published corrosion data from four pilot plants using 30 wt % MEA.

The CASTOR CO_2 capture pilot plant in Denmark captured CO_2 from a nearby coal-fired power plant. The facility had a capacity of approximately 1 ton CO_2 per hour. Corrosion was evaluated in two campaigns using 30 wt % MEA in 2006. Corrosion measurements were performed with corrosion coupons at absorber inlet lean solvent, absorber outlet lean solvent, stripper inlet rich solvent, and stripper outlet lean solvent. The

[1]Part of this chapter has been published in "Liu C-T, Fischer KB, Rochelle GT. Corrosion by Aqueous Piperazine at 40 – 150 °C in Pilot Testing of CO_2 Capture. Ind Eng Chem Res. 2020;59;7189 – 7197" with Liu as the primary author.

highest corrosion rate of carbon steel (C1018) was 4500 to 8500 μm/yr in the stripper outlet lean solvent. Although the high corrosion rate was attributed to the high temperature (115 °C) at the stripper outlet, carbon steel performed very well (4 μm/yr) in hot rich solvent entering the stripper. 316L and 304L stainless steels were resistant to corrosion (<5 μm/yr) at all the test locations (Kittel et al., 2009).

A pilot plant at the International Test Center (ITC), University of Regina, used electrical resistance measurement to monitor carbon steel corrosion in 30 wt % MEA (Kittel et al., 2009). The plant captured 1 ton CO_2 per day from a natural gas burner. Flue gas with 4% and 8% CO_2 was used during the campaign. Carbon steel corrosion was highest in the rich solvent entering the stripper (1075 μm/yr) during the period using flue gas with 8% CO_2, followed by stripper overhead (538 μm/yr). In the hot lean solvent, where the highest carbon steel corrosion was measured at the CASTOR plant, the rate measured at ITC was less than 50 μm/yr. Although the results from the two pilot plants did not perfectly agree, they suggest that the worst MEA corrosion is expected at high temperature (110–120 °C). The second highest carbon steel corrosion rate was measured in stripper overhead (538 μm/yr), most likely caused by the hot CO_2 and water vapor. In addition to the effect of temperature, the contributions of species in the solvent were discussed. A correlation between carbon steel corrosion rate (CR) measured in the liquid phase and several parameters, including temperature (T) and concentrations of MEA ([MEA]), total CO_2 ([CO_2]), and O_2 ([O_2]) in the liquid, is shown by Equation 2-1. According to the power order, regardless of the temperature, MEA concentration has more of an impact on the corrosion rate than CO_2 and O_2.

$$\ln(CR) = 19 - 8963 \times \frac{1}{T} + 3.3 \ln[MEA] + 2.4 \ln[CO_2] + 0.003 \ln[O_2] \quad (2\text{-}1)$$

Several stainless steels and Ni-based alloys were tested at a pilot plant using 30 wt % MEA operated by RWE Power (Moser et al., 2011). The plant captured 7.2 tons of CO_2 per day from a lignite-fired power plant. The materials tested included austenitic stainless steel 1.4541 (similar to 316L) and 1.4571 (SS321), duplex stainless steel 2205, and Ni alloy 825. All of the tested materials had excellent corrosion performance. The corrosion rate measured with coupons was less than 1 μm/yr everywhere. They also reported that no localized corrosion was observed on the tested materials.

The 2017 MEA campaign at the National Carbon Capture Center (NCCC) had similar corrosion results to those from the three plants above: 1. carbon steel corrosion was most severe (3500~4000 μm/yr) at high temperature locations (stripper sump), and it generally performed well in the absorber and cold streams; and 2. stainless steel showed great resistance to corrosion at all locations (Fischer, 2019).

A summary of corrosion results from the four pilot plants is given in Table 2-1. Based on these results, it can be concluded that for a capture plant using 30 wt % MEA, carbon steel is suitable only at low temperature locations. In the stripper area, either high alloys, such as stainless steels and Ni-based alloys, are required for the construction, or other corrosion mitigation methods need to be applied along with carbon steel construction.

Table 2-1: Summary table of corrosion at CCS pilot plants using 30 wt % MEA (Kittel et al., 2009; Moser et al., 2011; Fischer, 2019)

Pilot Plant	**CASTOR**	**ITC**	**RWE**	**NCCC**
Year	2006	2007	2009	2017
Flue gas source	Coal-fired power plant	Natural gas burner	Lignite-fired power plant	Coal-fired power plant
Capture capacity (ton CO_2/day)	24	1	7.2	9.6
CO_2 content in flue gas	12%	4%, 8%	14.2%	12%
Absorber Temperature (°C)	40	46	40	40–70
Stripper Temperature (°C)	116	118	120	110–120
Highest corrosion of CS	4500 µm/yr at hot lean piping (hot rich coupons lost during batch period)	1075 µm/yr at hot rich piping	-	3500 µm/yr at stripper sump & hot rich inlet separator
Corrosion of high alloys	304L, 316L stainless steel, 2205 duplex stainless steel, and Ni alloy 825 showed no sign of corrosion.			

2.1.2 Interaction between Corrosion and Solvent Degradation at Pilot Plants

The relationship between corrosion and solvent degradation was studied during pilot testing performed at the TNO CCS facility in Maasvlakte, the Netherlands (Khakharia et al., 2015). The facility processed the flue gas from a coal-fired power plant and captured up to 6 tons CO_2 per day using 30 wt % MEA. Corrosion of 304 and 316L stainless steel was measured using LPR probes in the hot lean solvent stream, and the rate of solvent degradation was monitored by measuring NH_3 emissions in the gas stream leaving the water wash. Increase in 316L corrosion rate and NH_3 emission was observed during the period when the pilot plant operated with a synthetic flue gas. The initial increase in corrosion and MEA degradation rates was attributed to the high O_2 content in the flue gas (17%). Corrosion and solvent oxidation were further catalyzed by the dissolved metals and accumulated degradation products and resulted in a tremendous increase in degradation in the later period.

Oxidation inhibitors can sometimes act as corrosion inhibitors at PCCC conditions. The inhibition of carbon steel corrosion by SO_2/SO_3^{2-} was studied in a pilot-scale process by Gao et al. (2011). The pilot system used a proprietary amine solvent blend specified by Toshiba and a synthetic flue gas containing 12% CO_2, 18% O_2, and 214 ppm SO_2. SO_2 in aqueous amine can oxidize to SO_3^{2-}, which can further react with O_2 to form SO_4^{2-}. Therefore, SO_2/SO_3^{2-} can act as an oxygen scavenger and mitigate solvent oxidation. SO_2 in flue gas was found to reduce carbon steel corrosion in the hot rich solvent line but not significantly. The corrosion rate of carbon steel in the cold rich amine stream increased slightly when SO_2 was present in the flue gas, and the increase was attributed to the lower pH of the solvent due to SO_2 oxidation and the higher Fe solubility due to chelation by heat

stable salts. The authors concluded that SO_2/SO_3^{2-} only had a minor effect on carbon steel corrosion.

The effect of SO_3^{2-} on corrosion was also studied at the pilot plant using 30 wt % MEA at Technology Centre Mongstad (TCM), Norway (Flø et al., 2019). Corrosion of carbon steel (CS235) was evaluated by weight loss analysis. The highest corrosion rate measured was above 6000 μm/yr in hot rich solvent. Other evaluated metals, including SS316L, 22Cr duplex, and 25Cr duplex steels, all had good performances everywhere. Although no stainless steel corrosion was measured by coupon weight loss, the plant experienced reboiler failure due to severe corrosion on the heat exchanger internals made of 316L stainless steel during the SO_3^{2-} injection period. It was proposed that the high corrosion of 316L resulted from the extremely reducing solvent environment as SO_3^{2-} consumed a significant amount of O_2. The solvent de-passivated stainless steel by reducing and dissolving the Cr_2O_3 passive layer and exposing the vulnerable metal to the hot and corrosive environment. Another cause of severe corrosion in the reboiler could be the gas evolution which caused extra turbulence and resulted in erosion-corrosion on the surface of the exchanger plates.

2.2 CORROSION MEASUREMENTS IN PZAS AT PILOT PLANTS

The following sections describe the corrosion studies with PZAS at the pilot scale. Corrosion measurements were made at two pilot plants, one at the National Carbon Capture Center (NCCC) in Wilsonville, Alabama and the other at the Separations Research Program (SRP) in Austin, Texas.

Corrosion was evaluated at the NCCC pilot plant between February and August 2018 (the NCCC 2018 campaign). The NCCC pilot unit captures CO_2 from a 0.6 MWe equivalent coal flue gas stream using fresh 5 m (30 wt %) aqueous PZ. The PZ solvent was prepared onsite and loaded with CO_2 using the flue gas from a coal-fired power plant. Corrosion was then evaluated in another pilot campaign at NCCC between February and June 2019. During this campaign (the NCCC 2019 campaign), the pilot unit operated with a synthetic flue gas from coal flue gas and air to simulate the CO_2 concentration in the flue gas from a power plant powered with natural gas combined cycle (NGCC). The NGCC flue gas contained 4.3% CO_2 and 15% O_2. The solvent was the inventory of 5 m PZ retained from the NCCC 2018 campaign. Detailed operating conditions and analyses for the two campaigns at NCCC have been published (Gao et al., 2019; Rochelle et al., 2019; Rochelle et al., 2021; Wu et al., 2021). The corrosion results during the two campaigns at NCCC have been published in a peer-reviewed journal (Liu et al., 2020).

Corrosion was evaluated at the SRP pilot plant between September 2021 and February 2022. The plant used a synthetic flue gas (air with added 4.3% CO_2) and 5 m PZ. The PZ solvent was from the same batch of solvent prepared for the NCCC 2018 campaign. The inventory had briefly undergone 264 hours of operation during other pilot campaigns before the SRP 2021 campaign and was reasonably fresh when the SRP campaign started. Corrosion study in the campaign focused on the interaction between corrosion and several PZ oxidation mitigation methods.

2.2.1 Coupon Weight Loss Measurements

Corrosion coupons were used for corrosion rate measurements by weight loss and for corrosion product analysis. Strip coupons (Metal Samples CO118 series) and disc coupons (Metal Samples CO220 series) were use in this study.

The procedures of installing coupons and coupons holders have been well documented by Fischer (2019). Once removed, coupons are rinsed with deionized water and acetone, photographed, and analyzed by a scanning electron microscope/energy dispersive X-ray spectroscopy and a surface profilometer. Afterward, corrosion products were scraped off and analyzed by powder X-Ray diffraction. After all surface characterization was done, residual corrosion products were removed using concentrated HCl inhibited with N,N'-Dibutylthiourea as recommended in literature (Kayafas, 1980; NACE, 2013). The cleaning procedures were repeated on coupons several times. The weight loss was determined after each cleaning cycle until no significant mass change occurred, and a final weight loss of the coupon was recorded.

After the corrosion products were removed, a final weight loss of coupons was measured. Finally, corrosion rate was calculated from the weight loss using Equation 2-2.

$$CR = 87600\ \frac{W}{DAT} \tag{2-2}$$

where:

CR = corrosion rate (μm/yr)

W = coupon mass loss (mg)

D = density of metal (g/cm^3)

A = surface area of coupon (cm^2)

T = duration of experiment (hours)

The factors that can produce errors in weight loss measurement include inadequate balance precision, improper corrosion product removal or overcleaning, and inaccurate exposure time. The balances used can determine mass values to 0.1 mg, which is at least one order of magnitude smaller than the typical weight loss of coupons that were considered corroded (>300 μm/yr). The precision of weight loss measurement can also be improved by acquiring higher accumulative weight loss over longer exposure time. Inadequate corrosion product removal or overcleaning may affect the accuracy of weight loss measurement and can be avoided by repetitive short cleaning steps. The exposure time can usually be well controlled to in most laboratory procedures. However, at pilot plants, corrosive conditions can vary significantly, and the estimation of how long corrosive conditions existed can cause errors.

2.2.2 Corrosion Measurements at NCCC Pilot Plant

Corrosion measurements were made at various locations at the NCCC pilot plant. These locations are illustrated in Figure 2-1. In the absorber system, coupons were installed at five locations: in the absorber sump, between packing sections one and two, between packing sections two and three, at the absorber top, and in the cold lean solvent pipe. In the Advanced Stripper, coupon measurements were made at five locations: the cold rich bypass, the warm rich bypass, the hot rich stream, the hot lean stream, and the stripper sump. C1010 carbon steel, 304 stainless steel, and 316L stainless steel were evaluated in the 2018 campaign. During the 2019 campaign, 2205 duplex stainless steel, Hastelloy®

C276, and Inconel® 625 (I625) were evaluated in the Advanced Stripper in addition to carbon and stainless steels.

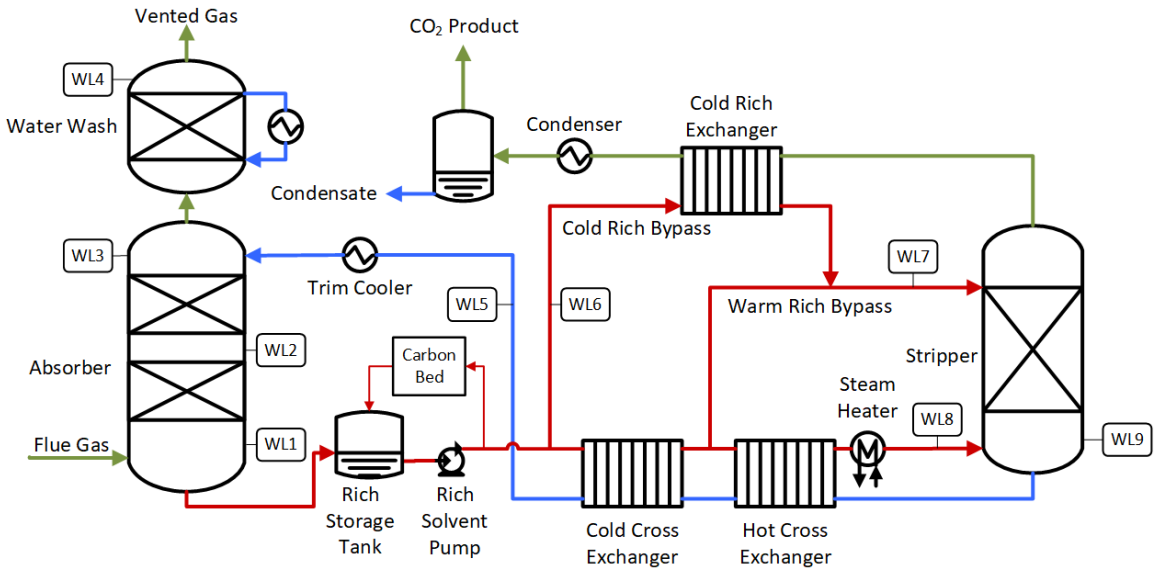

Figure 2-1. Process flowsheet of the NCCC pilot plant highlighting locations of coupon weight loss (WL) measurements: absorber sump (WL1), between absorber beds 1 and 2 (WL2), between absorber beds 2 and 3 (WL3), absorber top (WL4), cold lean stream (WL5), cold rich bypass (WL6), warm rich bypass (WL7), hot rich stream (WL8), stripper sump (WL9), and hot lean stream (WL10). (Liu et al., 2020)

In each campaign, coupons were installed and removed in four chronological batches. An illustration of the coupon batch period in the 2018 and 2019 campaign is given in Tables 2-2 and 2-3, respectively. In the 2018 campaign, the coupons in the absorber and in the Advanced Stripper were changed out at the same time while in 2019, only the ones in the Advanced Stripper were batched, and there was only one batch in the absorber throughout the campaign. A legacy activated carbon adsorption bed at NCCC was turned on May 14, 2019 and remained operating until the end of the campaign. The carbon bed was installed on a slip stream which drew 10–30% of the rich solvent after the rich solvent

pump and before the cold cross exchanger. The solvent after the carbon bed was then returned to the rich storage tank.

Table 2-2. Calendar illustration of coupon batches in the 2018 campaign[2] (Liu et al., 2020)

NCCC 2018 Campaign							
	February	March	April	May	June	July	August
Batch 1							
Batch 2							
Batch 3							
Batch 4							

Table 2-3. Calendar illustration of coupon batches in the 2019 campaign[3] (Liu et al., 2020)

NCCC 2019 Campaign						
		February	March	April	May	June
Absorber						
AFS	Batch 1					
	Batch 2					
	Batch 3					
	Batch 4					

2.2.3 Corrosion Measurements at SRP Pilot Plant

Figure 2-2 shows the process flow diagram (PFD) for the SRP pilot plant highlighting the locations where corrosion measurements are made. Four of the locations (absorber sump, cold lean stream, warm rich bypass, and hot lean stream) were legacy from previous pilot activities. Four new locations (cold rich stream, in-and-out intercooler loop,

[2] Green sections represent periods of piperazine operation, black sections represent periods when coupons were inserted but the plant was shut down, and the yellow section represents the period of simple stripper operation.

[3] Green sections represent periods of piperazine operation; black sections represent periods when coupons were inserted but the plant was shut down.

water wash (WW) circulation loop, and warm total bypass) were added for the SRP 2021 campaign to allow more data to be collected.

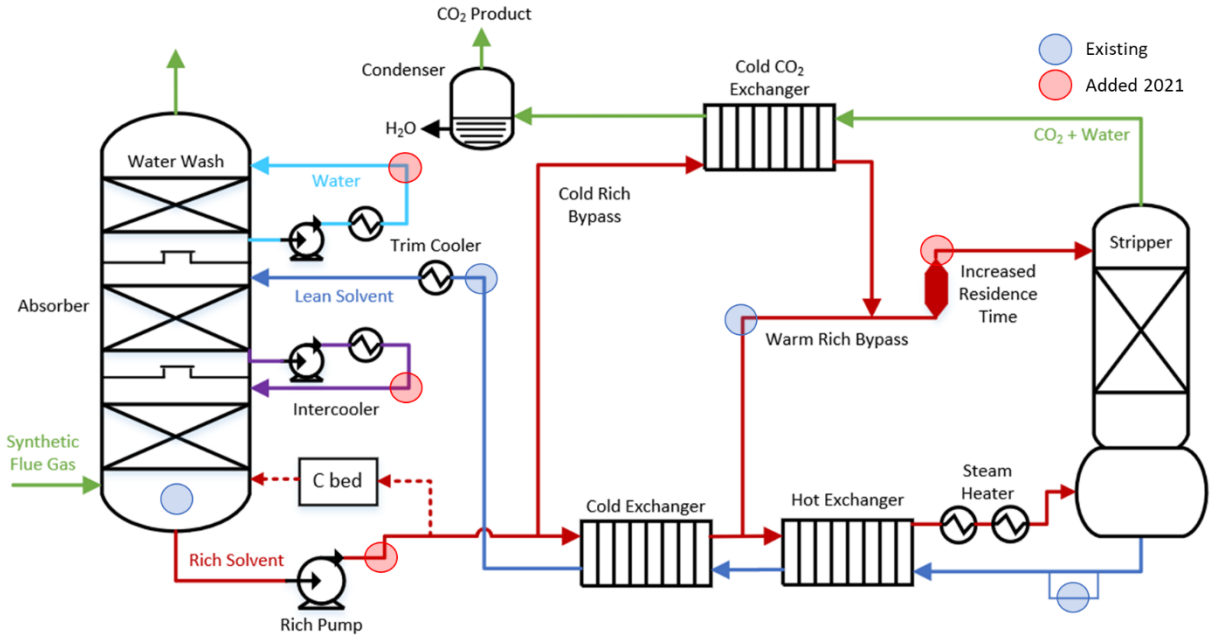

Figure 2-2: Process flow diagram for SRP pilot plant with corrosion testing locations

The SRP 2021 campaign aimed for the study of PZ oxidation, and several oxidation-related process operations, including NO_2 injection, N_2 sparging in the absorber sump, increased residence time in the warm rich bypass, and removal of PZ degradation products by carbon adsorption, were carried out during the campaign. Corrosion coupons were changed out when major operational changes were made to allow an investigation of corrosion under more consistent process condition and how corrosion reacts to the operational changes. A brief timeline of the 2021 SRP campaign operation and corrosion tests is given in Table 2-4. Six batches of coupons were evaluated. At the beginning of each

batch period, one fresh C1010 carbon steel coupon was installed at each location except the hot lean location, where one 304L and one 316L coupon were installed. The Batch 1 coupons evaluated corrosion by water during pre-commissioning, including troubleshooting equipment and heat loss measurements. This batch had been through 22 days of water operation between Sep 16 and Oct 29, 2021. Batches 2 and 3 experienced 121 and 40 hours of PZ operation, respectively, between Dec 14, 2021 and Jan 7, 2022, and the results are referred to as PZ baseline corrosion. Batch 4-1 was installed in the system on Jan 25, 2022 to evaluate corrosion during the period when 1 ppm of NO_2 was added to the flue gas. After 143 hours of plant operation, the Batch 4-1 coupons were removed on Feb 2, 2022, weighed, and cleaned with acid. The same batch of coupons was later reinstalled and underwent another 76 hours of operation with NO_2 (Batch 4-2). The Batch 5 coupons were in the system between Feb 14 and Feb 25, 2022. The warm rich bypass was switched over to the increased residence time mode on Feb 14, and N_2 sparging in the absorber sump was applied one day later. N_2 was turned off on Feb 19 and the warm bypass was left in the increased residence time mode through the end of the campaign. N_2 sparging effectively reduced the dissolved O_2 in the cold rich solvent from 7 ppm to 2 ppm, and the increased residence time in the warm bypass was supposed to increase the consumption of dissolved O_2. Therefore, during this period, the PZ solvent was expected to be more reducing, and the Batch 5 coupons evaluated corrosion under reducing conditions. A carbon bed was put into service between Feb 28 and Mar 4 to remove PZ degradation products. The Batch 6 coupons were installed on Feb 28 and stayed in the system for 99 hours to capture any change in corrosion that might result from the removal of degradation products. In addition to the six batches of coupons, there was one coupon

at each location which remained in the process throughout the entire campaign, and the results are referred to as long-term corrosion.

Table 2-4: Corrosion coupon batches during 2021 SRP campaign

Activity	**Tasks**	**Corrosion test**	**Duration**
Water testing	Checked for water leaks and instrument	Batch 1 Water corrosion	22 days
	Conducted heat loss measurement		
PZ baseline	Charged with 5 m PZ containing a Li tracer	Batch 2 & 3 PZ corrosion baseline	Batch 2: 121 hrs Batch 3: 40 hrs
	Operated with synthetic flue gas with 4.3% CO_2		
Operate with 1 ppm NO_2	1 ppm NO_2 in flue gas	Batch 4-1 Corrosion under oxidizing conditions	143 hrs
	1 ppm NO_2 in flue gas	Batch 4-2 Corrosion under oxidizing conditions	76 hrs
Test increased warm total bypass residence time and N_2 sparging	Operated with increased residence time piping and N_2 sparging in absorber sump	Batch 5 Corrosion under reducing conditions	71 hrs
	Turned off N_2 sparging. Continued operation with increased residence time.		121 hrs
Test carbon bed removal of degradation products	Pass slipstream (5–10%) through carbon bed	Batch 6 Corrosion with carbon bed	99 rs

2.3 RESULTS AND DISCUSSION

Corrosion measured in the absorber and the Advanced Stripper at NCCC is summarized in Tables 2-5 to 2-7, and the results from the SRP 2021 campaign are summarized in Tables 2-8 to 2-10. Process parameters, such as temperature and flow velocity, are also included in the tables. Temperatures were from the inline temperature sensor nearest to each corrosion measurement location. Flowrates were measured by inline flow meters, and the flow velocities were calculated by Equation 2-2. The flow in the absorber and stripper columns was minimal compared to the flow in the piping, so the flow velocity in the columns is assumed to be 0. The relationships between corrosion data and process parameters at the pilot plants are discussed in the following sections.

$$V = \frac{4Q}{\pi D^2} \tag{2-2}$$

where:

V = Flow velocity (m/s)

Q = Volumetric flowrate from inline flow measurements (m^3/s)

D = Pipe diameter at the corrosion measurement point (m)

Table 2-5: Summary table of corrosion measurements in the absorber at the NCCC pilot plant (Liu et al., 2020)

Campaign	Location	Batch Descriptor	Batch Operating Hours	Approx. Temperature (°C)	Flow Velocity (m/s)	Corrosion Rate (μm/yr)		
						316L	304	C1010
NCCC 2018	Absorber sump	2	388	50	0	0.5		0.9
		3	879	50	0		0.1	0
		4	363	50	0	0.6		0.6
	Bed 1-2	2	388	50	0			
		3	879	50	0	0.1		0.3
		4	363	50	0	0.5		0.2
	Absorber top	2	388	50	0			
		3	879	50	0			5
		4	363	50	0			
	Cold lean	2	388	50	0.50			
		3	879	50	0.50	0.4		108
		4	363	50	0.50	1		210
NCCC 2019	Absorber sump	-	1979	50	0	0		298
	Bed 1-2	-	1979	50	0	0.5		278
	Bed 2-3	-	1979	50	0	0.2	0.5	0.8
	Absorber top	-	1979	50	0	0.2	0.2	0
	Cold lean	-	1979	50	0.36	0.0	18	140

Table 2-6: Summary table of corrosion measurements in the Advanced Stripper during the NCCC 2018 campaign (Liu et al., 2020)

Campaign	Location	Batch Descriptor	Batch Operating Hours	Temperature (°C)	Flow Velocity (m/s)	Qualitative Loading	Corrosion Rate (μm/yr)		
							316L	304	C1010
NCCC 2018	Hot lean	2	388	146	0.53	lean	1095		711
		3	879	149	0.43	lean		0.5	49
		4	363	146	0.54	lean	1.8		184
	Hot rich	2	388	152	5.87	lean[4]	629		36
		3	879	154	5.73	lean		198	2729
		4	363	151	5.91	lean	1.9		9621
	Warm bypass	2	388	116	0.26	rich	9.0		55
		3	879	116	0.21	rich		0.3	47
		4	363	117	0.27	rich	1.2		92
	Cold bypass	2	388	48	0.05	rich	0.7		97
		3	879	50	0.05	rich		0.0	50
		4	363	50	0.05	rich	1.0		103
	Stripper sump	2	388	147	0	lean	489		0.2
		3	879	149	0	lean		0.6	11
		4	363	146	0	lean	4.4		

[4] The hot rich stream was flashing, and part of the CO_2 was in the gas phase; therefore, the liquid phase had a CO2 loading in the "lean" region.

Table 2-7: Summary table of corrosion measurements in the Advanced Stripper during the NCCC 2019 campaign (Liu et al., 2020)

Campaign	Location	Batch Descriptor	Batch Operating Hours	Temperature (°C)	Flow Velocity (m/s)	Qualitative Loading	Corrosion Rate (μm/yr)					
							316L	304	C1010	2205	C276	I625
NCCC 2019	Hot lean	1	225	150	0.44	lean	711			0.6	464	604
		2	390	139	0.60	lean		11	910		314	397
		3	400	150	0.55	lean	1429			1.0		
		4	964	150	0.54	lean	0.0	0.8		0.5		
	Hot rich	1	225	154	6.46	lean[5]	597			0.0	433	656
		2	390	144	5.72	lean		10	7431		0.0	0.0
		3	400	153	4.83	lean	417	0.1	4463	0.0		
		4	964	152	4.83	lean	0.0	0.0		0.0		
	Warm bypass	1	225	112	0.25	rich	112			0.0	137	86
		2	390	111	0.30	rich		0.0	107		0.9	0.9
		3	400	112	0.24	rich	223	0.7	143	0.7		
		4	964	113	0.24	rich	0.0	1.3	11	1.1		
	Cold bypass	1	225	45	0.03	rich	0.2			0.4	0.1	0.1
		2	390	45	0.05	rich	0.6	0.5	291			
		3	400	46	0.03	rich	0.5	0.0	50			
		4	964	46	0.03	rich	1.3	1.8				
	Stripper sump	1	225	151	0	lean				0.3	318	
		2	390	140	0	lean		1.0				186
		3	400	150	0	lean			0.0	1.1		
		4	964	150	0	lean	0.0	0.3				

[5] The hot rich stream was flashing, and part of the CO_2 was in the gas phase; therefore, the liquid phase had a CO_2 loading in the "lean" region.

2.3.1 Temperature Effect on Stainless Steel Corrosion

Figure 2-3 shows the relationship between stainless steel corrosion and temperature. Three levels of fluid velocity at the measurement locations are also shown in the plot. The temperature and velocity were measured during the plant operation and were averaged over the batch period. At low temperature locations (40 °C), corrosion of 316L was minimal, but 316L became vulnerable as the temperature increased. The corrosion rate followed the Arrhenius dependence, and the activation energy of 316L corrosion in 5 m PZ was calculated as 80 kJ/mol. The high corrosion of 316L suggests that 316L is not an ideal construction material for a PZ unit. Vulnerability of 316L has not been rigorously reported in literature because other amines typically operate at 120 °C, where 316L also demonstrated acceptable performance in PZ.

304 and 2205 both showed excellent corrosion resistance even at high temperature locations. The corrosion rates were seldom above 10 μm/yr. Such difference between corrosion performance of 304 and 316L has been rarely seen or expected because these alloys have similar compositions (Table 2-8), and they are usually interchangeable in real plant constructions. Only a few data points are found in literature that show similar difference between 304 and 316L SS at PCCC conditions. A pilot-scale study showed similar findings in a system operating with 30 wt % MEA. 316L corrosion was measured to be up to 800 μm/yr in the hot lean stream exiting the stripper sump, which operated at 120 °C, while 304 had a corrosion rate lower that 25 μm/yr at comparable conditions (Khakharia et al., 2015). The better performance of 304 and 2205 duplex SS might be related to the lower Ni content in those alloys compared to in 316L SS despite the small

difference. High corrosion of Ni-based alloys which is presented in the next section in this chapter may be the empirical proof of the vulnerability caused by Ni.

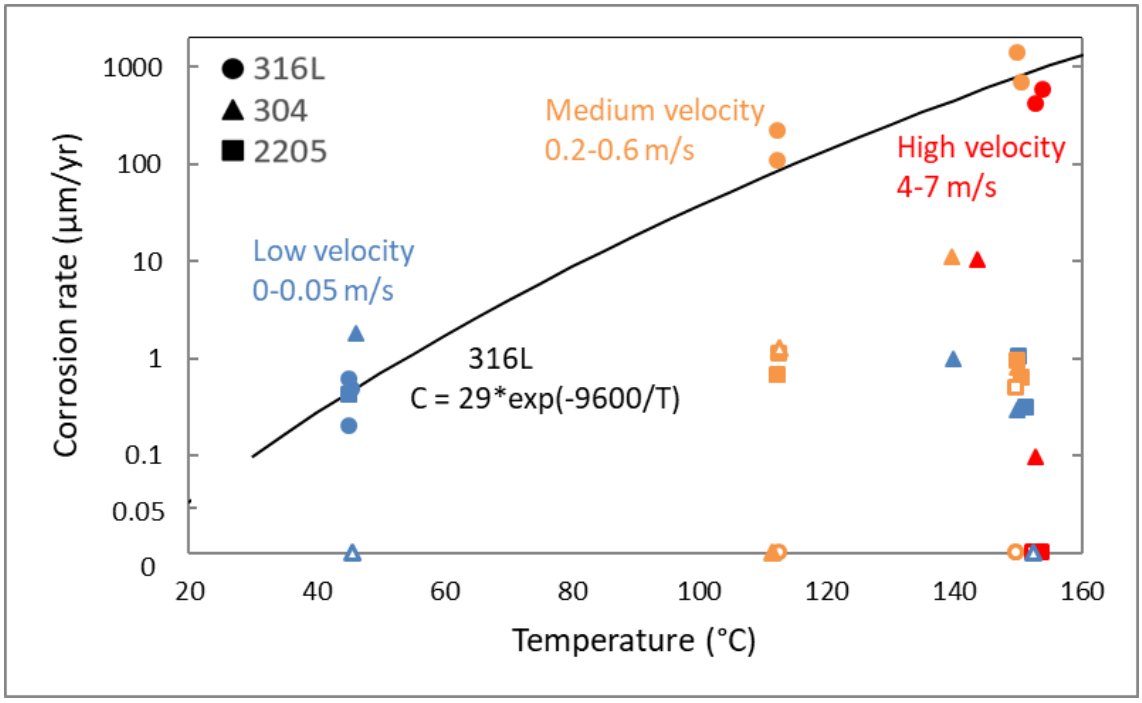

Figure 2-3: Stainless steel (●: 316L, ▲: 304 and ■: 2205 duplex) corrosion rates during the 2019 campaign. Blue points are low fluid velocity (0–0.05 m/s) locations, orange points are medium velocity (0.2–0.6 m/s) locations, and red points are high velocity (4–7 m/s) locations. Corrosion rate is shown on a complex y-axis (0–0.1 µm/yr: linear-scale; >0.1 µm/yr: log-scale). Open points show the rates measured when the carbon adsorption bed was operating. The solid curve shows the Arrhenius dependence of 316L corrosion rates excluding the data with carbon bed. (Liu et al., 2020)

Table 2-8: Compositions of tested stainless steels (Liu et al., 2020)

	Compositions (wt %)								
Alloy	C	Mn	Si	Cr	Ni	P	S	Mo	Fe
316L	0.03	2.00	1.00	16.0–18.0	10.0–14.0	0.045	0.03	2.0–3.0	Bal.
304	0.08	2.00	1.00	18.0–20.0	8.0–10.5	0.045	0.03	0	Bal.

2205	0.03	2.00	1.00	22.0-23.0	4.5–6.5	0.03	0.02	3.0-3.5	Bal.
Inconel 625	0.10 max	0.50 max	0.50 max	20.0–23.0	58.0	0.015	0.015	8.0-10.0	5.0 max
Hastelloy C276	0.01 max	1.0 max	0.08 max	15.0–17.0	57.0	0.04 max	0.03 max	15.0–17.0	4.0–7.0

2.3.2 Effect of PZ Degradation on Stainless Steel Corrosion

Figure 2-4 compares 316L corrosion measured in the 2018 and 2019 campaigns. At cold locations, including the absorber locations and the cold rich bypass in the Advanced Stripper, 316L in both campaigns demonstrated low corrosion (~1 μm/yr). As temperature increased to 116 °C, the corrosion behavior of 316L began to diverge. In 2018, there were some periods of time when corrosion was much lower than that measured in 2019 at comparable temperatures, and sometimes it was as high. The difference in 316L corrosion in the two campaigns might be due to the accumulation of PZ degradation products. Fresh PZ solution was used at the beginning of the 2018 campaign, and after 2100 hours of operation, the solvent was drained from the system and stored until loaded into the system again when the 2019 campaign started. Figure 2-4 shows the analysis of PZ degradation during both campaigns, including the concentrations of two major degradation products: total formate and ethylenediamine (EDA). Accumulation of total formate in the solvent has been reported to be a surrogate of PZ degradation, and EDA has been shown to be highly corrosive and can affect the formation of protective siderite films on carbon steel (Tanthapanichakoon et al. 2006; Liu et al., 2019). Although the level of total formate fluctuated during the latter half of the 2019 campaign, it followed a general increasing trend throughout the two campaigns, indicating continuous PZ degradation during operation. Therefore, the solvent used in the 2019 campaign had higher levels of degradation products, some of which might be corrosive to 316L.

The corrosion measurement showed that 316L corrosion was very low (<1 μm/yr) at all locations, even in the hot rich and hot lean pipes where the corrosion was up to 1400 μm/yr without the carbon bed operation. These results suggest that PZ degradation has an effect on corrosion of 316L, and removal of the degradation products can result in significant decrease in solvent corrosivity. A similar effect of MEA degradation on 316L corrosion has been reported in literature (Fytianos et al, 2014; Fytianos et al., 2016). The removal of degradation products by carbon bed operation was not clear by looking at the EDA or total formate concentrations, suggesting species other than these two have been removed but not yet identified. Though the exact PZ degradation products causing the increase in solvent corrosivity are still unknown, the carbon bed adsorption can be an effective method for mitigating 316L corrosion.

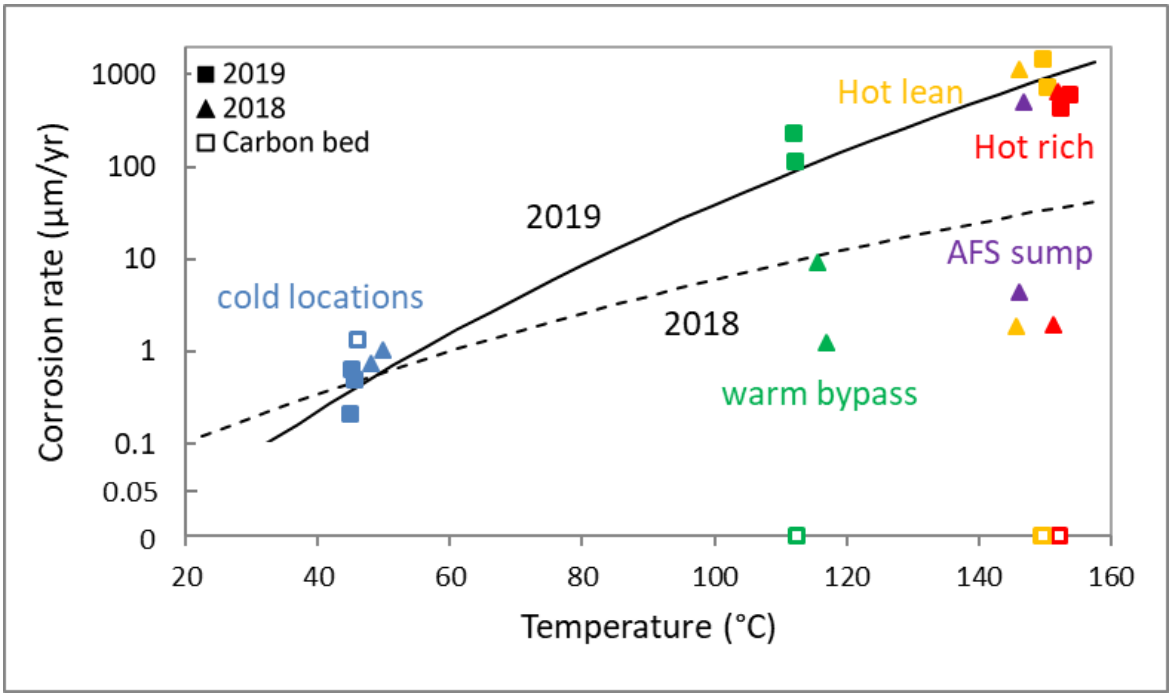

Figure 2-4: 316L corrosion during the 2018(▲) and 2019 (■) campaigns. Blue points are measurements in the cold locations, green points are in the warm bypass, yellow points are in the hot lean stream, red points are in the hot rich stream, and purple points are in the stripper sump. Corrosion rate is shown on a complex y-axis (0–0.1 µm/yr: linear-scale; >0.1 µm/yr: log-scale). Open points show the rates measured when the carbon adsorption bed was operating. The solid curve shows the Arrhenius dependence of 316L corrosion rates in 2019 excluding the data with the carbon bed, and the dashed curve shows the temperature dependence of 316L corrosion in 2018. (Liu et al., 2020)

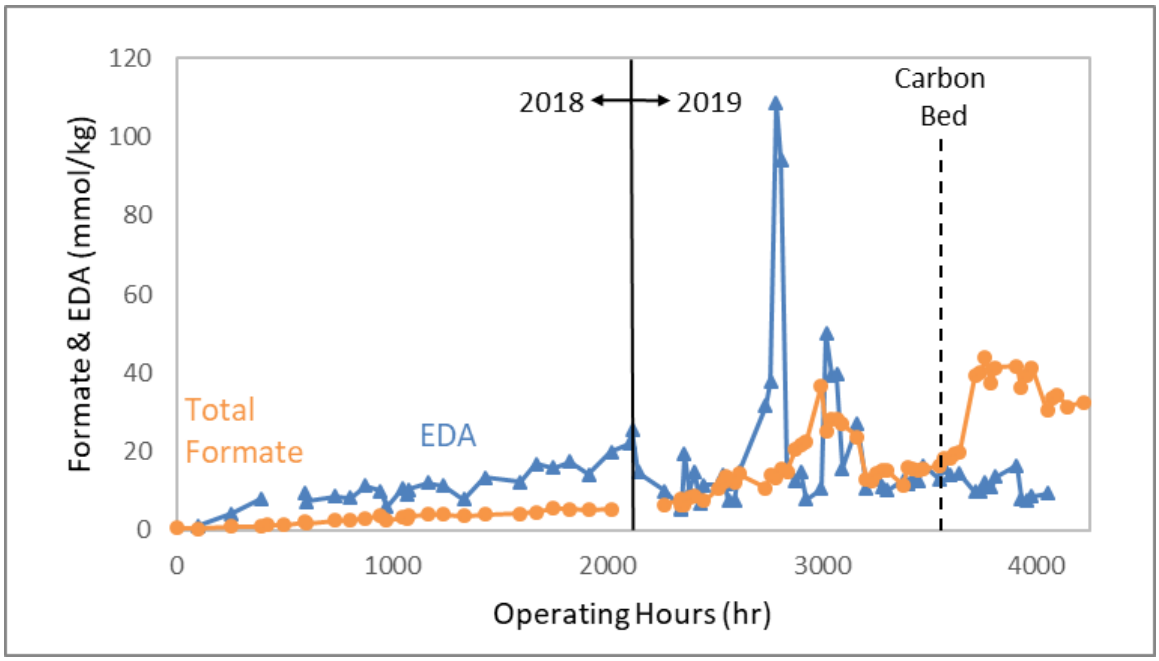

Figure 2-5: PZ degradation analyses during the 2018 and 2019 campaigns. The blue points show the level of ethylenediamine (EDA), and the orange points show the level of total formate in the solvent. (Liu et al., 2020)

2.3.3 Effect of Temperature and Flow Velocity on Carbon Steel Corrosion

Figure 2-6 shows the corrosion of C1010 carbon steel measured in two NCCC campaigns as a function of temperature. The effect of temperature on C1010 corrosion was apparently weaker than its effect on 316L. CS corrosion was generally acceptable (<300 μm/yr) at 50 °C. Corrosion rates measured in the warm bypass around 115 °C were similar to those in the cold pipes at 50 °C. As temperature further increased to around 150 °C, the corrosion rate began to vary widely, indicating temperature was not the most significant factor. The low corrosion rate at 50 °C can be explained by the naturally low reaction kinetics at low temperatures. At 115-155 °C, siderite ($FeCO_3$) films were observed, and such films have demonstrated their ability to protect carbon steel from corrosion (Zheng et

al., 2014a; Zheng et al., 2014b). Fischer (2019) proposed that the temperature effect on the formation of siderite films is driven by the following factors:

1. lower $FeCO_3$ solubility at higher temperatures, increasing the driving force for siderite precipitation (Sun et al., 2009; Sharma et al., 2018)
2. faster kinetics of siderite precipitation at higher temperatures.
3. faster oxidation of Fe at higher temperatures, causing high local supersaturation of $FeCO_3$ near steel surface

Although the precipitation of siderite is favored at high temperatures, it does not always result in low carbon steel corrosion. Other factors, such as flow velocity, can have a significant effect on the properties of siderite protective layers and subsequently, the rate of CS corrosion.

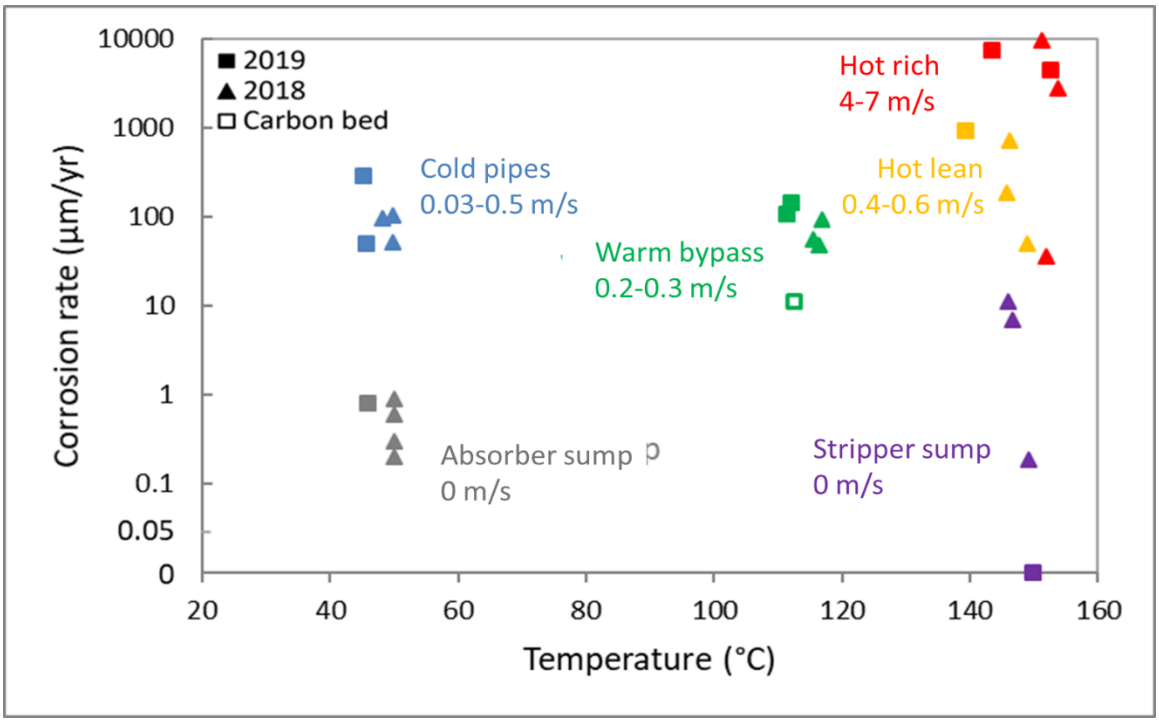

Figure 2-6: C1010 corrosion during the 2018(▲) and 2019 (■) campaigns. Blue points are measurements in the cold pipes (cold bypass and cold lean pipe), grey points are in the absorber sump, green points are in the warm bypass, yellow points are in the hot lean stream, red points are in the hot rich stream, and purple points are in the stripper sump. Corrosion rate is shown on a complex y-axis (0-0.1 µm/yr: linear-scale; >0.1 µm/yr: log-scale). Open points show the rates measured when the carbon adsorption bed was operating. (Liu et al., 2020)

One major factor affecting the protection by siderite films is flow velocity. Solvent is almost stagnant in the absorber and stripper sumps, and zero flow is assumed in the sumps. Moderate velocity locations refer to all the pipe locations except for the hot rich pipe. At these locations, the fluid velocity was estimated between 0.03 and 0.6 m/s at the NCCC pilot plant. The highest flow was measured in the hot rich pipe (4–7 m/s) because the solvent was flashing inside the piping. By comparing the corrosion rates measured at similar temperature but different flow velocities, it was clear that higher corrosion of CS

occurred at higher velocity. CS corrosion in the cold pipes (0.03–0.5 m/s) was higher than in the absorber sump (zero flow), possibly due to increased mass transfer of Fe^{2+} and corrosive species between the boundary layer and the bulk liquid. High fluid velocity might worsen carbon steel corrosion at high temperature because the flow prevented the formation of a dense siderite layer. In the stripper sump, where the liquid was hot and stagnant, CS was well protected by a compact and crystalline siderite layer and exhibited very low corrosion (<11 μm/yr). As flow velocity increased to 0.6 m/s in the hot lean solvent line, CS corrosion increased significantly to ~900 μm/yr. The highest CS corrosion (9600 μm/yr) of the entire process was measured in the hot rich solvent line between the steam heater and the stripper sump. Two-phase flow due to solvent flashing caused extra turbulence and made the condition extremely hard for CS.

Despite the very different corrosion performance among the CS at the high temperature (>100 °C) locations, siderite was identified as the primary corrosion product on the CS coupons retrieved from these locations, suggesting siderite layers were not always protective. Figure 2-7(a) shows the SEM micrograph of a coupon from the stripper sump at NCCC in 2019. A crystalline layer with uniform crystal sizes was observed, and the crystals had a cubic shape. The corrosion rate of this coupon was very low (<1 μm/yr), suggesting that this layer was very protective. Figure 2-7(b) shows the surface of the CS coupon taken from the warm rich bypass in the same campaign. The coupon was also covered by a crystalline siderite layer, but the appearance of the crystals was different. These crystals were smaller and had different shapes than those formed in the stripper sump. The smaller crystals might result in some gaps in between crystals, and the layer lost

some of its protectiveness. Nevertheless, CS corrosion rate measured at in the warm rich bypass was acceptable (<143 μm/yr), and the layer was considered protective.

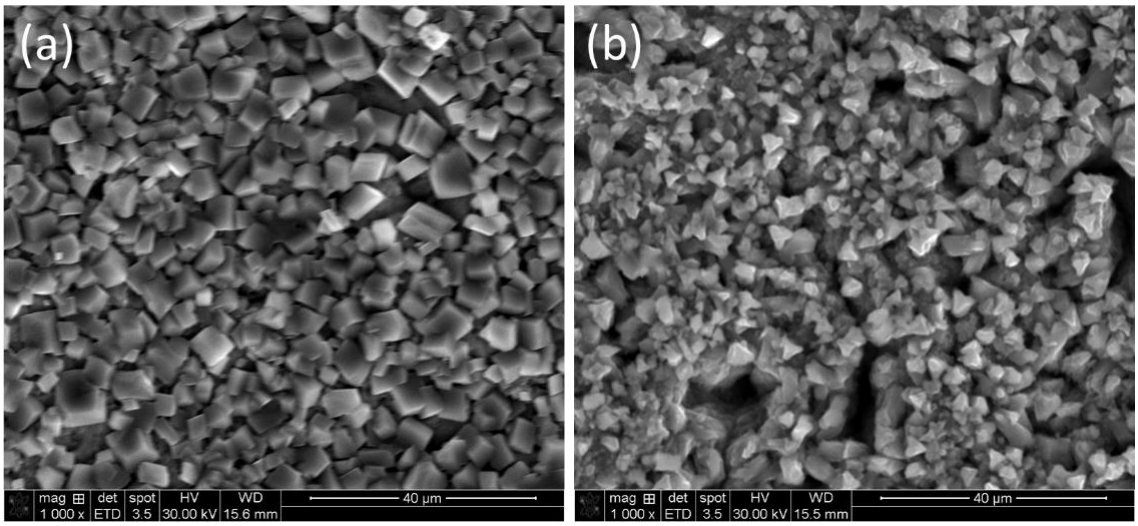

Figure 2-7: SEM micrographs of protective siderite layers on (a) the Batch 3 C1010 coupon in the stripper sump, 0 μm/yr; and (b) the Batch 2 C1010 coupon in the warm bypass, 107 μm/yr in the NCCC2019 campaign. (Liu et al., 2020)

Although all C1010 coupons taken from the warm and hot locations had such siderite layers, some of the layers did not protect the steel. Figure 2-8 shows two C1010 coupons from the hot rich stream that were not protected. The siderite films on these two coupons looked very different from the protective ones shown previously. Instead of a layer of fully grown crystals, the CS seemed to be covered by piles of small crystals. The crystal piles might be porous inside and therefore not protective, and very high CS corrosion (7431 and 2729 μm/yr) was measured by these two coupons.

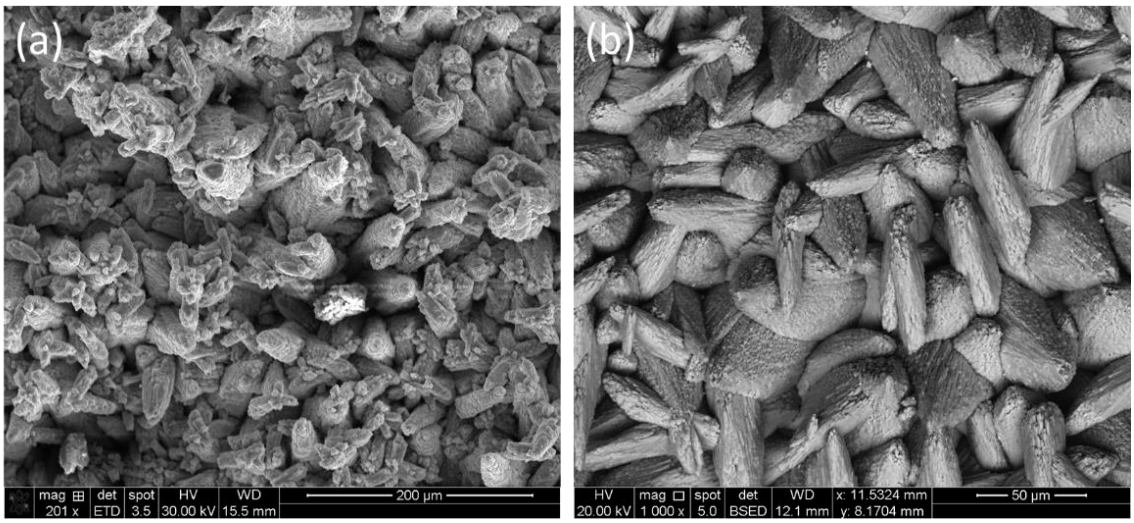

Figure 2-8: SEM micrographs of non-protective siderite layers on (a) the Batch 2 C1010 coupon in the hot rich pipe during the 2019 campaign (200X), 7431 µm/yr; and (b) the Batch 3 C1010 coupon in the hot rich pipe during the 2018 campaign (1000X), 2729 µm/yr. (Liu et al., 2020)

2.3.4 Corrosion of Nickel-based Alloys

Two Ni-based alloys, Hastelloy® C276 (C276) and Inconel® 625 (I625), were evaluated in the Advanced Stripper during the NCCC 2019 campaign and investigated as alternatives to stainless steel. Figure 2-9 shows the corrosion rate of these Ni-based alloys as a function of temperature. Despite the industrially good experience with these alloys, they were surprisingly vulnerable in PZ, especially at high temperature. Similar to 316L, the Ni-based alloys showed corrosion strongly dependent on temperature, and the dependence followed the Arrhenius equation. The activation energy of corrosion of the alloys in PZ was calculated as 93 kJ/mol. There was a pair of points showing minimal corrosion of C276 and I625 at 144 °C. These two coupons were evaluated in the hot rich pipe during the Batch 2 period. During that period, process parametric testing was carried

out, and the process conditions varied frequently. Therefore, it was difficult to interpret the results and establish the cause of better performance. Figure 2-10 shows the photo of a C276 coupon and the surface of the coupon under SEM. The area surrounding the holes was covered by Teflon™ washers during measurement. The liquid could be trapped in the gap between alloy and washers, and thus this area was exposed to a different corrosion environment. The bulk surface of the coupon looked etched and uneven under SEM, and there was a clear boundary between the bulk surface and the area under washers. Figure 2-11 shows the surface profile of the coupon obtained using the Keyence optical profilometer. A clear decrease in height is seen on the 3D surface profile. The red (high) area represents the part of surface covered by Teflon washers, and the blue (low) part represents the surface that was open. The height difference between the two flat plains is 29 μm and represents a corrosion rate of 500 μm/yr, assuming no corrosion at the upper plain. The as-calculated corrosion rate is close to the rate by weight loss measurement (430 μm/yr), and thus it validates the assumption that the area covered by washers experienced little corrosion in hot, rich PZ.

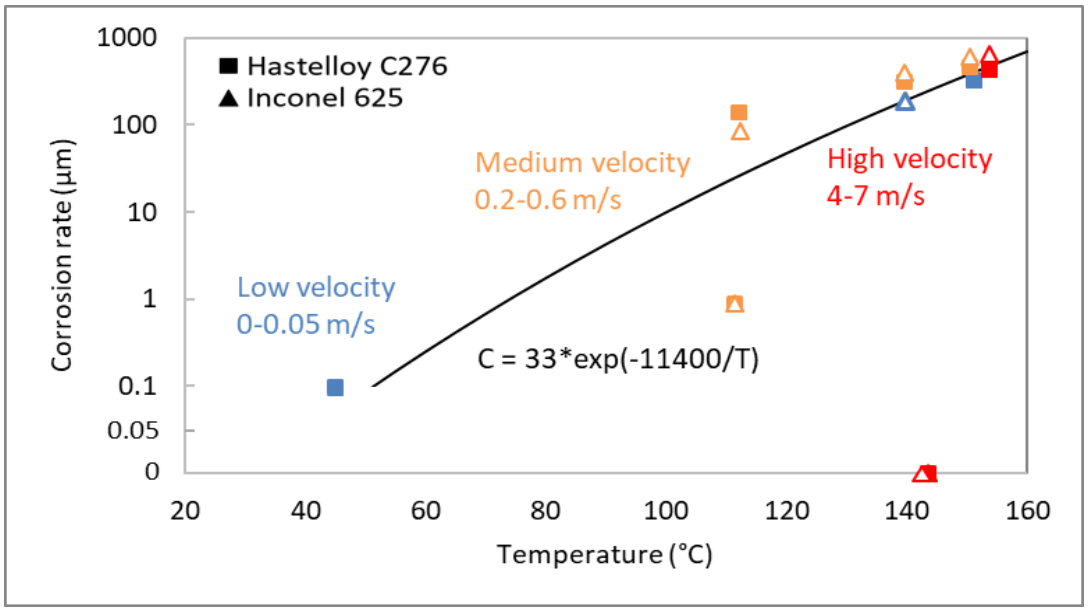

Figure 2-9: Corrosion of Hastelloy® C276 (■) and Inconel® 625 (▲) during the 2019 campaign. Blue points are low fluid velocity (0–0.05 m/s) locations, orange points are medium velocity (0.2–0.6 m/s) locations, and red points are high velocity (4–7 m/s) locations. Corrosion rate is shown on a complex y-axis (0–0.1 µm/yr: linear-scale; >0.1 µm/yr: log-scale). (Liu et al., 2020)

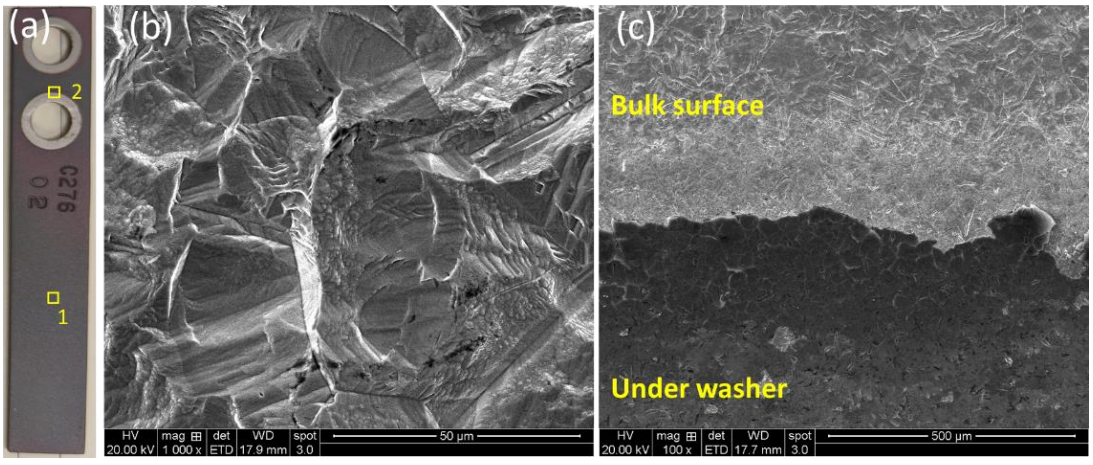

Figure 2-10: (a) Photo of a C276 coupon highlighting two locations imaged with SEM, (b) SEM micrograph of spot 1, and (c) SEM micrograph of spot two. (Liu et al., 2020)

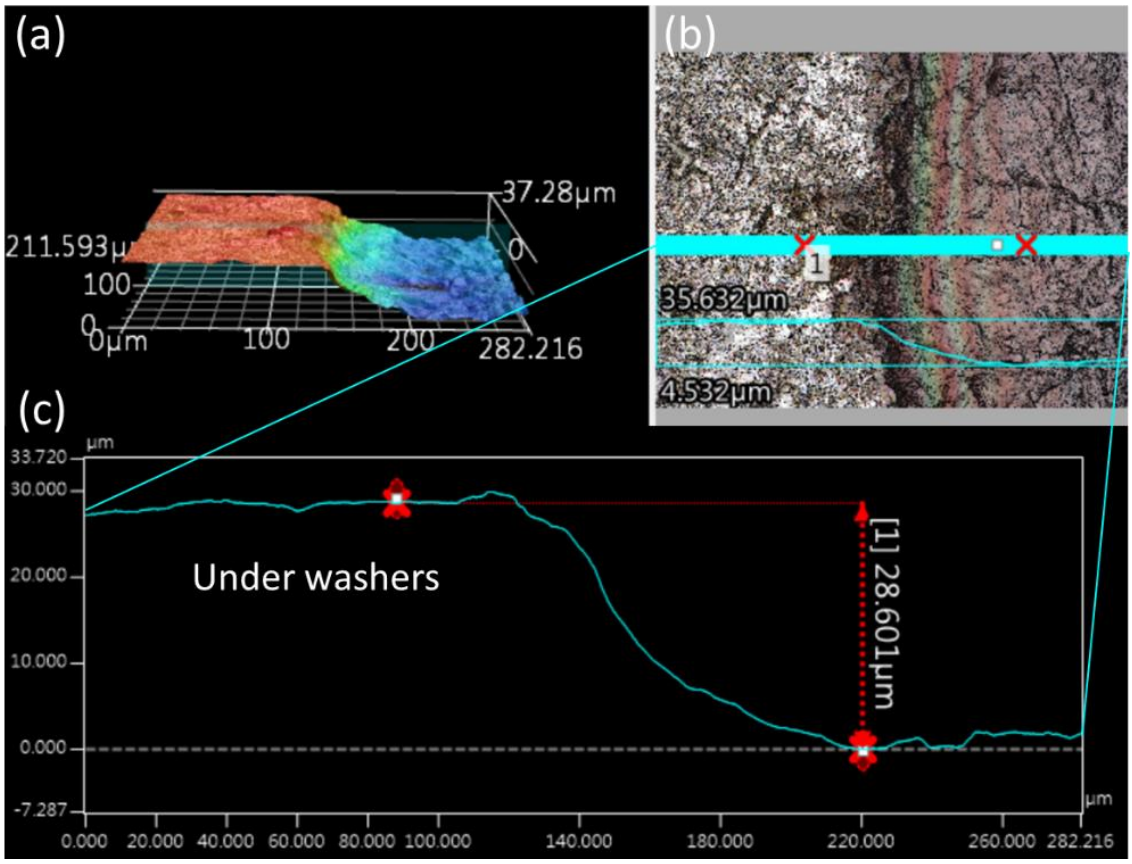

Figure 2-11: Surface profile of the C276 coupon in the hot rich stream during Batch 1 in the 2019 NCCC campaign. (a) 3D profile of the scanned surface, color-coded by height; (b) top-view optical image of the scanned surface, labeling the cross-section for (c) 2D profile analysis. (Liu et al., 2020)

2.3.5 Corrosion During Water Testing

It is common that pilot plants operate with water and perform equipment check during pre-commissioning. It is expected to have more severe corrosion in water than in PZ solvent, especially when an inlet gas containing CO_2 is introduced because the dissolved CO_2 in water creates an acidic environment. Corrosion of carbon steel and stainless steel during water testing was evaluated in the SRP 2021 campaign, and the results are

summarized in Table 2-9. C1010 carbon steel was tested at most of the locations except the hot lean stream, where 304L and 316L stainless steels were tested. The highest C1010 corrosion rate (263–275 μm/yr) was measured in the warm rich bypass and warm total bypass, possibly due to the high temperature (up to 103 °C). In the cold rich stream, intercooler loop, and WW circulation loop, C1010 corroded at a lower rate (108–190 μm/yr) due to the lower temperature (up to 37 °C). C1010 corrosion rate in the absorber sump (53 μm/yr) was one of the lowest among all measurements, and it could be due to the low temperature and liquid flow velocity in the sump. C1010 corrosion was also low (37 μm/yr) in the cold lean stream, possibly because of the lower dissolved O_2 level in this stream. Both stainless steel coupons showed negligible corrosion in the hot lean stream during the operation with water. During the water operation period, the system was shut down each night, and therefore the corrosion rate could be underestimated. Although C1010 corrosion measured during water testing was not extremely high, it is ideal to shorten the water operations to avoid significant metal loss during pre-commissioning.

Table 2-9: Corrosion results during water testing period (Batch 1) at SRP

Location	Material	Corrosion rate (μm/yr)	Temperature (°C)	Liquid velocity (m/s)	Corrosion product
Warm Bypass	C1010	275	82–102	0.2–0.6	Fe_3O_4, FeOOH
Residence Time Mod	C1010	263	80–103	0.3–0.7	FeOOH
Cold Rich	C1010	190	21–35	0.2–0.4	Fe_3O_4
Intercooler	C1010	123	22–33	0.2–0.4	Fe_3O_4, FeOOH
Water Wash	C1010	108	18–31	0.4–0.7	Fe_3O_4, FeOOH
Absorber Sump	C1010	53	22–37	0	Fe_3O_4, FeOOH
Cold Lean	C1010	32	21–32	0.2–0.4	Fe_3O_4, FeOOH
Hot Lean	304L	0	91–151		-
	316L	0	91–151		-

2.3.6 Effect of PZ Oxidation Mitigation on Corrosion

Several operations related to the study of PZ oxidation were performed during the SRP 2021 campaign, including the introduction of NO_2 in flue gas, increased residence time in the warm rich bypass, N_2 sparging in the absorber sump, and removal of degradation products by carbon adsorption. The corresponding effects of these operations on corrosion are presented in this section.

The presence of NO_2 in the flue gas has been shown to significantly increase the rate of PZ oxidation via radical reactions; therefore, removal of NO_2 from flue gas is proposed as a mitigation method for PZ oxidation (Fine, 2015). NO_2 is also believed to increase the oxidation potential of PZ solvent and may affect steel corrosion. Table 2-10

summarizes the coupon results during the PZ baseline and NO_2 periods. Batch 2 and 3 coupons were tested under PZ baseline condition, and the results from the two batches are highly consistent. During the PZ baseline period, warm rich bypass exhibited highest corrosion rate of carbon steel (118 µm/yr) because of the high temperature. A black product layer was deposited on this coupon and identified by XRD as siderite ($FeCO_3$). CS corrosion was generally low at all the low temperature locations, including cold lean, cold rich, and the absorber sump, and no removable corrosion product was observed. When NO_2 was incorporated into the flue gas, CS corrosion in the warm rich bypass decreased to 29 µm/yr during the first 143 hours and later increased to 195 µm/yr. The reason for the decrease in corrosion rate is not clear. It might result from the more oxidizing solvent environment, which oxidized Fe^{2+} in the solution to Fe^{3+}, lowered the overall solubility of the Fe species, and therefore, reduced the driving force for iron dissolution. The subsequent increase in corrosion rate could be due to the accumulation of PZ degradation products, such as mononitrosopiperazine (MNPZ). CS at cold lean experienced higher corrosion (155 µm/yr) during the NO_2 period, which can also be attributed to higher level of PZ degradation. Both 304L and 316L stainless steel exhibited very low corrosion rate (<2 µm/yr) in the hot lean stream during the PZ baseline and NO_2 periods.

Table 2-10: Corrosion results during PZ baseline and NO_2 period at SRP

			Batch 2 & 3 PZ baseline 1/2 121/40 hrs			Batch 4-1 NO_2 1 143 hrs			Batch 4-2 NO_2 2 76 hrs		
Location	Alloy	Flow velocity (m/s)	Corrosion rate (µm/yr)	Median T (°C)	Corrosion product	Corrosion rate (µm/yr)	Median T (°C)	Corrosion product	Corrosion rate (µm/yr)	Median T (°C)	Corrosion product
Warm Bypass	C1010	0.2	115/118	116/114	$FeCO_3$	29	115		195	116	Fe_2O_3
Cold Lean	C1010	0.1	41/38	26/27		123	27		155	25	
Cold Rich	C1010	0.1	19/16	23/16		14	16		1	15	
Absorber Sump	C1010		13/12	25/21		14	18		14	19	
Hot Lean	304L		0.2/0.1	142/140		2	140		1	141	
	316L		0.2/0.1	142/140		1	140		1	141	

PZ oxidation by dissolved O_2 mostly takes place in the warm rich bypass. Increased residence time in the warm rich bypass was proposed to increase PZ degradation rate and reduce the dissolved O_2 in the stripper area. N_2 sparging in the absorber sump is another way to lower the dissolved O_2 content in the solvent. During the period when the plant operated with increased residence time in the warm rich bypass and N_2 sparging in the absorber sump, the PZ solvent became very reducing. Removal of PZ degradation products by an activated carbon bed has been demonstrated to reduce corrosion significantly in the NCCC 2019 campaign, and the effect was tested again during the last week of the SRP 2021 campaign.

Table 2-11 summarizes the corrosion results from Batches 5 and 6 at SRP. Batch 5 covered the period when N_2 was sparged into the absorber sump and the residence time modification was online. The highest CS corrosion rate was observed at the warm rich bypass and the residence time modification. The result is not surprising given the high temperature. Though the two locations are on the same process line, the corrosion products collected from the CS coupons had different compositions. $Fe(III)_2O_3$ was the dominant product at the warm rich bypass location. Going down the line to the residence time modification, a mixture of $Fe(III)_2O_3$ and $Fe(II)CO_3$ was observed. The transition from ferric iron to ferrous iron in the corrosion product speciation could be an indication that the PZ solvent became more reducing as it traveled along the warm bypass. CS coupons at the low temperature locations during this period all showed acceptable performance. 304L SS and 316L SS also performed well despite our hypothesis that solvent at extremely reducing conditions may compromise the passivation of SS and lead to significant corrosion. Batch 6 coupons were intended to evaluate corrosion when the carbon bed was online to remove

PZ degradation products. Even though the carbon bed was not turned on until the last week of this campaign, there had not been much degradation product accumulation in the solvent before the carbon bed was turned on. Therefore, corrosion during the carbon bed period was not significantly different from the previous batches.

The effect of these operations to mitigate PZ oxidation on corrosion was not clear within the short operating period during the SRP 2021 campaign. More hours for each operation may be necessary for more obvious effects to be observed.

Table 2-11: Corrosion results during N_2 sparging/increased residence time in warm bypass and carbon bed periods at SRP

			Batch 5 N_2 sparging + increased residence time 192 hrs			Batch 6 Carbon bed 99 hrs		
Location	Alloy	Flow velocity (ft/s)	Corrosion rate (µm/yr)	Median T (°C)	Corrosion product	Corrosion rate (µm/yr)	Median T (°C)	Corrosion product
Warm Bypass	C1010	0.2	232	113	Fe_2O_3	23	116	
Residence Time Mod	C1010	0.3	282	113	Fe_2O_3, $FeCO_3$	225	110	$FeCO_3$
Cold Lean	C1010	0.1	57	27		111	27	
Cold Rich	C1010	0.1	0.3	18		2	22	
Absorber Sump	C1010		0.3	19		2	19	
Hot Lean	304L		1	140		1	141	
	316L		1	140		1	141	

2.4 CONCLUSIONS

2.4.1 316L SS showed severe corrosion by aqueous PZ at high temperatures, while 304 stainless and 2205 duplex stainless steel remained highly resistant to corrosion at similar conditions.

High corrosion rate of 316L SS was measured in the high temperature region of PZAS. The highest rate was 1429 μm/yr in the hot lean solvent line (~150 °C), and the corrosion rate showed strong dependence on temperature:

$$Corrosion\ rate\ \left(\frac{\mu m}{yr}\right) = 29 \times \mathrm{EXP}\left(\frac{-9600}{T(K)}\right)$$

304 SS and 2205 duplex SS performed very well at all measurement locations. The rate of corrosion never exceeded 10 μm/yr at both NCCC and SRP pilot plants.

2.4.2 PZ degradation may increase corrosion of 316L SS. Removal of PZ degradation products by a carbon adsorption bed significantly reduced 316L corrosion.

316L SS showed higher corrosion at the NCCC pilot plant in 2019 than in 2018. The chronological increase in corrosion rate could be explained as the effect of PZ degradation. The PZ solvent was more degraded in 2019 as it had been through ~2100 hours of operation in 2018. An activated carbon bed was put into service during the last few weeks of the 2019 NCCC campaign to remove PZ degradation products from the solvent. Significant decrease in 316L corrosion from >1000 μm/yr to negligible values was observed when the carbon bed was in operation, suggesting some corrosive degradation products were removed by the carbon bed.

2.4.3 Carbon steel corrosion can be greatly reduced by a protective siderite ($FeCO_3$) film formed at 110–155 °C. The protection diminished at high flow velocity or in two-phase flow.

Siderite was observed as the primary corrosion product on CS coupons in the high temperature (110–155 °C) regions of PZAS. The protectiveness of the films decreased with increasing flow velocity. At low velocity in the stripper sump, a crystalline and compact siderite film was formed and resulted in very low corrosion of CS (<11 μm/yr) even though it was one of the hottest (150 °C) points of PZAS. At moderate flow velocity (0.4–0.6 m/s) and the same high temperature, CS corrosion rate was as high as 910 μm/yr. Even higher corrosion rate (9600 μm/yr) was observed in high velocity, two-phase flow between the steam heater and the stripper sump. The loss of protectiveness could be a result of the formation of porous siderite films under high flow velocity.

2.4.4 Ni-based alloys were vulnerable in PZ at high temperature, and the rate of corrosion increased with increasing temperature.

Inconel® 625 and Hastelloy® C276 were evaluated in the Advanced Stripper in the 2019 NCCC campaign, and both showed poor corrosion resistance in PZ at high temperature. Therefore, the Ni-based alloys may not be good candidate materials for PZAS™. Their corrosion rates showed dependence on temperature:

$$Corrosion\ rate\ (\frac{\mu m}{yr}) = 33 \times EXP\left(-\frac{11400}{T(K)}\right)$$

2.4.5 Corrosion of CS by water during water testing can be significant at high temperatures, and SS corrosion by hot water is negligible.

CS corrosion during water testing was evaluated in the SRP 2021 campaign, and the highest rate was 275 μm/yr in the warm bypass. Although the CS corrosion rate measured during the water testing period all seemed acceptable (<300 μm/yr), long

operating hours with water should be avoided if any part of the system is built with CS. 316L and 304L SS performed very well in hot water up to 151 °C

2.4.6 Several mitigation methods to reduce PZ oxidation were tested in the SRP pilot plant. Most of them had minor effects on corrosion compared to temperature and flow velocity.

NO_2 injection, N_2 sparging in the absorber sump, increased warm bypass residence time, and removal of PZ degradation products by a carbon bed were evaluated in the SRP 2021 campaign. Most of these operations seemed to slightly alter the oxidation state of the PZ solvent but did not show significant effect on CS or SS corrosion. Longer period for each operation is recommended for the future pilot testing.

Chapter 3: Corrosion in PZAS Absorber and Water Wash

3.1 INTRODUCTION

Stainless steel construction for a post-combustion CO_2 capture (PCCC) unit is chosen largely based on experience with concentrated aqueous monoethanolamine (MEA). Piperazine (PZ), as a secondary amine, has intrinsically lower corrosivity than primary amines like MEA (Kohl et al., 1997; Gunasekaran et al., 2013; Gunasekaran et al., 2017). Corrosion results from pilot-scale testing described in the previous chapter have demonstrated that carbon steel (CS) may be a good material candidate for the absorber with PZAS. Even without the siderite protective layer that was only observed in the Advanced Stripper at high temperature (120–155 °C), CS generally showed acceptable corrosion performance (<300 μm/yr) in the absorber area at pilot plants. However, to ensure smooth operation of pilot plants, the flexibility of adjusting parameters independently was limited. Corrosion data were collected only at a handful of conditions, and correlations between corrosion and each process variable, such as temperature, CO_2 loading, flow velocity, and PZ degradation could not be established based on only the pilot-scale data.

In addition to the lack of correlation between corrosion and process variables at absorber conditions, there are few corrosion data for the water wash of an amine-scrubbing system available in the literature. The presence of PZ can result in increased pH, which is expected to lower the solution corrosivity. However, it can also shift the equilibrium between H_2CO_3 and HCO_3^-/CO_3^{2-}. At a pH above 6.3, HCO_3^-, which is postulated to be a corrosive agent in CO_2-H_2O-amine systems (Veawab et al., 2002), becomes the dominant species in an aqueous CO_2 system. In addition, HCO_3^- is an important reagent of the formation of siderite ($FeCO_3$) films on carbon steel in CO_2-loaded solution. Whether a

protective layer of siderite can form on carbon steel at the water wash conditions would greatly affect the material selection for the column and piping in this area.

To better understand the corrosion performance and provide material recommendations for the absorber and water wash in PZAS, corrosion experiments in multiple bench-scale apparatuses were performed, and the results are presented in this chapter.

3.2 BACKGROUND

This section provides background relevant to corrosion in the PZAS absorber and water wash. Most corrosion data in the review are from bench-scale experiments performed in electrochemical cells. Due to the pressure limit of the glassware used in these experiments, corrosion measurements were taken below 80 °C near atmospheric pressure, which is similar to the conditions in the absorber area and the water wash of PZAS™.

3.2.1 Corrosion by Aqueous Amines for CO_2 Capture

Aqueous amines are not intrinsically corrosive because of their high pH and low conductivity, but they may become corrosive when they absorb acid gases (DuPart et al.; 1993a). Although corrosion in an aqueous system has been extensively studied, the interaction of amine-H_2O-CO_2-Fe adds significant complexity to the corrosion behavior in an amine-based CO_2 capture system. So far, no consensus has been reached concerning the mechanisms of corrosion by amine solutions. However, some systematic trends that govern the corrosivity of amine solutions loaded with CO_2 have been identified.

It is well agreed that when solution is loaded with CO_2, primary amines are the most corrosive, followed by secondary amines, and tertiary amines have the lowest corrosivity (Veawab et al., 1999; Bonis et al., 2004; Gunasekaran et al., 2013). Figure 3-1

shows that under CO_2-saturated conditions and 80 ˚C, the rate of carbon steel corrosion in several amines are in the following order: monoethanolamine (MEA) > 2-Amino-2-methyl-1-propanol (AMP) > diethanolamine (DEA) > PZ > methyl diethanolamine (MDEA) (Gunasekaran et al., 2013). MEA, as a primary and the benchmark amine for CO_2 capture, has the highest corrosivity. The sterically hindered primary amine, AMP, is less corrosive. The overall higher corrosivity of primary and secondary amines than tertiary has been proposed to be related to the formation of carbamate ions. Primary and secondary amines react and form amine-carbamates and protonated amines (Equation 3-1). Tertiary amines do not form carbamate because there is no hydrogen atom attached to the nitrogen. Therefore, the reaction of tertiary amines and CO_2 is associated with bicarbonate formation (Equation 3-2). Carbamate may play the role of a chelating agent to form iron complex-compounds, which would promote metal dissolution (Wong et al., 1985; Tomoe, 1996). Chelating can also increase the apparent solubility of $FeCO_3$, resulting in the dissolution of protective films.

$$2R_2NH + CO_2 \leftrightarrow R_2NCOO^- + {R_2NH_2}^+ \quad (3\text{-}1)$$

$$R_3N + CO_2 + H_2O \leftrightarrow HCO_3^- + R_3NH^+ \quad (3\text{-}2)$$

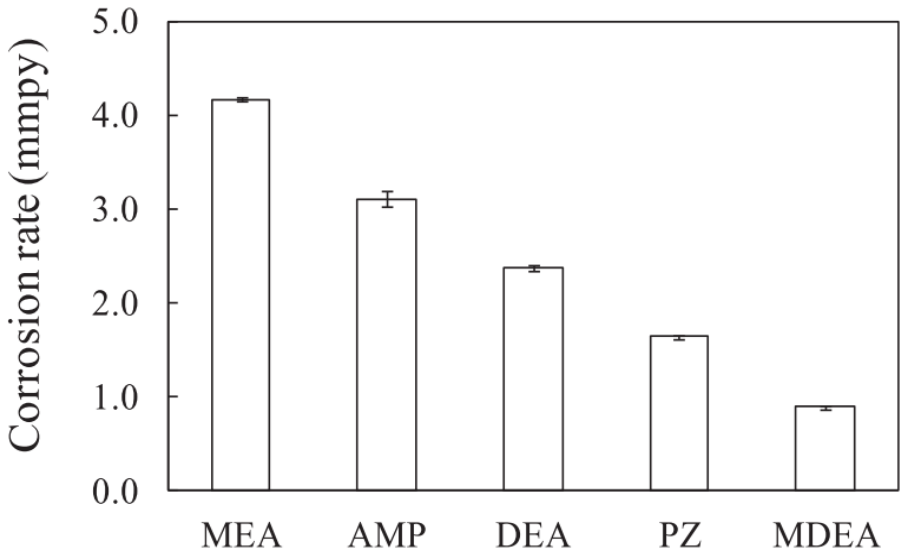

Figure 3-1: Corrosivity of amine solutions at 80 ˚C, sat. CO_2 (5 kmol/m^3 MEA, DEA, MDEA, and PZ; 4.0 kmol/m AMP) (Gunasekaran et al., 2013).

It has been proposed that amines with greater bicarbonate (HCO_3^-) concentration, or with a higher tendency to form HCO_3^-. For example, hindered amines like AMP, are more corrosive (Veawab et al., 1999). Higher concentration of HCO_3^- promotes its reduction to CO_3^{2-}, which is a critical reduction reaction coupled with oxidation of a metal surface (Equation 3-3).

$$Fe + 2HCO_3^- \rightarrow Fe^{2+} + 2CO_3^{2-} + H_2 \quad (3\text{-}3)$$

3.2.2 Bench-Scale Corrosion by MEA at PCCC Conditions

MEA has long history of being used to capture H_2S and CO_2 from natural gas and is broadly considered the benchmark solvent for PCCC. MEA is one of the most corrosive amines, and it has bad reputation for corrosion problems in acid gas treating. Several bench-scale studies on corrosion in MEA solutions have been done (Veawab et al., 1999;

Veawab et al., 2002; Kittel et al., 2009; Soosaiprakasam et al., 2008). Most of these studies were performed in electrochemical cells at moderate temperature (max. 80 ˚C) near ambient pressure. The corrosion rates were determined by measuring corrosion current density and converting the electrical current to metal loss rate using Faraday's law. This section summarizes the impact of several parameters on MEA corrosion. Though PZ is expected to have less corrosion problems than MEA, experience with MEA can still inform the study of PZ corrosion.

The temperature effect on corrosion in MEA was mainly evaluated between ambient temperature and 80 ˚C in laboratory conditions. Because corrosion reactions are thermally activated electrochemical reactions, the rates of both cathodic and anodic reactions increased as temperature increased (Veawab et al., 1999; Kittel et al., 2009; Soosaiprakasam et al., 2008). At a given CO_2 loading, the measured corrosion rate follows a linear evolution with the reciprocal of temperature, confirming thermal activation (Kittel et al., 2009).

CO_2 loading is another significant parameter for corrosion in MEA solution. Kittel et al. (2009) showed that in 30 wt % MEA at 80 ˚C, the corrosion rate of carbon steel increased from 50 to >500 μm/yr as CO_2 loading increased from 0 to 0.5, and both cathodic and anodic reaction rates increased.

Combining the loading and temperature effects (Figure 3-2), carbon steel corrosion in MEA is expected to be the most severe at the hot (120°C), rich part of the process. Even in the more moderate conditions in the absorber (50 ˚C), carbon steel may not show satisfactory performance in 30 wt% MEA.

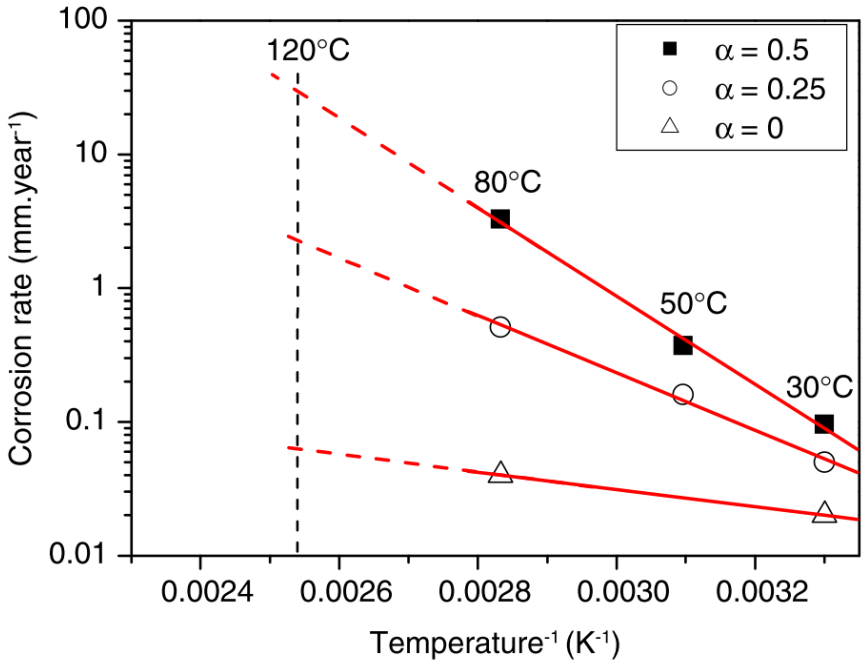

Figure 3-2: Temperature and loading effects on carbon steel corrosion in MEA (Kittel et al., 2009).

The impact of amine concentration was also evaluated in these studies. At constant CO_2 loading, a weak increase of carbon steel corrosion rate is observed when the MEA concentration is raised from 6 to 30% (Veawab et al., 1999). Between 30% and 55% MEA, the electrochemical measurements show very similar corrosion rates (Veawab et al., 1999; Soosaiprakasam et al., 2008). Despite the low dependence on MEA concentration in the high concentration region, a more concentrated solution is usually more prone to amine degradation (Wagner et al., 2006; Lawal et al, 2006) which can generate corrosive degradation products (Kittel et al., 2014).

The impurities in amine solutions, including heat stable salts generated from amine degradation, dissolved O_2, SO_2, and NO_2 were all found detrimental to the corrosion

performance of steels. Studies of the effect of several MEA degradation products on corrosion show that formic acid, oxalic acid, and compounds that can degrade into HSS related to these two (formate and oxalate) have more observable effect (Fytianos et al., 2014; Fytianos et al., 2016). For O_2, SO_2, and NO_2, the main impact may be on amine degradation, which can produce corrosive degradation products, rather than on corrosion directly. Studies of the effect of several parameters on corrosion in 30 wt % MEA show that while the carbon steel corrosion rates increased with increasing concentrations of O_2 and SO_2 in the simulated inlet gas, the effect remained second-order to the effects of temperature and MEA concentration evaluated in the same study (Kladkaew et al., 2009a; Kladkaew et al., 2009b).

3.2.3 Wet CO_2 Corrosion in the Water Wash

Corrosion by wet CO_2 can occur in the water wash where there is little or no amine in the solution. The mechanisms of corrosion in an aqueous system have been extensively studied. At the steel surface where corrosion occurs, metal (iron) undergoes the oxidation reaction in Equation 3-4, and the metal ions go into solution. In an acidic solution, the reduction reaction in Equation 3-5 occurs. At low pH, the rate of corrosion is higher due to the higher concentration of H^+, which results in greater potential driving force for the electrochemical reaction. Another mechanism by which low pH accelerated corrosion is the dissolution of the protective corrosion scale in an acidic environment. In the presence of dissolved oxygen, ferrous hydroxide or ferrous oxide can deposit on steel surfaces and compose a barrier through which the species associated with the cathodic reaction must diffuse. Such a barrier is dissolved in strong acids at pH below 4, and with weaker acids (carbonic, acetic) the dissolution occurs at pH 5 to 6.

$$Fe \leftrightarrow Fe^{2+} + 2e^{-} \quad (3\text{-}4)$$

$$2H^{+} + 2e^{-} \leftrightarrow H_2 \quad (3\text{-}5)$$

Dissolved CO_2 forms carbonic acid and partially dissociates into H^+ and CO_3^{2-}. As a weak acid, dissolved CO_2 can cause steel corrosion at higher rates than stronger acids do. This is explained by the higher total acidity of a partially dissociated acid compared with a completely dissociated acid at a given pH (Uhlig et al., 1985). The fundamentals of corrosion by dissolved CO_2 were discussed by Schmitt (1985a). In the absence of the protective corrosion scales, the uniform corrosion rate on bare iron surfaces is controlled by the kinetics of the cathodic reaction, which is hydrogen evolution in a system with only water and CO_2. Such a scenario is usually considered the "worst case." A correlation of corrosion rates for the worst case of plain steels, and several parameters including CO_2 partial pressure and temperature, were established by de Waard (1975) as in Equation 3-6.

$$\log CR = 0.67 \times logP_{CO2} + \frac{Q}{RT} \quad (3\text{-}6)$$

where:

CR = corrosion rate (mm/yr)

P_{CO2} = CO_2 partial pressure (bar)

Q = activation energy = 10.7 kcal/mol

R = gas constant

T = temperature (K)

Equation 3-6 remains valid at low CO_2 partial pressures (<2 bar) and temperatures up to 60 ˚C under laminar flow conditions. At higher CO_2 partial pressures and temperatures, the observed corrosion rates are usually lower than the rates predicted by the equation due to

the rapid formation of a protective layer of siderite ($FeCO_3$), which is a major corrosion product in a CO_2 environment.

Although not very much, the water wash solution typically contains some level of amine, which can cause a significantly different corrosion environment from an aqueous CO_2 system. Currently, there is limited corrosion data in dilute amine solutions in the water wash conditions for PCCC.

3.3 EXPERIMENTAL METHODS

3.3.1 Low-Gas Flow (LGF) Reactor

Figure 3-3 shows the setup of the low-gas flow reactors. The design and dimensions of each part have been detailed by Freeman (2011). The inlet gas from a pre-mixed gas cylinder came in at a rate of 100 cc/min to a pre-saturator (wrapped with fiberglass pipe insulation) and was saturated with water to maintain the water balance in the reactors. Then the gas was bubbled into the solvent in the jacketed reactors. Two inlet gas mixtures were used in the experiments presented in this report: 1.5% CO_2 in air and 18% CO_2 in N_2. The current setup has two jacketed glass reactors with Teflon™ lids. The jackets of the reactors were connected to an oil bath to control the temperature in the reactors. The solvent volume in each reactor was around 600 mL and was agitated magnetically or mechanically to simulate liquid flow in real pipes.

Figure 3-3: Low-gas flow reactor setup

Each lid has three coupon holders also made of Teflon™ (Figure 3-4). The corrosion coupons are purchased from Metal Samples Company and used as received. The alloys tested include C1010 carbon steel, 430 stainless steel, 304L stainless steel, and 316L stainless steel. The coupons were weighed before being immersed in PZ solution. The experiments typically lasted 3 to 5 days. Once removed from the PZ, coupons were rinsed with deionized water, dried, photographed, wrapped in the original packaging, and placed in a glass desiccator until analysis could be performed. Coupons were mounted for imaging by a scanning electron microscope (SEM). Afterward, any corrosion product was scraped off and analyzed by powder x-ray diffraction (XRD). Any residual corrosion product was removed using concentrated HCl inhibited by N, N'-dibutylthiourea, and a final weight loss was calculated.

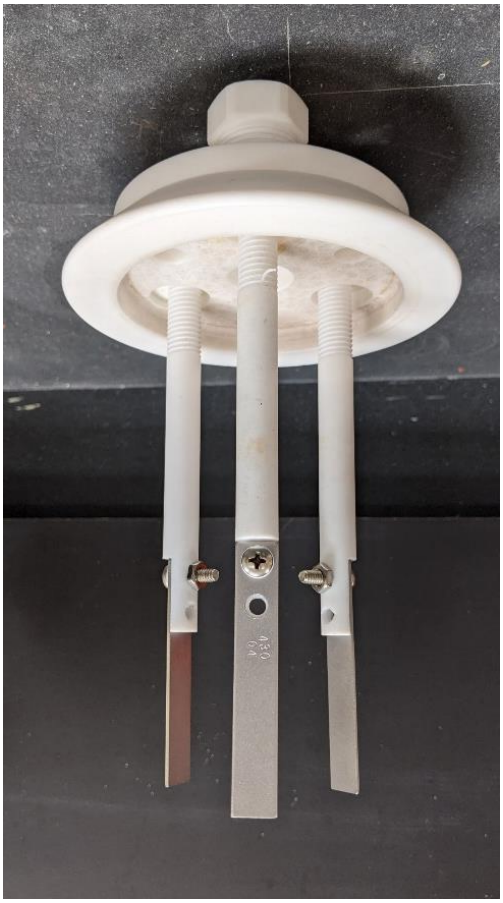

Figure 3-4: Teflon lid with three coupon holders

3.3.2 Pump Around Corrosion Loop (PACL)

A schematic of the new corrosion loop is given in Figure 3-5. The PACL mainly consists of a variable speed gear pump (CHEMSTEEL™ S923 M) and a pipe loop. The size of the pipe loop around the pump is 1.5” to match the pump connections. The rest of the pipe loop is reduced to 1/2” in order to allow higher flow velocity at a given flow rate and reduce total solvent inventory. One 3/4” and three 1” threaded NPT ports are installed on the 1.5” pipe section downstream of the pump to allow the insertion of corrosion and oxidation-reduction potential (ORP) probes. Immediately downstream of the corrosion probe location, there is a 1/8” Swagelok® port connected to a syringe pump (New Era Pump

Systems Inc. NE-8000). This port allows for injection of liquids, such as oxidizer/reducer liquid, into PACL during experiments. Cylindrical coupons (Metal Samples Co. ES204) are installed at the nine 4-way tees in the 1/2" pipe section to evaluate corrosion at pipe bends. A needle valve is installed on the top horizontal pipe section to control liquid flow rate and pressure drop. The section of 1.5" pipe downstream of the pump discharge is wrapped with a heating cable, which is controlled in the DeltaV™ Automation System by Emerson Electric Co. An armored level gauge (Jerguson Gage & Valve Co. 115R300L) and a vibrating fork level switch (Rosemount™ 2120D0DG1E7SA0000) on the upper left of the loop monitor the solvent inventory. The vertical section of pipe below the level gauge can be replaced by three sets of tube coupon assemblies for better study of corrosion on straight pipe walls. The tube coupons are made from 9/16" tubing to match the inner dimeter of 1/2" pipes, cut to desired length, cleaned with DI water and acetone, weighed, and mounted on flanges on both sides using Swagelok® NPT adapters. The materials of flanges and adapters are the same as the tube coupon material. The adjacent flanges from different assemblies are isolated by gaskets and bolt sleeves to avoid contact between different alloys. A N_2 line with a manual gas flow regulator, a 1-way check valve, and a back-pressure regulator are used to control system pressure. The process control interface in DeltaV™ is given in Figure 3-8. More details of the PACL and the standard operating procedures are given in Appendix A.

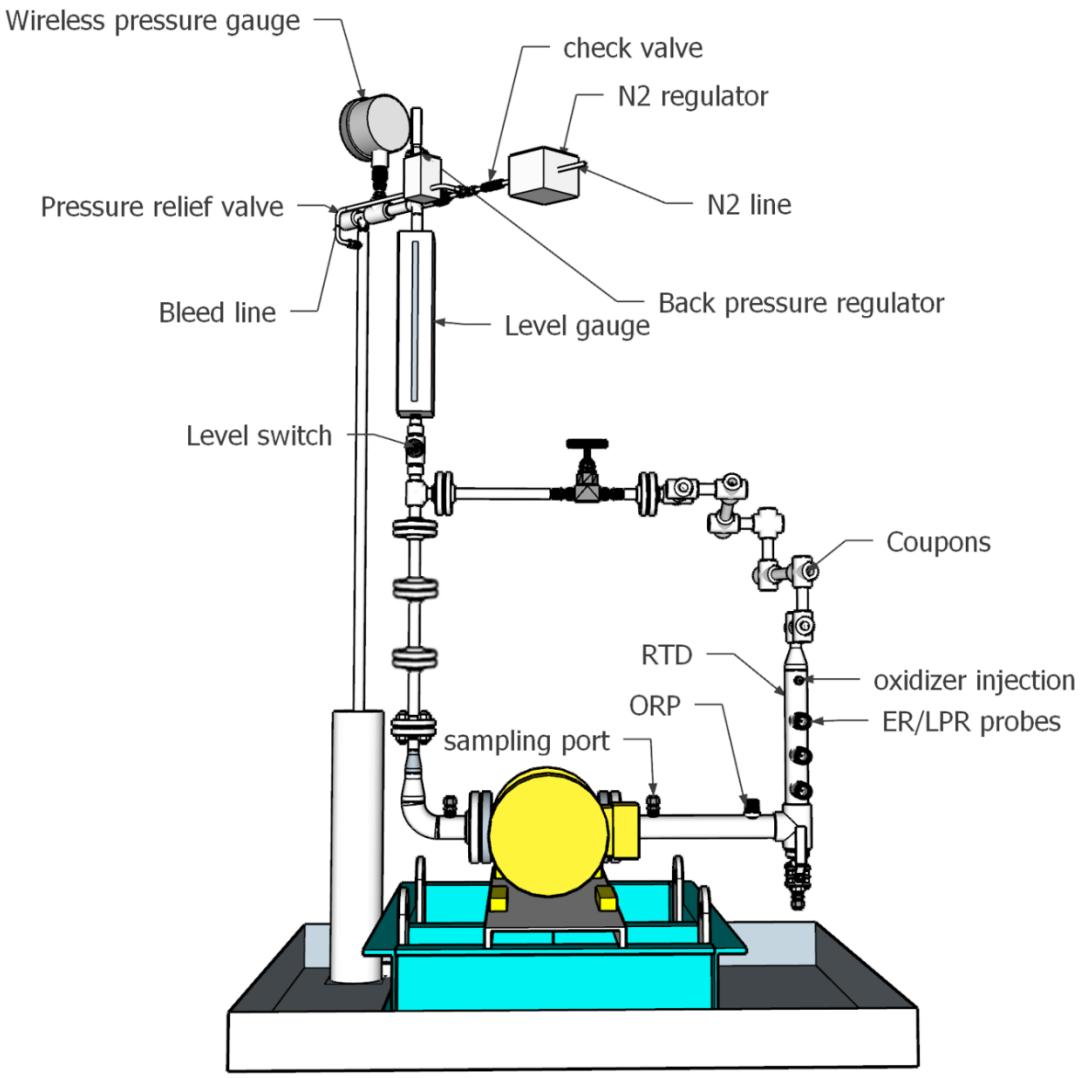

Figure 3-5: Pump around corrosion loop (PACL)

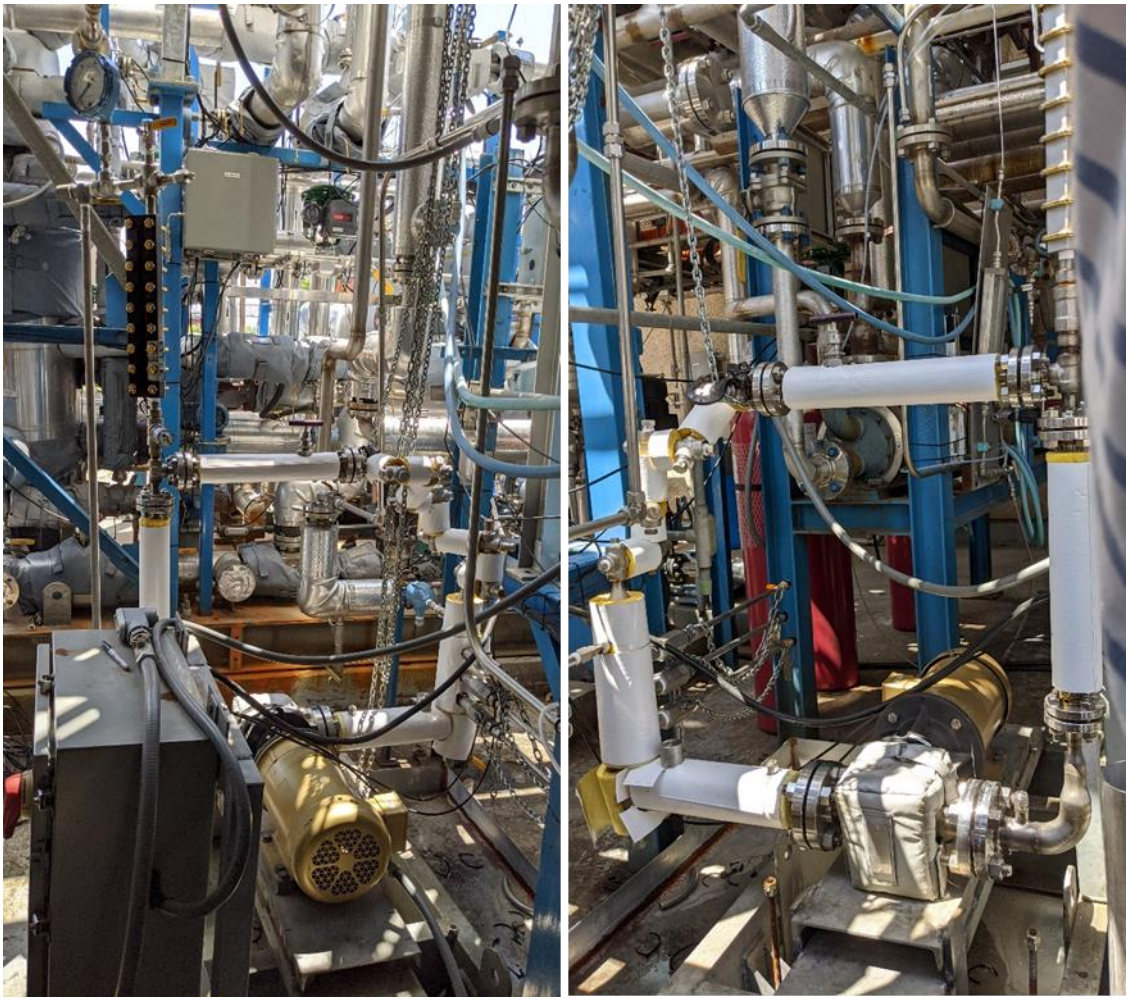

Figure 3-6: Front view (left) and back view (right) of the pump-around corrosion loop.

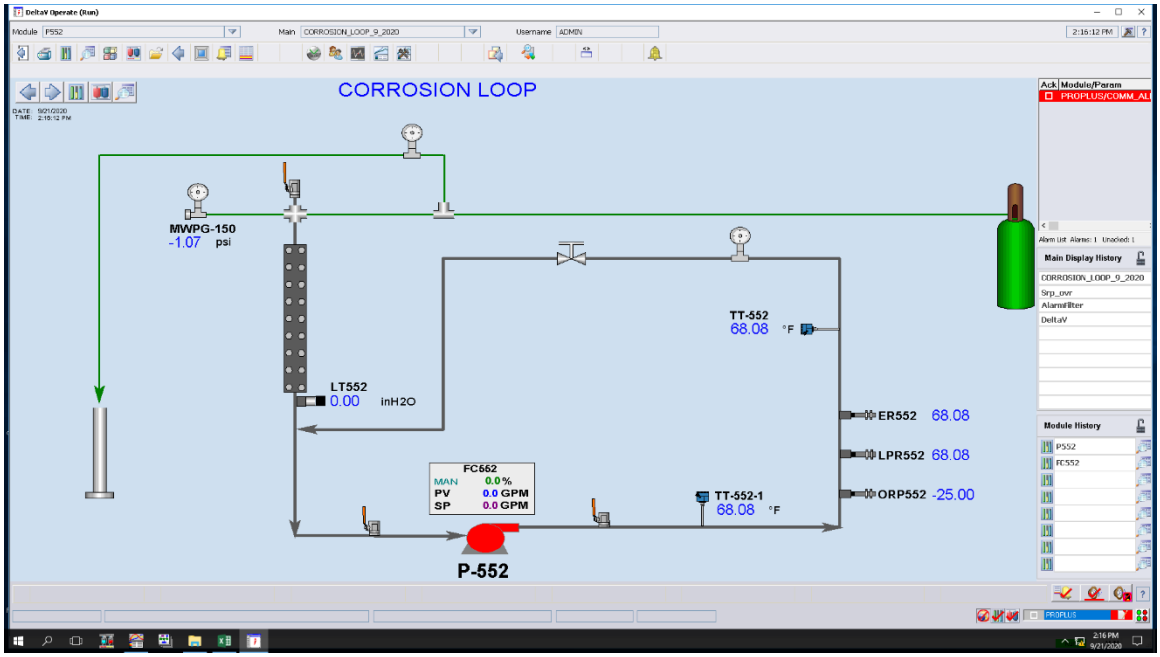

Figure 3-7: Process flow diagram and control interface of PACL in the DeltaV™ control system

3.3.3 Preparation of PZ Solutions

Fresh PZ solvents were prepared by dissolving anhydrous PZ solids (purchased from Sigma-Aldrich or Thermo Fisher Scientific; CAS No.: 110-85-0) in deionized water which is purified by a Millipore Direct-Q® deionization system to 18 MΩ·cm. All PZ solutions were prepared gravimetrically, and the PZ concentration is reported in molality (m), which is defined as moles of PZ per kilogram of water. CO_2 from a compressed cylinder was then bubbled into the PZ solutions through a gas dispersion tube with a porous tip (Ace Glass Inc.). The increase in the mass of PZ solutions during the sparging procedure was recorded to determine the amount of CO_2 added. The CO_2 content in a PZ solution is reported as CO_2 loading (α), which is defined as moles of CO_2 per mole alkalinity of PZ in solution.

Some experiments are performed using solvent samples from pilot plants. The Tarong PZ was collected at the CSIRO Tarong pilot plant, Australia in 2011 and diluted to 3 m for transportation and storage. The NCCC PZ was taken at the end of the pilot plant campaign at the National Carbon Capture Center (NCCC) in Alabama, USA in 2019. Detailed operation at the pilot plants and analytical results of the solvent samples can be found in literature (Cousins et al., 2012; Cousins et al., 2015; Rochelle et al., 2019; Rochelle et al., 2021; Wu et al., 2021). The pilot plant samples are blended with fresh PZ solution or sparged with CO_2 to get desired PZ concentrations and loadings.

3.3.4 Cation Ion Chromatography

The concentration of PZ is measured by the Dionex ICS-6000 ion chromatograph. The injected sample is first sent to a suppressor to remove anions. Then the flow stream exiting the suppressor goes through an IonPac CG17 guard column to remove contaminants and an IonPac CS17 analytical column where the primary separation occurs. The eluent contains various concentrations of methanesulfonic acid in water generated by an eluent generator. The sample is then sent to a conductivity detector, and the measured conductivity output is recorded in Chromeleon™ software and converted to concentrations of compounds of interest based on the calibration curves of concentrations and peak areas of measured conductivity.

3.3.5 Total Inorganic Carbon (TIC)

The concentration of CO_2 in PZ solutions is determined by total inorganic carbon (TIC). The loaded PZ solution is injected into a glass tube filled with 15% H_3PO_4 to release CO_2. The released CO_2 then travels with an N_2 carrier gas to the Horiba VIA 510 infrared CO_2 analyzer. The resulting change in voltage detected by the CO_2 analyzer produces

peaks. The peak areas are calculated and converted to CO_2 concentration using a calibration curve produced with a 1000 standard inorganic carbon solution, which is a mixture of K_2CO_3 and $KHCO_3$ (Ricca Chemical Company). CO_2 loading (mol C/mol N) is calculated from the CO_2 concentration by TIC, and PZ concentration by ionic chromatography.

3.3.6 pH Measurement

PZ solution samples are collected after each experiment and stored in plastic sample vials. The pH of the samples is measured at room temperature (~25 °C) using an Oakton 150 pH meter equipped with a single-junction pH electrode (Ag/AgCl reference). Two-point calibration using buffer solutions of pH 4 and 7 is performed daily before measuring sample pH.

3.4 RESULTS AND DISCUSSION

3.4.1 Effect of PZ Concentration on Carbon Steel Corrosion in PZAS Absorber and Water Wash

The water wash captures volatile amines and amine aerosols from the absorber outlet gas before it is released to the atmosphere. The water wash solution usually contains very little PZ (<1 m), and the PZ concentration is dependent on the operating temperatures in the absorber and water wash columns. When the absorber is operated at higher temperature, more volatile PZ leaves from the absorber top and enters the water wash column. Meanwhile, higher water wash temperature leads to more water vapor leaving the water wash column with the CO_2-depleted flue gas. Therefore, PZ concentration in the water wash solution increases with increasing temperature in the absorber and water wash. The effect of PZ concentration on carbon steel corrosion at absorber and water wash conditions was investigated in the low-gas flow (LGF) reactor. The experiment conditions and results are tabulated in Table 3-1. Solvents from the Tarong and NCCC pilot plants

were diluted with DI water to PZ concentration over a range from 0 to 0.6 m. PZ solid was dissolved in the NCCC PZ to increase the concentration to 5 m. Higher temperature may induce higher corrosion, and therefore the reactor temperature was kept at 55 – 60 °C, which was on the higher side of typical operating temperature of the PZAS absorber and water wash. CO_2 was blended with air or N_2 to make an inlet gas containing 1.5% CO_2, which represent the outlet gas composition of an absorber treating a coal flue gas (1.2%).

Table 3-1: Experiments on effect of PZ concentration on C1010 corrosion in low-gas flow reactor

PZ concentration (m)	PZ	Temperature (°C)	Gas	Corrosion rate (μm/yr)	Solution pH
0	-	55	1.5% CO_2, air	681	6.4
0.001	NCCC	60	1.5% CO_2, air	254	8.4
0.001	Tarong	60	1.5% CO_2, air	747	8.9
0.001	Fresh	60	1.5% CO_2, air	472	8.0
0.003	Tarong	60	1.5% CO_2, air	48	9.4
0.01	Tarong	60	1.5% CO_2, air	21	9.6
0.01	NCCC	60	1.5% CO_2, air	42	9.8
0.1	NCCC	60	1.5% CO_2, air	13	10.0
0.6	NCCC	55	1.5% CO_2, air	3	10.0
5	NCCC	60	1.5% CO_2, air	1	10.2
0.001	NCCC	60	1.5% CO_2, N_2	85	7.3
0.003	NCCC	60	1.5% CO_2, N_2	121	7.8
0.01	NCCC	60	1.5% CO_2, N_2	27	8.4
0.1	NCCC	60	1.5% CO_2, N_2	6	9.1
0.6	NCCC	60	1.5% CO_2, N_2	8	9.4
5	NCCC	60	1.5% CO_2, N_2	1	9.7

Figure 3-8 shows the effect of PZ concentration on C1010 carbon steel corrosion. The highest corrosion rate was 747 μm/yr, measured in 0.001 m Tarong PZ sparged with the CO_2/air mixture. The rate was comparable to that measured from an experiment done with DI water (681 μm/yr), suggesting 0.001 m PZ was not sufficient to cause significant change in liquid corrosivity. As PZ increased to 0.003 m, the corrosion rate significantly

dropped to 48 μm/yr and could be categorized as acceptable corrosion performance (< 300 μm/yr). The corrosion rate kept decreasing as the PZ increased further. CS corrosion in 5 m PZ was almost negligible at the test conditions, indicating the risk of corrosion is very low in the PZAS absorber. The correlation between C1010 corrosion rate (CR) and PZ molality (C_{PZ}) is given in Equation 1. When the solution was sparged with the CO_2/N_2 gas mixture, the corrosion rate still followed the general trend, suggesting that the presence of oxygen in the gas phase may not have a significant effect on carbon steel corrosion at absorber and WW conditions.

$$CR = 2.4 \times C_{PZ}^{-0.68} \tag{3-7}$$

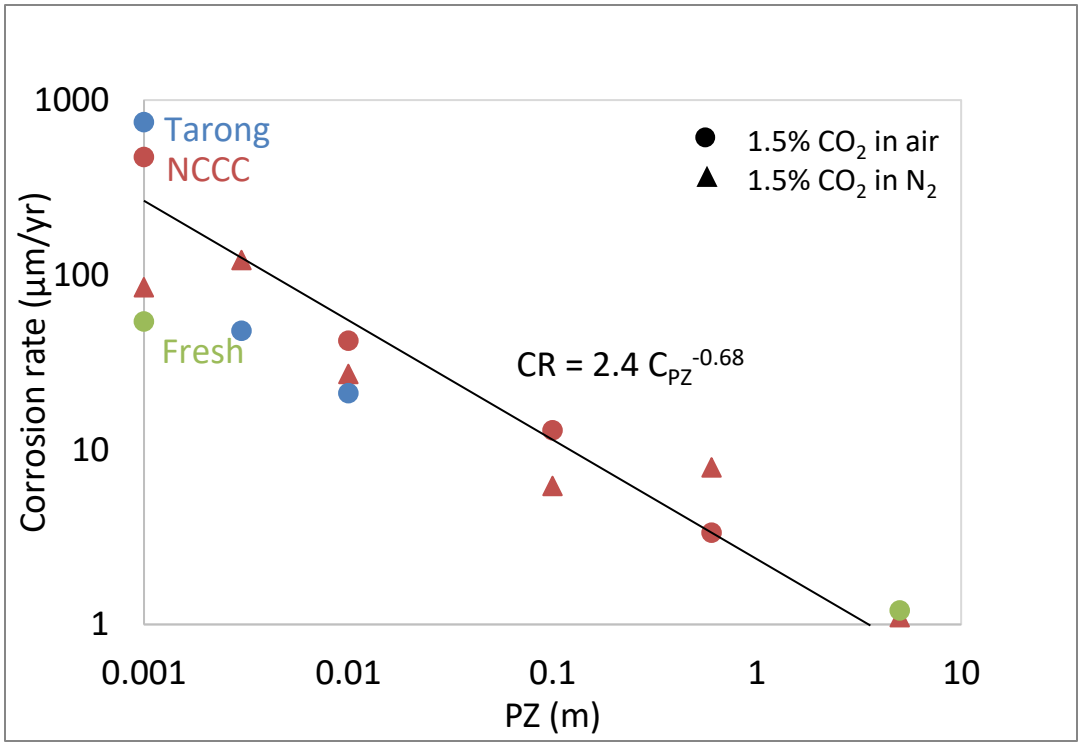

Figure 3-8: C1010 corrosion rates measured in experiments with a mixture of 1.5% CO_2 in air or N_2 as inlet gas at 60 °C

The pH of the PZ solutions was measured after each experiment at 25 °C (room temperature), and the results are given in Figure 3-9. The pH increased at higher PZ concentration, as expected. The lower corrosion rate in more concentrated PZ can be attributed to the reduced acidity by the addition of PZ. As the solution became less acidic, fewer protons were available for the cathodic corrosion reaction to occur, resulting in lower corrosion rates. The measurement of pH provides a simple way of differentiating between PZ solutions that are corrosive and non-corrosive to C1010. Below a critical pH value near 9 (represented by a red dashed line in Figure 3-9), C1010 corrosion was above the 300 μm/yr standard and was unacceptable. As more PZ was added, and the pH was above the critical value, C1010 performed well. Therefore, from a technical viewpoint, pH measurement of the water wash solution can be an easy tool for monitoring CS corrosion in the water wash during operation.

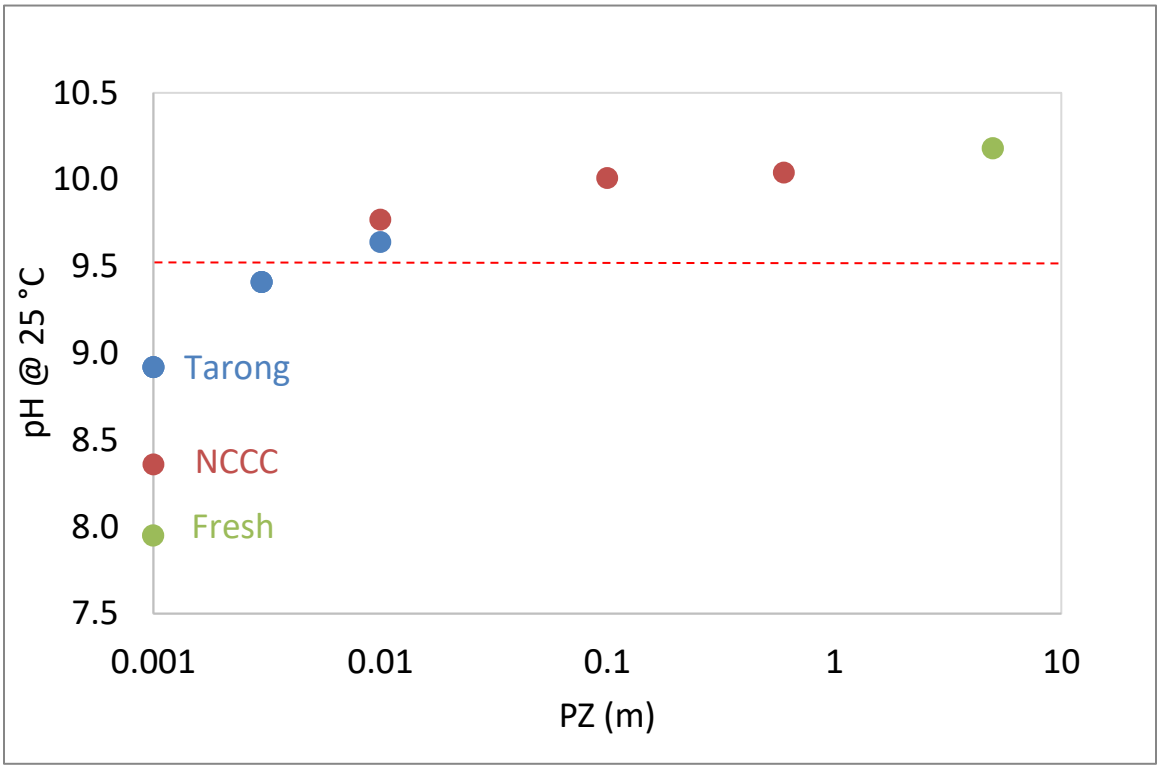

Figure 3-9: pH of PZ solutions from experiments with 1.5% CO_2 in air mixture as inlet gas at 60 °C; a critical pH marked by the red dashed line.

3.4.2 Effects of temperature and loading on C1010 corrosion in the absorber and WW

The temperature effect on C1010 corrosion at water wash conditions was studied between 40 and 75 °C. 0.01 m PZ was selected to represent water wash conditions. The experimental conditions are summarized in Table 3-2, and the results are presented in Figure 3-10. The corrosion rate increased when temperature increased from 40 to 60 °C, but it decreased as temperature further increased to 70 and 75 °C. There could be two things driving corrosion in different directions: 1. corrosion reactions are typically faster at higher temperature if other variables are constant, resulting in the increase in corrosion rate from 40 to 60 °C; 2. at a constant P_{CO2} (1.5% CO_2, 1 atm), loading decreased from 0.41 to 0.37

when temperature increased from 40 to 75 °C. Less CO_2 in the solution could lead to lower acidity or lower concentration of CO_2 species that are corrosive. Therefore, for 0.01 m PZ at 60–75 °C, loading could be playing a more significant role than temperature itself.

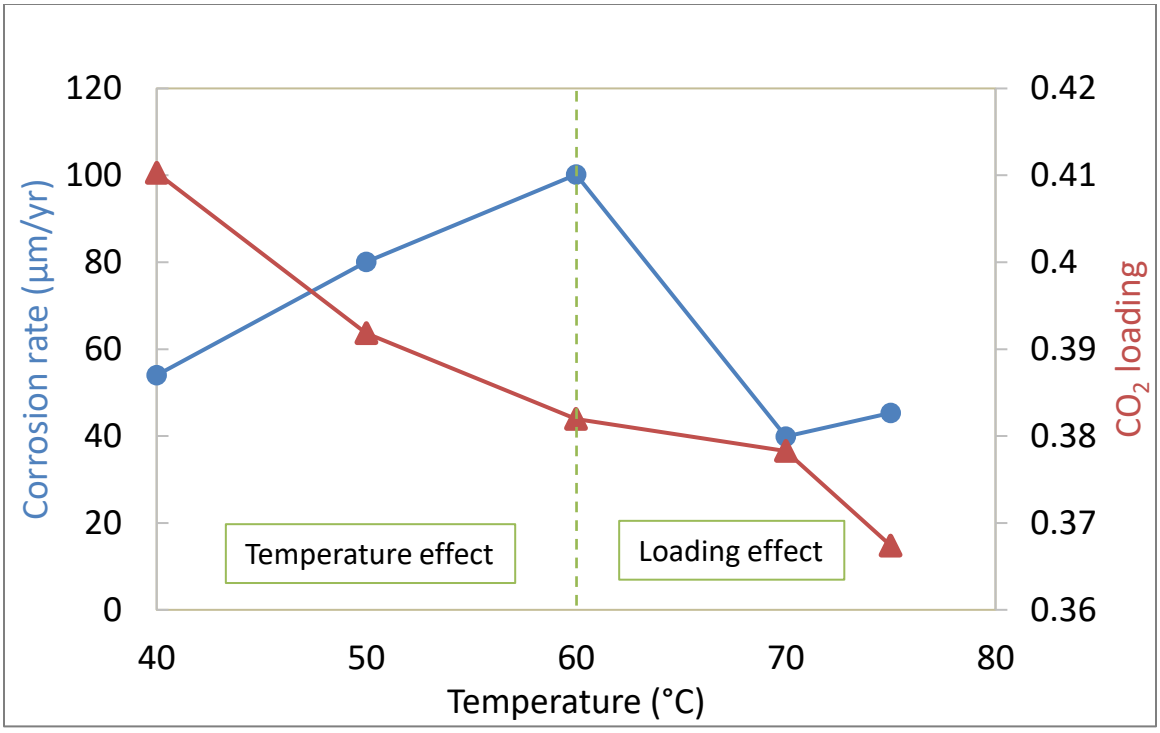

Figure 3-10: Temperature effect on C1010 corrosion (primary y-axis) and CO_2 loading (secondary y-axis).

The effect of CO_2 loading was studied by varying the CO_2 content in the inlet gas mixture from 0.04% (400 ppm CO_2 in the atmosphere) to 12%. Experiments were conducted at temperatures ranging from 40 to 75 °C. 0.01 m and 5 m PZ represent water wash and absorber conditions, respectively. A summary of the experiments is given in Table 3-2 and Figure 3-11. The corrosion rate of C1010 increased with increasing loading. The increase in corrosion rate was more significant for 0.01 m PZ, and it was as high as 574 µm/yr when 0.01 m PZ was saturated to 12% CO_2 at 60 °C. This suggests that even

though 0.01 m PZ might be sufficient to protect carbon steel under normal water wash operating conditions, letting untreated flue gas with high CO_2 content into the water wash during system shutdowns or by accident might cause serious corrosion. The regression of corrosion rate on loading and temperature is given in Equation 3-8 with an R^2 of 0.80.

$$\ln(CR) = 8.5(Ldg) - 3337.8\left(\frac{1}{T} - \frac{1}{333}\right) + 0.93 \quad (3\text{-}8)$$

where:

CR = corrosion rate (μm/yr)

Ldg = CO_2 loading (mol CO_2/mol alkalinity)

T = temperature (K)

Table 3-2: Experiments on effect of temperature and loading on C1010 corrosion in low-gas flow reactor

PZ concentration (m)	PZ	Temperature (°C)	P_{CO2} (atm)	Loading	Corrosion rate (μm/yr)
0.01	NCCC	40	0.0004	0.191	8
0.01	NCCC	40	0.015	0.410	54
0.01	NCCC	40	0.12	0.508	85
0.01	NCCC	50	0.015	0.392	80
0.01	NCCC	60	0.0004	0.180	11
0.01	NCCC	60	0.015	0.317	42
0.01	NCCC	60	0.04	0.356	48
0.01	NCCC	60	0.12	0.489	574
0.01	NCCC	70	0.015	0.378	40
0.01	NCCC	75	0.0004	0.191	34
0.01	NCCC	75	0.015	0.367	45
0.01	NCCC	75	0.12	0.429	136
5	NCCC	40	0.04	0.389	17
5	NCCC	40	0.12	0.418	25
5	NCCC	60	0.0004	0.161	15
5	NCCC	60	0.015	0.266	26
5	NCCC	60	0.04	0.303	19
5	NCCC	60	0.12	0.36	94
5	NCCC	75	0.0004	0.129	8
5	NCCC	75	0.12	0.351	62

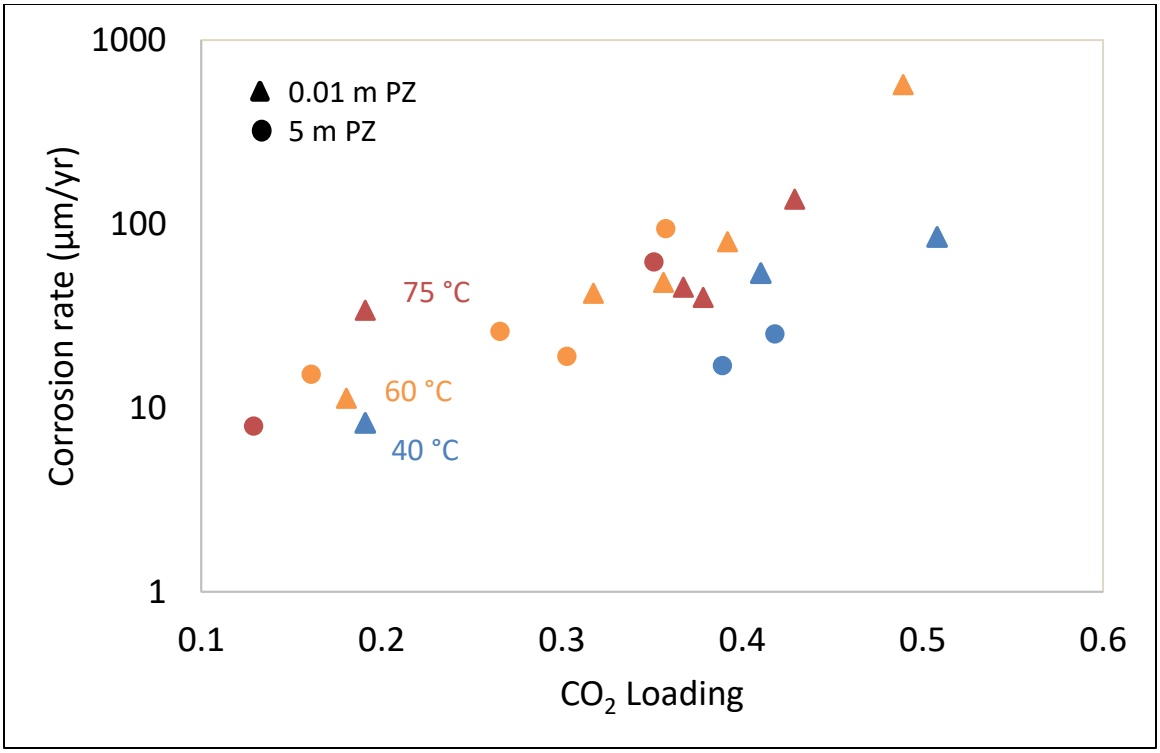

Figure 3-11: Effects of loading and temperature on C1010 corrosion at absorber and water wash conditions

3.4.3 Effect of Flow Velocity on Carbon Steel Corrosion in the PZAS Absorber and Water Wash

The effect of flow velocity on carbon steel corrosion was studied in the pump around corrosion loop (PACL). The liquid flow rate was controlled by a variable speed gear pump and a needle valve. The flow rate was estimated using Equation 3-9. ΔP is the pressure drop across the needle valve, and C_v is the flow coefficient provided by the valve manufacturer. The PZ solvent was from NCCC 2019 campaign and used as received or diluted to 0.01 m to represent the absorber and WW conditions, respectively. Both 0.01 and 5 m solvents were preloaded to a loading of 0.4.

$$Q = C_V \sqrt{\frac{\Delta P}{SG}} \tag{3-9}$$

where:

Q: flow rate (GPM)

Cv: flow coefficient of valve

ΔP: pressure drop (psi)

SG: liquid specific gravity

The conditions and results of the experiments performed in the PACL are summarized in Table 3-3. Figure 3-12 shows the effect of flow velocity on CS corrosion in 0.01 m and 5 m PZ at 40 °C and 0.4 loading. Most of the corrosion rates in this plot were measured with cylindrical coupons at elbows, where higher flow turbulence existed and was expected to have more corrosion than in straight pipes. Flow velocity was varied between 0.6 and 3 m/s. Within the low velocity range (0.6–1.6 m/s), the corrosion rate of carbon steel in 0.01 m PZ was almost constant. The rate only increased slightly from 60 to 62 μm/yr. In the high velocity region (1.6–3.0 m/s), corrosion of CS increased more rapidly from 62 to 216 μm/yr. The corrosion rates measured in 5 m PZ showed a similar trend with flow velocity but generally lower than the rates measured in 0.01 m PZ. CS corrosion in 5 m PZ increased slightly from 29 to 38 μm/yr as flow velocity increased from 0.6 to 1.6 m/s. The rate increased to 108 μm/yr as velocity was further increased to 3.0 m/s.

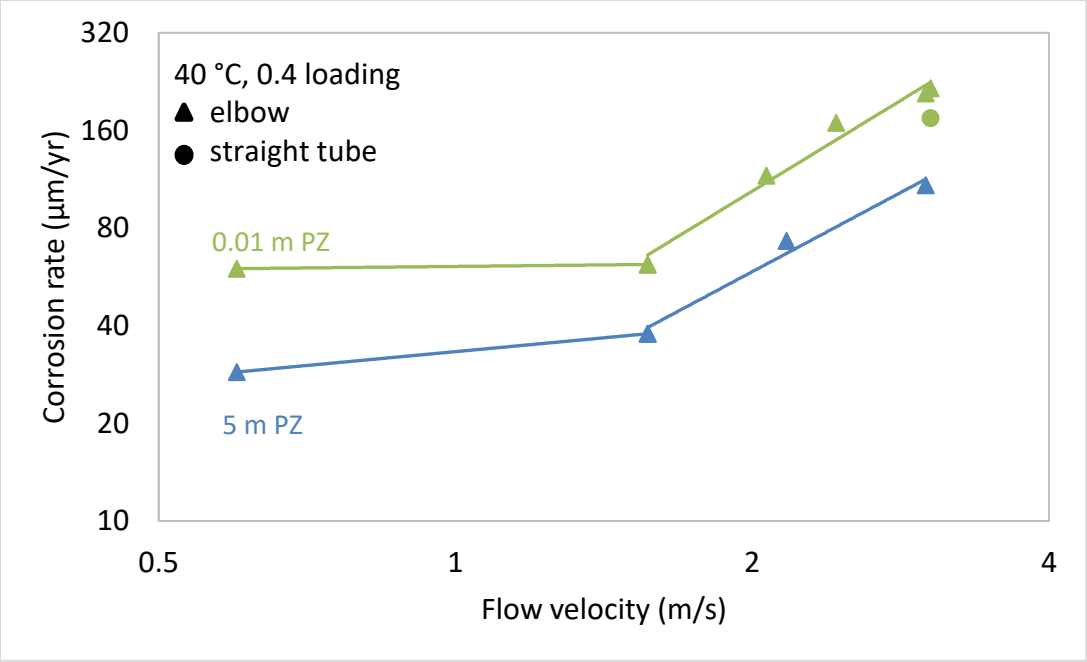

Figure 3-12: Effect of flow velocity on C1010 corrosion in the 0.01 m and 5 m PZ at 40 °C, 0.4 loading.

Figure 3-13 shows the effects of flow geometry in addition to the flow velocity effect in 5 m PZ. All experiments were performed with 5 m PZ from NCCC 2019 campaign, pre-loaded with CO_2 to a loading of 0.4. Two types of coupons, tube coupons and cylindrical coupons placed at elbows, were tested to evaluate corrosion in different flow geometries. Change in the flow direction causes extra turbulence in elbows. The CS corrosion rate measured at elbows at 60 °C increased from 75 to 167 µm/yr as flow velocity increased from 1.1 to 3.1 m/s. CS corrosion at straight pipe sections showed similar increasing trend with velocity but the absolute rate was lower (15–42 µm/yr). This suggests with other parameters remaining the same, extra turbulence inside an elbow caused higher corrosion.

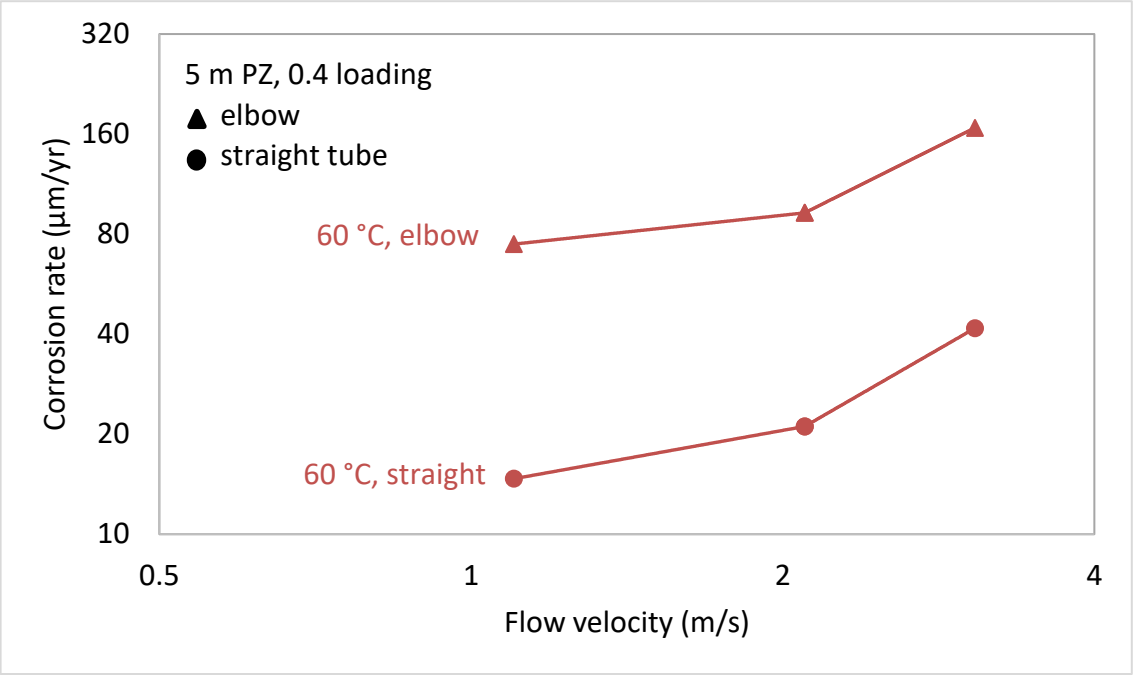

Figure 3-13: Effect of flow velocity on C1010 corrosion in 5 m PZ at 40–60 °C, 0.4 loading.

Table 3-3: Experiments on flow velocity effect on C1010 corrosion in pump-around corrosion loop

PZ (m)	Amine	Temperature (°C)	Loading	Flow Velocity (m/s)	Cylindrical coupon corrosion (μm/yr)	Tube coupon corrosion (μm/yr)	Density (kg/m^3)	Viscosity (cP)	Re	τ_w (N/m^2)
0.01	NCCC PZ	40	0.4	1.8	60		999	0.65	8153	1.5
0.01	NCCC PZ	40	0.4	4.7	62		999	0.65	21289	8.0
0.01	NCCC PZ	40	0.4	6.2	116		999	0.65	28084	13.0
0.01	NCCC PZ	40	0.4	7.3	169		999	0.65	33066	17.3
0.01	NCCC PZ	40	0.4	9	208		999	0.65	40767	25.0
0.01	NCCC PZ	40	0.4	9.1	216	175	999	0.65	41220	25.5
5	NCCC PZ	40	0.4	1.8	29		1194	3.61	9743	1.7
5	NCCC PZ	40	0.4	4.7	38		1194	3.61	25441	9.2
5	NCCC PZ	40	0.4	6.5	73		1194	3.61	35184	16.2
5	NCCC PZ	40	0.4	9	108		1194	3.61	48716	28.6
5	NCCC PZ	60	0.4	3.3	75	15	1194	2.23	17863	4.9
5	NCCC PZ	60	0.4	6.3	93	21	1194	2.23	34101	15.3
5	NCCC PZ	60	0.4	9.2	167	42	1194	2.23	49799	29.7

Flow-enhanced corrosion can result from the increase in mass transfer or shear stress on metal surface. Increased turbulence at high velocity will bring corrosive species closer to the wall where corrosion occurs, making the mass transfer boundary layer thinner, the concentration gradient higher and the resulting in higher mass transfer rate. However, in a mass transfer-controlled system, corrosion typically shows more rapid increase in the low velocity region and reaches a plateau at higher velocity (Fontana, 1986; Fakeeha et al., 1996). The shape of curves in Figure 3-12 does not match a typical mass transfer-controlled corrosion system. Another possible explanation for the velocity effect is the increase in shear stress. Higher turbulence and mixing in the bulk will bring the faster moving solvent closer to the wall, making the hydrodynamic boundary layer thinner, and resulting in a higher velocity gradient and therefore higher wall shear stress. Shear stress (τ_w) in 1/2" NPT pipes at each experiment condition listed in Table 3-3 was estimated using Equation 3-10.

$$\tau_w = f\frac{\rho v^2}{2} \tag{3-10}$$

where:

τ_w = wall shear stress (N/m^2)

ρ = fluid density (kg/m^3)

v = mean flow velocity (m/s)

f = Fanning friction factor

The Fanning friction factor for a turbulent flow system with Reynolds number (Re) between 2100 to 100000 can be estimated using the Patel's correlation (Equation 3-11):

$$f = \frac{0.79}{Re^{0.25}} \tag{3-11}$$

High shear stress may remove adsorbed organic compound or corrosion product films from the metal surface and expose the raw substrate to the corrosive environment. Organic compounds with N, O, and S functional groups can be adsorbed on steel surface and some have demonstrated great ability of inhibiting corrosion in oil and gas industry. In PZ solvent, PZ itself along with other PZ-derivative species or degradation products might have similar adsorption behavior. At low velocities, PZ species may be adsorbed on the carbon steel surface and protect it from corrosion. As velocity increases to a critical velocity, the adsorbed compound films may be removed or ruptured by the highly turbulent flow environment, causing the increase in corrosion rate. On the other hand, shear stress required to remove corrosion products (iron oxides, iron carbonate, etc.) is typically in the order of mPa (Gao et al, 2008; Yang et al. 2010), which is several orders of magnitude higher than the calculated wall shear stress at the experiment conditions. Therefore, mechanical removal of corrosion products is not likely the cause of the flow-enhanced corrosion.

3.4.4 Stainless Steel Corrosion in PZAS Absorber and Water Wash

Corrosion of three stainless steels (304L, 316L, and 430) was evaluated at representative absorber and water wash conditions. The experiment conditions and corrosion rate are summarized in Table 3-4. All three stainless steel performed very well (<56 μm/yr) at the conditions evaluated (0–5 m PZ, 40–60 °C, 0.04–18% CO_2).

Table 3-4: Stainless steel corrosion at PZAS absorber and water wash conditions

Material	PZ (m)	Temperature (°C)	Inlet Gas	Corrosion rate (μm/yr)
304L	0	55	1.5% CO_2, air	<1
	0	60	air	<1
	0.001	40	18% CO_2, N_2	<1
	0.001	40	1.5% CO_2, air	10
	0.001	60	1.5% CO_2, air	4
	0.003	40	18% CO_2, N_2	<1
	0.003	60	air	<1
	0.01	60	1.5% CO_2, air	2
	0.01	60	1.5% CO_2, air	7
	0.1	60	1.5% CO_2, air	56
	0.6	55	1.5% CO_2, air	<1
	5	40	18% CO_2, N_2	<1
	5	40	1.5% CO_2, air	<1
316L	0.001	40	1.5% CO_2, air	<1
	0.003	40	18% CO_2, N_2	<1
	0.01	40	18% CO_2, N_2	<1
	5	40	1.5% CO_2, air	<1
430	0	55	1.5% CO_2, air	1
	0.001	40	18% CO_2, N_2	<1
	0.001	60	1.5% CO_2, air	<1
	0.01	60	1.5% CO_2, air	<1
	0.01	60	1.5% CO_2, air	1
	0.1	60	1.5% CO_2, air	<1
	0.6	55	1.5% CO_2, air	1
	5	40	18% CO_2, N_2	1

3.5 CONCLUSIONS

3.5.1 Carbon steel is a promising material candidate for 5 m PZ at absorber conditions and can also be used for the water wash with caution. Stainless steels (304, 316L, and 430) have excellent corrosion resistance at absorber and water wash conditions.

C1010 CS performs well (< 300 μm/yr) in 5 m PZ under normal operating conditions in a PZAS absorber (40–75 °C, 0.04–12% CO_2 in gas) and can be a good

candidate for construction material for the absorber. The low amine concentration and high level of dissolved CO_2 in the water wash can cause CS corrosion by carbonic acid. Some restrictions of operating conditions are required for a water wash built with CS. Stainless steels, including 304, 316L, and 430, all show great corrosion performance (<60 μm/yr), and are ideal materials for the PZAS absorber and water wash.

3.5.2 Carbon steel corrosion decreases as more PZ is present in solution. The decrease of solution corrosivity can be explained by the increase in solution pH.

C1010 carbon steel corroded significantly (~750 μm/yr) when the solution has lower than 0.003 m PZ with an inlet gas of 1.5% CO_2 in air at 60 °C. Corrosion rate decreases as the concentration of PZ in the solution increases. The correlation between C1010 corrosion rate (CR) and PZ molality (C_{PZ}) can be expressed as:

$$CR = 2.4 \times C_{PZ}^{-0.68}$$

As more PZ is added, the solution becomes less acidic, and fewer protons were available for the cathodic corrosion reaction to occur, and results in lower corrosion rates. pH measurement of the water wash solution can be an easy tool for monitoring CS corrosion in the water wash during operation.

3.5.3 0.01 m PZ can be sufficient to protect carbon steel at normal operating conditions for a PZAS water wash, but untreated flue gas with high CO_2 content might cause corrosion if entering the WW.

When the PZ concentration increases to 0.01 m, the performance of C1010 is acceptable (<300 μm/yr). Therefore, maintaining at least 0.01 m PZ in the water wash solution can allow for carbon steel construction of a PZAS water wash under normal operating conditions.

C1010 corrosion is a strong function of loading at absorber and water wash conditions. The dependence of corrosion rate on loading (ldg) and temperature (T) can be expressed as:

$$\ln(CR) = 8.5(ldg) - 3337\left(\frac{1}{T} - \frac{1}{333K}\right) + 0.9$$

3.5.4 Operating temperature in the water wash is varied to maintain water balance of the PZAS process. Data suggest 40 °C is the optimal operating temperature for the water wash.

Higher operating temperature in the water wash may cause higher corrosion by increasing the reaction kinetics. High temperature also results in lower equilibrium CO_2 content in solution and therefore may reduce corrosion. The experimental results suggest that 40 °C is a better operating temperature for the PZAS absorber and water wash than 60 or 75 °C.

Temperature affects PZ concentration in the water wash. When the absorber is operated at higher temperature, more volatile PZ leaves from the absorber top and enters the water wash column. Meanwhile, higher water wash temperature leads to more water vapor leaving the water wash column with the CO_2-depleted flue gas. Therefore, PZ concentration in the water wash is higher at higher temperature, which is expected to reduce CS corrosion.

3.5.5 Flow-enhanced corrosion of CS was observed in 0.01 m and 5 m PZ at high velocity.

Within the low velocity range (0.6–1.6 m/s), the corrosion rate of carbon steel in 0.01 m PZ was almost constant. In the high velocity region (1.6–3.0 m/s), corrosion of CS increased more rapidly. The corrosion rates measured in 5 m PZ showed a similar trend with flow velocity. Extra turbulence inside pipe elbows increases corrosion.

3.5.6 Stainless steels (304L, 316L, and 430) have excellent performance at absorber and water wash conditions.

Three stainless steels (304L. 316L. and 430) were evaluated at representative absorber and water wash conditions. All three materials exhibited very low corrosion rates (~1 μm/yr) with occasional higher but still acceptable corrosion (~50 μm/yr).

Chapter 4: Carbon Steel Protected by Siderite in the Advanced Stripper[6]

4.1 INTRODUCTION

PZ has been shown to have good corrosion performance at temperatures below 80 °C. Gunasekaran et al. (2013) compared the corrosivity of five single amines and several blends of two amines at CO_2 saturation and 80 °C. The corrosivity decreased in this order: MEA > AMP (2-amino-2-methyl-1-propanol) > DEA (diethanolamine) > PZ > MDEA (methyldiethanolamine), and PZ outperformed all the amine blends studied in that work.

Besides the intrinsically low corrosivity of PZ, previous research (Zheng et al., 2014a; Zheng et al., 2014b) demonstrated the passivity of CO_2-loaded PZ on carbon steel at 100 °C, while such passivity was not observed in MEA at comparable conditions. This passive film was characterized as siderite ($FeCO_3$) and considered the major contribution to the decrease in the corrosion rate by acting as a barrier between corrosion agents and steel surfaces.

$FeCO_3$ has been recognized as one of the corrosion products that can passivate on steel surfaces in acid gas treating plants. Although the protection of $FeCO_3$ is outperformed by FeS, another common passive corrosion product in gas sweetening applications, $FeCO_3$ plays a significant role in the corrosion of carbon steel in PCCC due to the lack of H_2S for FeS formation in the flue gas (Ikeda et al., 1985; Tomson and Johnson, 1991; Dunlop et al., 1983).

The mechanism of $FeCO_3$ formation has been studied extensively. Although no consensus has been reached on the detailed mechanism of $FeCO_3$ formation in amine−CO_2-water systems because numerous chemical/ electrochemical reactions and transport

[6] Part of this chapter has been published in "Liu C-T, Fischer KB, Rochelle GT. Corrosion of Carbon Steel by Aqueous Piperazine Protected by $FeCO_3$. Int. J. Greenh. Gas Control 2019, 85, 23–29." with Liu as the primary author.

processes can occur simultaneously, some systematic trends governing the formation and effectiveness of this passive film have been identified. High temperature and high concentration of Fe^{2+} and HCO_3^- are favorable for the film formation since it is a slow kinetic-based process which follows the Arrhenius equation of reaction rate. Other factors such as pH, fluid velocity, dissolved O_2, and amine type can also affect the formation rate and performance of the $FeCO_3$ film (Dugstad, 1998; Campbell et al., 2016; Zheng et al., 2016a; Zheng et al., 2016b).

Due to the case-sensitive nature of the $FeCO_3$ protective layer, and although the research on this layer has been done with several amines including MEA, MDEA, and DEA, a better understanding of its behavior in PZ is required for the Advanced Stripper. This work aims to study the effect of PZ degradation, which occurred in long-term plant operations, on the corrosion protection provided by $FeCO_3$ passive films. Most of the previous studies were done with electrochemical testing, which is constrained by some pressure limits and is difficult to utilize in pilot plants to conduct analogous measurements. This work used electrical resistance corrosion measurement along with coupons, which are widely used for in-line corrosion monitoring in various industries, to study the corrosion behavior. The corrosion loop apparatus also provided testing environments at elevated temperature and pressure with natural circulation inside the loop. This enabled the study of corrosion at stripper conditions.

4.2 EXPERIMENTAL METHODS

4.2.1 Electrical Resistance (ER) Probe

Some corrosion measurements were performed with electrical resistance (ER) probes. The detailed specification of ER probes used in this work has been documented by Fischer (2018). The ER probe exposes a metal wire to the PZ solvent. As the wire corrodes

by the solution, the cross-sectional area of the wire decreases, thus increasing resistance in the wire. Equation 4-1 shows the relationship between conductor resistance and its cross-sectional area.

$$R = \rho \frac{L}{A} \tag{4-1}$$

where:

R = conductor resistance

ρ = electrical resistivity

L = conductor length

A = conductor cross-sectional area

Two examples of the corrosion calculation are shown in Figure 4-1. Corrosion measurements typically lasted 7–24 h for high corrosion rates and 20–120 h for low corrosion rates. ER probes are connected to a transmitter which converted remaining thickness readings to 4-20 mA signals. The signals were recorded in the SignalExpress software by National Instrument™. The experiments took one remaining thickness (probe life remaining) reading per second, and this data was then directly regressed using the method of least square to determine a corrosion rate. ER probes were cleaned between experiments using concentrated HCl inhibited with N,N'-Dibutylthiourea as recommended in literature (Kayafas, 1980; NACE, 2013).

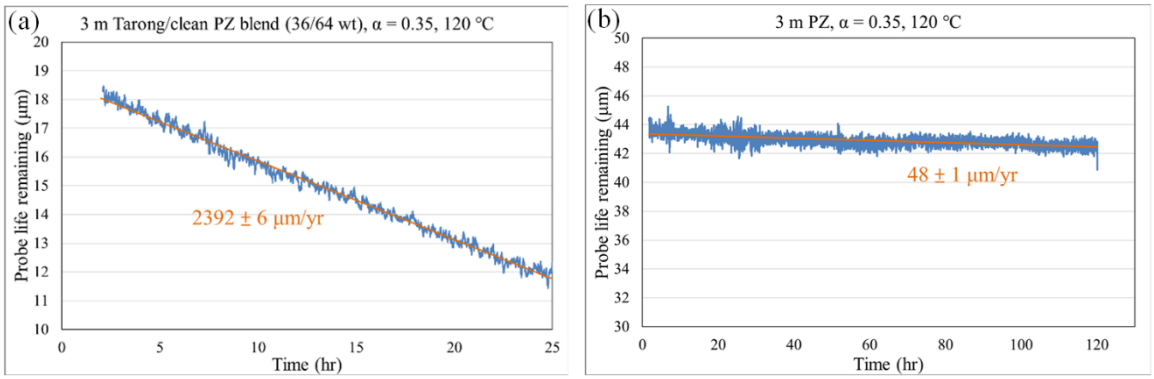

Figure 4-1: Examples of corrosion rate calculation from ER probe measurements: (a) high corrosion rate and (b) low corrosion rate. (Liu et al., 2019)

4.2.2 Corrosion Coupons

Corrosion coupons were used for corrosion rate measurements by weight loss and for corrosion product analysis. Strip coupons (Metal Samples CO1183750104110) and cylindrical coupons (Metal Samples CO2043770104100) in C1010 carbon steel were use in this study.

Once removed, coupons are rinsed with deionized water and acetone, photographed, and analyzed by a scanning electron microscope/energy dispersive X-ray spectroscopy and a surface profilometer. Afterward, corrosion products were scraped off and analyzed by powder X-Ray diffraction. After all surface characterization was done, residual corrosion products were removed using the same method for cleaning ER probes described in the previous section. After the corrosion products were removed, a final weight loss of coupons was measured. Finally, corrosion rate was calculated from the weight loss using Equation 4-2.

$$CR = 87600\,\frac{W}{DAT} \tag{4-2}$$

where:

CR = corrosion rate (μm/yr)

W = coupon mass loss (mg)

D = density of metal (g/cm^3)

A = surface area of coupon (cm^2)

T = duration of experiment (hours)

4.2.3 Corrosion Loop

Some experiments in this work were conducted in the corrosion loop shown in Figure 4-2. The details of this apparatus have been well documented by Fischer (2018). This apparatus was built for experiments at high temperature and high pressure at stripper conditions. The main body is a pressure vessel consisting of a 1-inch diameter pipe loop with a 1 1/2-inch diameter pipe headspace. The right side of the loop is wrapped in heat tape controlled by a PID controller. Temperature was measured at the upper right corner of the loop by a J-type thermocouple, which was connected to the PID controller. A temperature measurement was also taken at the lower left corner, and the temperature difference between these two sites varied from 70 to 97 °C. The uneven temperature creates a slow counter-clockwise flow inside the pipe loop due to natural convection. An ER probe along with up to two strip type coupons could be inserted at the upper right corner and collect data. The pipe headspace has a pressure gauge for pressure monitoring and a rupture disc to prevent over-pressurization. The loop was filled with 1000 mL PZ solution, sealed, and then heated to the target temperature. Once at temperature, the corrosion rate was measured for 7 hours to 124 hours. Experiments last 7–24 h for high corrosion rates and 20–120 h for low corrosion rates.

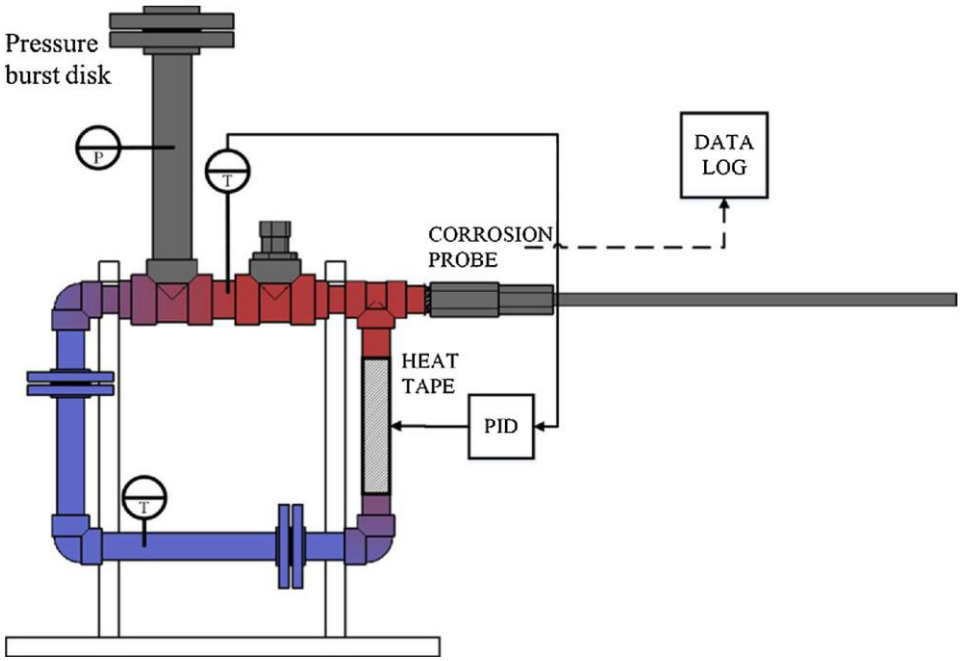

Figure 4-2: Corrosion loop apparatus (Liu et al., 2019)

4.2.4 Pump-Around Corrosion Loop (PACL)

A schematic of the new corrosion loop is given in Figure 3-5. The PACL mainly consists of a variable speed gear pump (CHEMSTEEL™ S923 M) and a pipe loop. The size of the pipe loop around the pump is 1.5" to match the pump connections. The rest of the pipe loop is reduced to 1/2" in order to allow higher flow velocity at a given flow rate and reduce total solvent inventory. One 3/4" and three 1" threaded NPT ports are installed on the 1.5" pipe section downstream of the pump to allow the insertion of corrosion and oxidation-reduction potential (ORP) probes. Immediately downstream of the corrosion probe location, there is a 1/8" Swagelok® port connected to a syringe pump (New Era Pump Systems Inc. NE-8000). This port allows for injection of liquids, such as oxidizer/reducer

liquid, into PACL during experiments. Cylindrical coupons (Metal Samples Co. ES204) are installed at the nine 4-way tees in the 1/2” pipe section to evaluate corrosion at pipe bends. A needle valve is installed on the top horizontal pipe section to control liquid flow rate and pressure drop. The section of 1.5” pipe downstream of the pump discharge is wrapped with a heating cable, which is controlled in the DeltaV™ Automation System by Emerson Electric Co. An armored level gauge (Jerguson Gage & Valve Co. 115R300L) and a vibrating fork level switch (Rosemount™ 2120D0DG1E7SA0000) on the upper left of the loop monitor the solvent inventory. The vertical section of pipe below the level gauge can be replaced by three sets of tube coupon assemblies for better study of corrosion on straight pipe walls. The tube coupons are made from 9/16” tubing to match the inner dimeter of 1/2” pipes, cut to desired length, cleaned with DI water and acetone, weighed, and mounted on flanges on both sides using Swagelok® NPT adapters. The materials of flanges and adapters are the same as the tube coupon material. The adjacent flanges from different assemblies are isolated by gaskets and bolt sleeves to avoid contact between different alloys. A N_2 line with a manual gas flow regulator, a 1-way check valve, and a back-pressure regulator are used to control system pressure. More details of the PACL and the standard operating procedures are given in Appendix A.

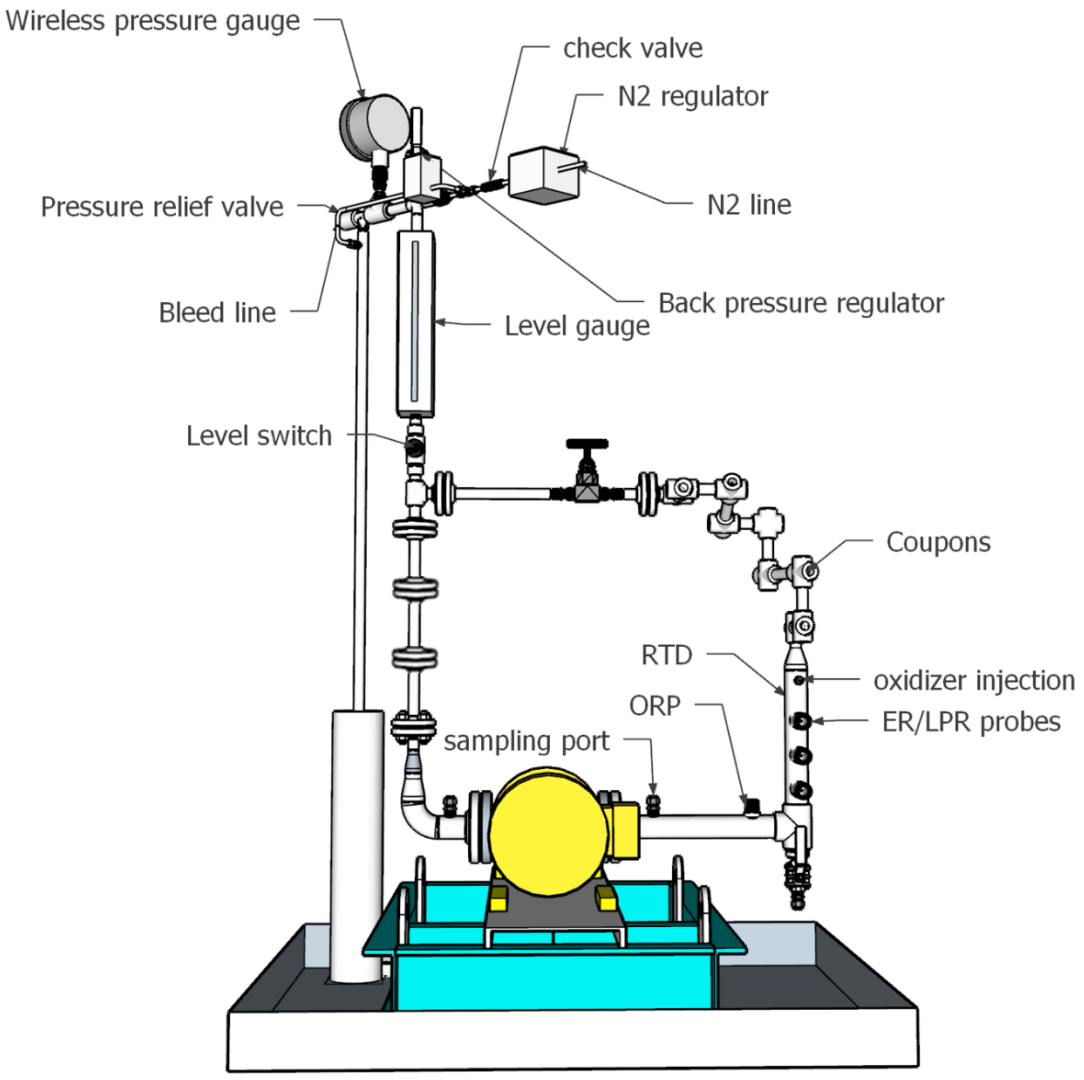

Figure 4-3: Pump around corrosion loop (PACL)

The liquid flow rate was controlled by a variable speed gear pump and a needle valve. The flow rate was estimated using Equation 4-3. ΔP is the pressure drop across the needle valve, and C_v is the flow coefficient provided by the valve manufacturer.

$$Q = C_V \sqrt{\frac{\Delta P}{SG}} \tag{4-3}$$

where:

Q: flow rate (GPM)

Cv: flow coefficient of valve

ΔP: pressure drop (psi)

SG: liquid specific gravity

4.2.5 Scanning Electron Microscopy/Energy-dispersive X-ray Spectroscopy (SEM/EDS)

Corrosion coupon surfaces were imaged using FEI Quanta 650 scanning electron microscope equipped with a Bruker EDS system for elemental mapping analysis. The characterization was carried out at a voltage of 20 kV and a current of 2 mA. The magnification was typically 100x-3000x.

4.2.6 Powder X-ray diffraction (XRD)

Corrosion product films were analyzed by powder X-ray diffraction using a Rigaku R-Axis Spider instrument with a Cu tube source at 40 kV and 40 mA. Reference spectra are given in Table 4-1

Table 4-1: References for corrosion product identification using powder XRD (Fischer, 2019).

Compound Name	Chemical Formula	Powder Diffraction File (PDF) #	Citation
Siderite	$FeCO_3$	00-029-0696	(NBS, 1978)
Iron	Fe	00-006-0696	(NBS, 1955)
Magnetite	Fe_3O_4	00-019-0629	(NBS, 1967)
Goethite	FeO(OH)	00-029-0713	(Harrison, 1975)
Ferric Hydroxide	$Fe(OH)_3$	00-038-0032	(Au-Yeung et al., 1984)

4.2.7 Cation Chromatography

PZ and ethylenediamine (EDA) were quantified with cation chromatography (Dionex ICS2100). The eluent consisted of methanesulfonic acid (MSA) and deionized water. The separation of ions was performed in an IonPac GC 17 guard column and an IonPac CS 17 analytical column. The samples were gravimetrically diluted to 6000X. EDA eluted at 28 min and PZ eluted at 33 min during a total run time of 50 min.

4.3 RESULTS AND DISCUSSION

4.3.1 Effect of Piperazine Degradation on Siderite Protective Films

A series of experiments were conducted to evaluate the effect of PZ degradation on the corrosion rate of C1010 CS at stripper temperature. Experiments were performed in the corrosion loop, and corrosion rates were measured with ER probes. Detailed experiment conditions and results are summarized in Table 4-2. The amines investigated include clean PZ, pilot plant PZ from the Tarong power plant in Queensland, Australia in 2011 (Tarong PZ), and two solvent samples from the 2018 pilot plant campaign at National Carbon Capture Center (NCCC) in Alabama, USA (NCCC628 & NCCC814). The characterization of these pilot plant solvents is fully documented in other publications (Nielsen et al., 2013; Wu et al., 2018). 3 m Tarong PZ and 5 m NCCC814 PZ were blended with 3 and 5 m clean PZ respectively to get different concentrations of degradation products.

Table 4-2: Effect of PZ degradation on C1010 carbon steel corrosion in the corrosion loop

Amine	Composition (wt %)[a]	Temperature (°C)	Loading (mol CO_2/mol alk.)	Corrosion rate (µm/yr)	Time (hr)	[EDA] (mmol/kg soln)	[EDA]/[PZ] ($\times 10^3$)
3 m Tarong/clean PZ blend	100	120	0.36	3246 ± 114	24	12.9	4.3
	60	120	0.35	4267 ± 16	23	8.4	3.6
	45	120	0.35	3517 ± 15	24	4.6	2.0
	45	120	0.35	2940 ± 7	24	5.7	2.5
	40	120	0.35	2392 ± 6	25	5.6	2.4
	40	120	0.34	3757 ± 9	20	6.0	2.6
	40	120	0.34	1678 ± 7	20	3.9	1.7
	36	120	0.36	18 ± 1	92	5.0	2.2
	30	120	0.36	3 ± 0	122	6.7	2.8
	20	120	0.36	48 ± 1	109	2.6	1.1
	0	120	0.35	42 ± 1	102	0.0	0.0
5 m NCCC628	-	120	0.25	2010 ± 6	24	13.0	4.1
	-	120	0.40	2360 ± 60	6	13.6	4.6
5 m NCCC814/ clean PZ blend	100	120	0.25	1160 ± 9	19	19.5	6.5
	50	120	0.25	919 ± 14	17	10.1	3.5
	30	120	0.25	12 ± 2	25	6.0	2.0
	20	120	0.25	0.2 ± 3	23	3.9	1.3
5 m clean PZ + EDA	-	120	0.25	2880 ± 64	6	15.2	6.3
	-	120	0.25	78 ± 9	18	6.2	1.9
	-	120	0.25	122 ± 9	20	5.9	1.7
	-	120	0.25	71 ± 6	19	6.5	1.9
	-	120	0.25	41 ± 2	21	12.1	3.5
	-	120	0.25	587 ± 22	12	17.8	5.0

[a]weight percent of Tarong PZ or NCCC PZ in the blends

Figure 4-4 summarizes the corrosion rate measured by ER probes with different levels of degradation products at 120 °C. The concentration of ethylenediamine (EDA), which is one of the major degradation products of PZ, is normalized by PZ concentration and used to represent the degree of degradation. For the experiments using the blends of 3 m Tarong and clean PZ with loading of 0.35, the corrosion rate of CS1010 was low (< 80 μm/yr) when [EDA]/[PZ] (mol/mol) in the solvent was less than 1.8×10^{-3} but increased to ~2400 μm/yr when [EDA]/[PZ] was 2.4×10^{-3} and remained at the same order of magnitude after that. The discontinuity of corrosion behavior is clearly seen at a critical [EDA]/[PZ] range of 1.8×10^{-3} to 2.4×10^{-3}. A similar step change of corrosion rate was obtained from the experiments using the blends of 5 m NCCC814 and clean PZ, where the corrosion rate increased from 12 μm/yr to 919 μm/yr when [EDA]/[PZ] was between 2.0×10^{-3} and 3.5×10^{-3}. This drastic change in corrosion rate suggests that a corrosion issue in a CCS plant may arise as the solvent degrades during a long period of operation.

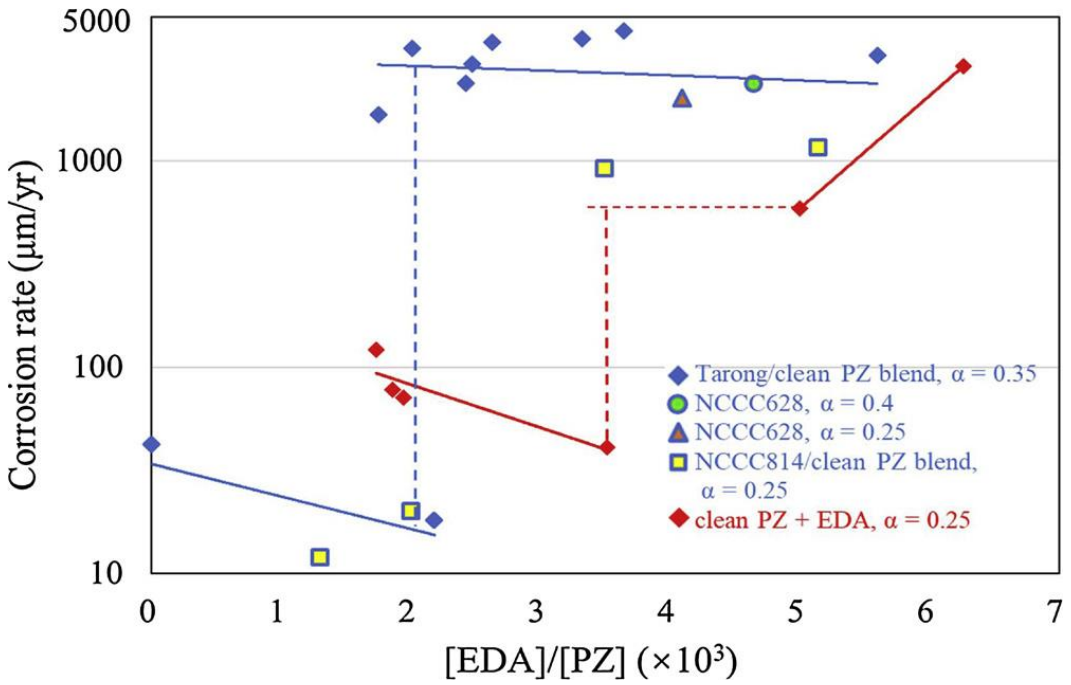

Figure 4-4: Corrosion of CS1010 with different levels of degradation products in aqueous PZ at 120 °C. (Liu et al., 2019)

To further understand the effect on carbon steel corrosion caused solely by EDA, 5 m clean PZ with the addition of different levels of EDA was investigated with the same technique at 120 °C with loading of 0.25. The relationship between the measured corrosion rate and the concentration of EDA is shown in Figure 4-4. With [EDA]/[PZ] lower than 3.5×10^{-3}, the corrosion rate remained low (<14 μm/yr) and began to increase rapidly as [EDA]/[PZ] exceeds a critical value between 3.5×10^{-3} and 5.0×10^{-3}. Although the corrosion rate in this solvent did not change as quickly as it did in the two pilot plant/clean solvent blends, the change was still significant, suggesting that EDA could either be one of the major corrosion agents in degraded PZ or a surrogate for the effect of degradation products on carbon steel corrosion.

To study the effect of corrosion product films on the change in corrosion rate, the corrosion products were scraped off the CS1010 coupons and analyzed with XRD. The

diffraction patterns of six representative coupons, including two samples—one on each side of the step change boundary—from three series of experiments with different PZ blends (Tarong/clean PZ, NCCC814/clean PZ, and clean PZ + EDA) are shown in Figure 4-5. The ones on the left side of the boundary (low [EDA]/[PZ], low corrosion rates) are noted as protected and the others (high [EDA]/[PZ], high corrosion rates) as corroded. The XRD analysis shows that siderite ($FeCO_3$) was the major corrosion product on all CS1010 coupons, regardless of the different corrosion rates. The only difference between the corroded and protected samples was that the corroded samples had a larger peak of iron (Fe) at a 2θ value of 44.6˚. This suggests that although siderite films formed on all the coupons, the films on the corroded coupons might be incomplete or thin, resulting in steel being exposed to the corrosive solvent.

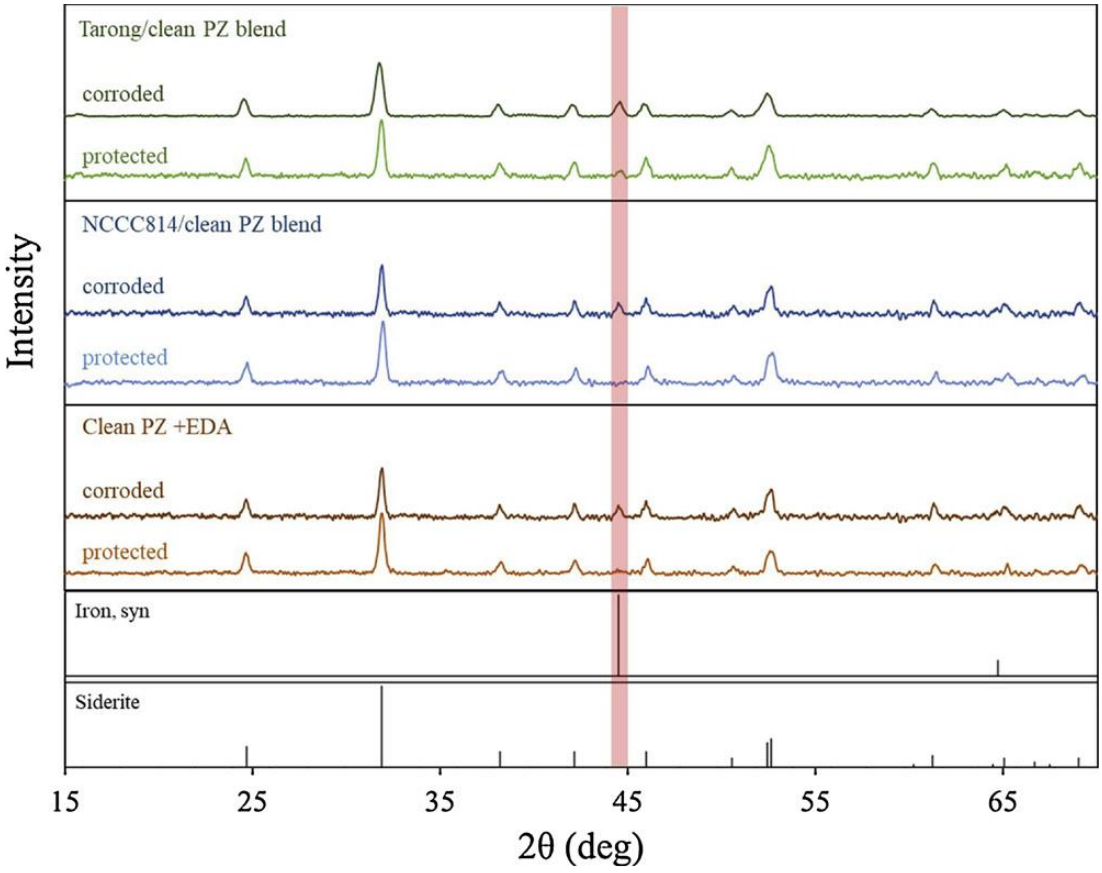

Figure 4-5: XRD patterns of corrosion products on six representative CS1010 coupons (Liu et al., 2019)

SEM was used to examine the surface of the C1010 coupons. Figure 4-6 shows the SEM images of the six representative coupons: (a) and (b) were from the Tarong/clean PZ blend experiments; (c) and (d) were from the NCCC814/clean PZ blend experiments; (e) and (f) were from the clean PZ + EDA experiments. Images in the left column (a, c, and e) are protected, while those in the right column (b, d, and f) are seriously corroded. Although the XRD analysis suggests that siderite ($FeCO_3$) was the major corrosion product on the surface of all these coupons, the appearance of the siderite crystals was different in the SEM images. The protected coupons (a, c, and e) were covered by a compact layer of

siderite crystals. No significant deficit of the films or exposed steel metal was. For the corroded coupon from the Tarong/ clean PZ blend experiment (b), the crystal sizes were less uniform than on the protected one (a), and there were some gaps between the crystals. The small crystals on top of the large ones might result from the dissolution of $FeCO_3$ or the erosion caused by liquid flow inside the corrosion loop. The damaged siderite films might be porous and thus have lost of the ability to block the diffusion of corrosive agents to the metal surface. Similar deficits can be found on Figure 4-6(d) and (e). Figure 4-6(g) and (h) show the cross-sectional images of the coupons in (a) and (b) respectively. The grey layers between the steel substrates and the black epoxy layers are the siderite passive films of interest. The protected coupon (g) has a complete film with a thickness of 6 μm on top of the steel surface, while the corroded one (h) was not fully covered. The siderite crystals on top of the corroded coupon did not form a compact layer. Instead, the outline of each crystal is still observable, and the gaps between the crystals may serve as passages that allow for the diffusion of corrosive species to the metal surface. The incomplete film was not able to provide protection to carbon steel, and it might further induce localized corrosion of the exposed area (Nyborg et al., 1998). EDA has been recognized as a corrosion inhibitor in aqueous solutions by adsorption on metal surfaces (Hackerman et al., 1954; McCafferty et al., 1972; Danaee et al., 2012). The adsorbed EDA forms a film and protects the metal by increasing the electrical resistance at the liquid-metal interface. In our case, however, the adsorption of EDA may interfere with the formation of $FeCO_3$ protective film. Assuming the ferrous required for $FeCO_3$ to precipitate comes from a short period of initial corrosion of the steel before it is fully covered by the siderite film, the adsorbed EDA may reduce the concentration of ferrous ions near the metal surface and therefore impede the growth of the siderite film. Such competition between the formation of siderite and EDA films results in neither of these two films providing adequate

protection to the underneath steel. This destructive interaction between siderite and several corrosion inhibitors has been reported (Sun et al., 2004; Chokshi et al., 2005; Sadeek et al., 2018).

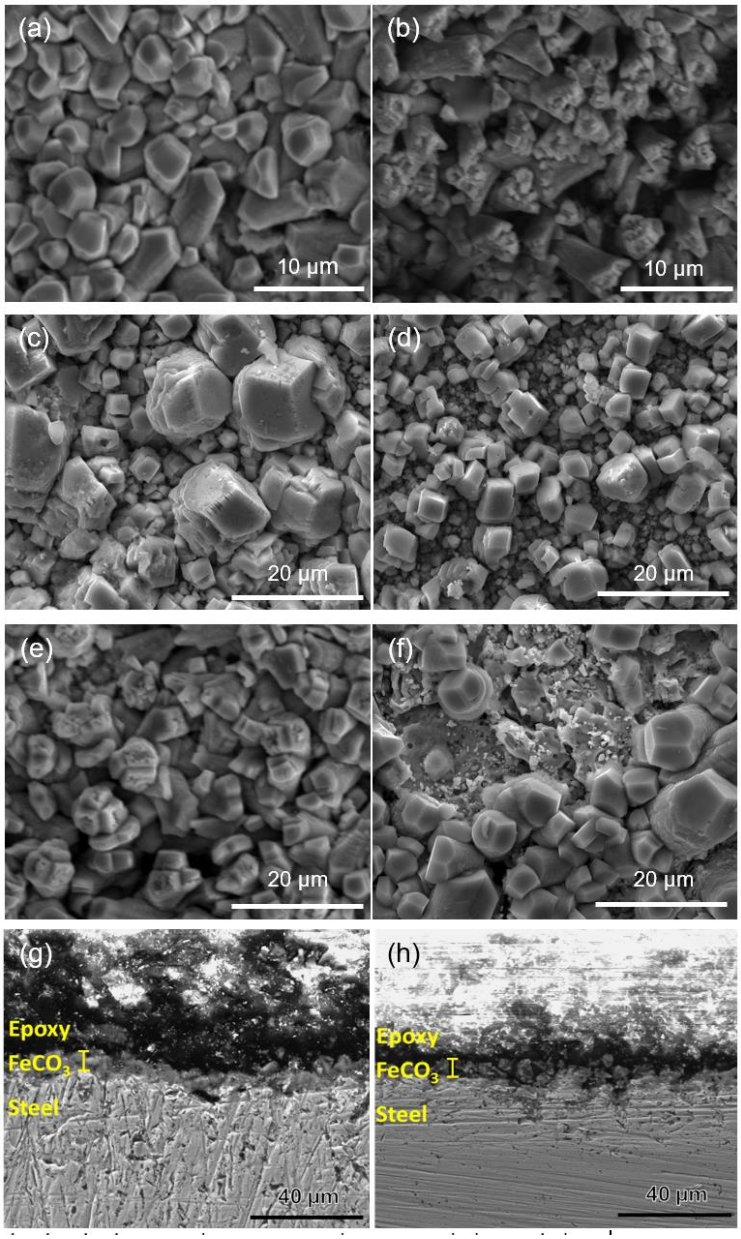

Figure 4-6: SEM images of the corrosion products on (a) protected coupon in 3m Tarong/clean PZ blend (36/64 wt); (b) corroded coupon in 3m Tarong/clean PZ blend (60/40 wt); (c) protected coupon in 5m NCCC814/clean PZ blend (20/80 wt); (d) corroded coupon in 5m NCCC814/clean PZ blend (50/50 wt); (e) protected coupon in 5m clean PZ+12 mmol/kg EDA; (f) corroded coupon in 5m clean PZ+18 mmol/kg EDA; cross-sections of (g) protected coupon in 3m Tarong/clean PZ blend (36/64 wt) and (h) corroded coupon in 3m Tarong/clean PZ blend (60/40 wt).

The temperature dependence of the high corrosion rates on the right-hand side of the discontinuity boundary (high EDA content) was investigated over a range of 80–150 ℃. Figure 4-7 shows the activation energy as a function of the corrosion rate at 120 ℃ calculated from the Arrhenius equation. For the cases with corrosion rates higher than 1000 μm/yr, the activation energies ranged from 26 to 53 kJ/mol, while no clear systematic correlation between the activation energy and the calculated corrosion rate was observed.

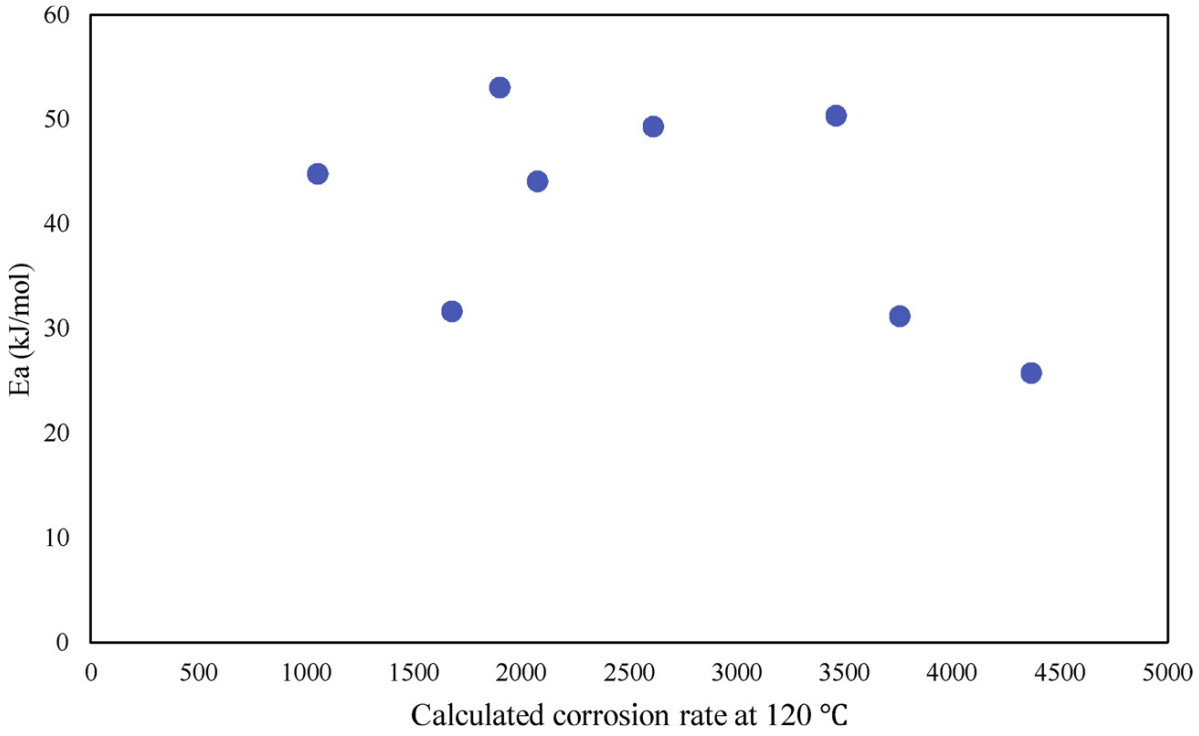

Figure 4-7: Temperature dependence of corrosion rate from 80–150 ℃.

4.3.2 Siderite Protective Films under Flowing Conditions

Besides the effect of PZ degradation, the dynamic fluid environment inside the corrosion loop apparatus is suspected as another reason for the incompleteness of the protective films. Although the wall shear stress caused by the fluid flow has been shown to

be insufficient to cause damage to corrosion product films (Ruzic et al., 2006; Wei et al., 2018), the damage is believed to be related to the local disturbance of the fluid (Ruzic et al., 2006), which in this case could result from the partially boiling solvent in the hot side of the corrosion loop apparatus. It has also been shown that the liquid flow could cause localized spalling of the siderite films, changing the corrosion type from general corrosion to localized corrosion (McCafferty et al.,1972), but such large pits on the siderite film (100–200 μm) have not been observed in the experiments using the corrosion loop. Further investigation on the fluid flow was performed in the pump-around corrosion loop (PACL), which provided the opportunity to control liquid flow rate inside the piping.

The effect of flow velocity on CS corrosion with the presence of siderite product films was evaluated in PACL. Experiment conditions and results are summarized in Table 4-3. Solvent sample from the NCCC 2019 campaign was used in all the experiments. NCCC PZ had an initial loading of 0.31 and was either preloaded to 0.4 loading or blended with fresh PZ solvent prepared in the lab to reduce to the loading to 0.2. The liquid flow rate was controlled by a variable speed gear pump and a needle valve. The measured liquid flow rate was divided by the cross-sectional area inside a 1/2" NPT pipe to get the flow velocity.

Table 4-3: CS corrosion experiments with 5 m PZ in PACL

Line	Solvent	Temperature (°C)	Loading	Velocity (m/s)	Operating hours	CS corrosion (µm/yr)	Siderite film thickness (µm)	Siderite film mass (mg)	Apparent film density (g/cm^3)
1	NCCC	100	0.4	1.3	101	81	10.7	20.1	3.0
2	NCCC	100	0.4	3.2	94	114	10.4	17.6	2.7
3	NCCC/fresh blend	100	0.4	3.2	97	140	10.2	16.8	2.7
4	NCCC/fresh blend	100	0.2	3.2	92	231	10.6	16	2.4
5	NCCC/fresh blend	120	0.2	3.0	104	201	13.1	19.7	2.4
6	NCCC/fresh blend	120	0.2	3.0	46	348	12.6	14.1	1.8

The thickness of siderite films was estimated using an optical surface profilometer. An example of the analysis is given in Figure 4-8. A scratch was made on the siderite film using a dental scraper, which scraped off only the corrosion product scale but not the CS substrate. The scratch showed up as a V-shape valley on the surface profile, and the depth of the valley was considered the thickness of the siderite film. The volume of the film was estimated by multiplying the thickness of the film by the surface area of the coupon. The mass of the siderite film was obtained from coupon weight loss analysis as the difference of coupon weight before and after the product films were removed by acid. An apparent density of the siderite film was then calculated using the estimated mass and volume of the film. The thickness, volume, mass, and density of the siderite films from the experiments in PACL are summarized in Table 4-3.

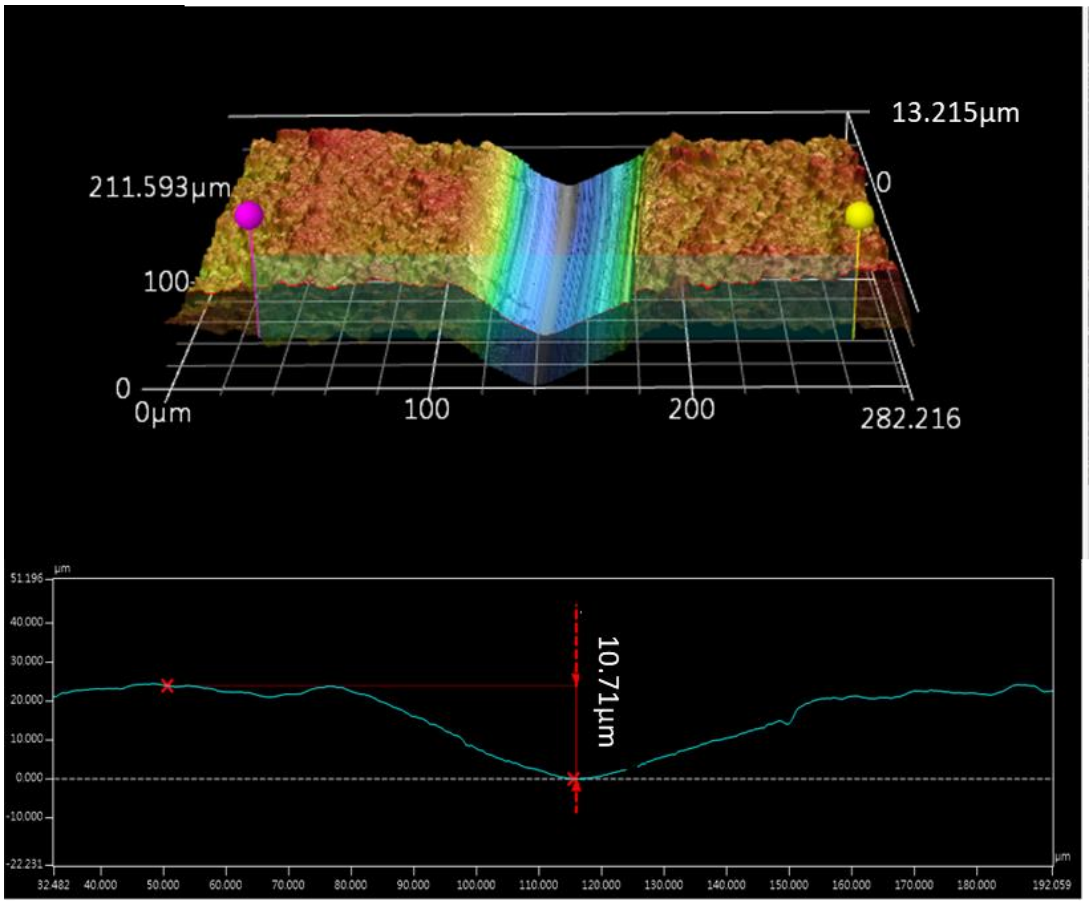

Figure 4-8: Example of film thickness estimated from the surface profile of CS coupon from experiment using 5 m NCCC PZ, 100 °C, 0.4 loading, 1.3 m/s flow velocity.

The siderite film thickness was similar when formed at the same temperature. For example, the films formed at 100 °C, 0.4 loading (Line 1–4 in Table 4-8) had thickness of 10.2–10.7 µm, suggesting flow velocity and loading did not affect the film thickness. The films formed at 120 °C (Line 5–6) also had similar thickness (12.6–13.1 µm) even though one of the coupons had 2X more exposure time than the other. The mass and density of films, on the other hand, showed some correlation with the corrosion rate. The corrosion rate from the experiments at 100 °C increased from 81 to 231 µm/yr as the apparent film

density decreased from 3.0 to 2.4 g/cm^3 (Line 1–4), and the rate from the 120 °C experiments decreased from 201 to 348 as film density went from 2.4 to 1.8 g/cm^3. It suggests that films with higher density provide better protection to the CS substrate.

At 120 °C, 0.2 loading, and 3.0 m/s flow velocity, the CS that was exposed to PZ solvent for 104 hours showed lower corrosion rate (201 μm/yr) than the one exposed for 46 hours (348 μm/yr) corrosion. It suggests CS corrosion was higher at the beginning of experiments, followed by the formation of siderite films which protected CS and lower the corrosion rate. It has been reported in literature that a pre-corrosion process of CS is required for the precipitation of siderite (Farelas et al., 2022). During the active corrosion stage, the ferrite phase of CS dissolves into solution, leaving a porous Fe_3C layer on the surface (Nesic et al., 1993). Fe_3C can increase corrosion rate by acting as cathodic sites, causing high initial corrosion rate. The Fe_3C layer gets thicker as ferrite corrodes and slows down the rate of Fe^{2+} leaving the steel surface. Once it reaches a critical thickness, the Fe_3C film creates sufficient mass transfer resistance and results in local high supersaturation of Fe^{2+} and CO_3^{2-}, which are required for siderite precipitation. This explains the fairly constant thickness of films formed at each temperature.

The Fe_3C may also serve as a scaffold and promote the nucleation of siderite crystals. The crystals grow within the porous Fe_3C layer, fill the gaps, and form a complete film. Until the surface of CS is completely covered, corrosion of CS can continue to occur. There is competition between CS corrosion and siderite precipitation. If the rate of siderite precipitation is higher than the rate of CS corrosion, a dense siderite film will form and act as an effective diffusion barrier between CS surface and corrosive species in bulk liquid. On the contrary, if the rate of siderite precipitation is lower, only a porous film is formed, which provides less protection. Lower CO_2 loading may slow down siderite precipitation

as there is less CO_3^{2-} that can react to form $FeCO_3$. When loading decreased from 0.4 to 0.2 at 100 °C, 3.0 m/s flow velocity (Line 3 & 4), corrosion rate went up from 140 to 231 μm/yr. Although the film thickness did not change significantly, the film density decreased from 2.7 to 2.4 g/cm^3. In addition, higher flow velocity may cause higher mass transfer of Fe^{2+} away from CS surface and break local supersaturation of $FeCO_3$. It may explain the lower film density and higher CS corrosion rate at high velocity.

4.4 CONCLUSIONS

4.4.1 Siderite films can deposit on the surface of CS in CO_2-loaded PZ solution at temperatures >100 °C and protect CS from corrosion. The protection may fail in degraded PZ.

Siderite was the dominant corrosion product on the surface of carbon steel from corrosion loop experiments at 120 °C. Siderite films were observed in 5 m clean PZ and 3–5 m degraded PZ from pilot plants. With clean and slightly degraded PZ solvent, the siderite films protected the CS substrates and resulted in very low corrosion rate (<80 μm/yr) at 120 °C.

The siderite films were not protective when they were formed in severely degraded PZ solvent. A discontinuity of CS corrosion was observed at a critical level of degradation. Without effective protection, CS corroded at significantly higher rates (2400 μm/yr) at 120 °C.

Although some siderite films were not protective due to insufficient thickness and compactness, this work confirmed the frequent formation of siderite films on CS in PZ and expanded the understanding of this protective film to the extremely reducing stripper conditions.

4.4.2 Ethylenediamine (EDA) is one of the major contributors for the loss of film protectiveness or can be the surrogate for the effect of PZ degradation on siderite film protection.

5 m clean PZ with different concentration of EDA showed similar discontinuity of CS corrosion behavior. It suggests EDA itself might be a cause of the failure of protective films. The effect is hypothesized as a result of EDA adsorption on the steel surface. The adsorbed EDA might form a mass transfer barrier between Fe^{2+} from the steel surface and CO_3^{2-} from bilk liquid and impede the formation of siderite films.

4.4.3 Denser siderite films provide better protection to the CS substrate. The apparent density of siderite films decreases with increasing flow velocity and decreasing CO_2 loading.

There is competition between CS corrosion and siderite precipitation. If the rate of siderite precipitation is higher than the rate of CS corrosion, a dense siderite film will form and act as an effective diffusion barrier between CS surface and corrosive species in bulk liquid. On the contrary, if the rate of siderite precipitation is lower, only a porous film is formed, which provides less protection. Lower CO_2 loading results in less CO_3^{2-} available to react with Fe^{2+}. Higher flow velocity may cause higher mass transfer of Fe^{2+} away from CS surface and break local supersaturation of $FeCO_3$. Therefore, siderite precipitation rate may be lower at low loading and high flow velocity, leading to lower film density and protectiveness.

Chapter 5: Conclusions

5.1 CORROSION IN PZAS PILOT PLANTS

Corrosion was evaluated in three pilot plant campaigns using PZAS technology. 316L SS experienced higher corrosion than 304 SS and 2205 duplex SS, and the corrosion rate showed strong dependence on the temperature. 304 and 2205 performed well at all locations and should be good construction materials for PZAS. Degraded PZ exacerbated 316L corrosion, and removal of PZ degradation products using a carbon adsorption bed significantly reduced corrosion.

Carbon steel corrosion showed a weak temperature effect because the corrosion was more dependent on the protective siderite film. The protectiveness of the films was related to fluid velocity.

Ni-based alloys also corroded in PZ, and the rate increased with temperature. Corrosion occurred mostly on the surface open to the bulk solution, and the surface underneath the Teflon washers was less corroded.

5.1.1 316L SS showed severe corrosion by aqueous PZ at high temperatures and reducing conditions, while 304 stainless and 2205 duplex stainless steel remained highly resistant to corrosion at similar conditions.

A high corrosion rate of 316L SS was measured in the high temperature region of PZAS. The highest rate was 1429 μm/yr in the hot lean solvent line (~150 °C), and the corrosion rate showed strong dependence on temperature:

$$Corrosion\ rate\ \left(\frac{\mu m}{yr}\right) = 29 \times \mathrm{EXP}\left(\frac{-9600}{T(K)}\right)$$

304 SS and 2205 duplex SS performed very well at all measurement locations. The rate of corrosion never exceeded 10 μm/yr at both NCCC and SRP pilot plants.

5.1.2 PZ degradation may increase corrosion of 316L SS. Removal of PZ degradation products by a carbon adsorption bed significantly reduced 316L corrosion.

316L SS showed higher corrosion at the NCCC pilot plant in 2019 than in 2018. The chronological increase in corrosion rate could be explained as the effect of PZ degradation. The PZ solvent was more degraded in 2019 as it had been through ~2100 hours of operation in 2018. An activated carbon bed was put into service during the last few weeks of the 2019 NCCC campaign to remove PZ degradation products from the solvent. Significant decrease in 316L corrosion from >1000 μm/yr to negligible values was observed when the carbon bed was in operation, suggesting some corrosive degradation products were removed by the carbon bed.

5.1.3 Carbon steel corrosion can be greatly reduced by a protective siderite ($FeCO_3$) film formed at 110–155 °C. The protection diminished at high flow velocity or in two-phase flow.

Siderite was observed as the primary corrosion product on CS coupons in the high temperature (110–155 °C) regions of PZAS. The protectiveness of the films decreased with increasing flow velocity. At low velocity in the stripper sump, a crystalline and compact siderite film was formed and resulted in very low corrosion of CS (< 11 μm/yr) even though it was one of the hottest (150 °C) points of PZAS. At moderate flow velocity (0.4–0.6 m/s) and the same high temperature, CS corrosion rate was as high as 910 μm/yr. Even higher corrosion rate (9600 μm/yr) was observed in high velocity, two-phase flow between the steam heater and the stripper sump. The loss of protectiveness could be a result of the formation of porous siderite films under high flow velocity.

5.1.4 Ni-based alloys were vulnerable in PZ at high temperature, and the rate of corrosion increased with increasing temperature.

Inconel® 625 and Hastelloy® C276 were evaluated in the Advanced Stripper in the 2019 NCCC campaign, and both showed poor corrosion resistance in PZ at high temperature. Therefore, the Ni-based alloys may not be good candidate materials for PZAS. Their corrosion rates showed dependence on temperature:

$$Corrosion\ rate\ (\frac{\mu m}{yr}) = 33 \times EXP\left(-\frac{11400}{T(K)}\right)$$

5.1.5 Corrosion of CS by water during water testing can be significant at high temperature, and SS corrosion by hot water is negligible.

CS corrosion during water testing was evaluated in the SRP 2021 campaign, and the highest rate was 275 μm/yr in the warm bypass. Although the CS corrosion rates measured during the water testing period all seemed acceptable (<300 μm/yr), long operating hours with water should be avoided if any part of the system is built with CS. 316L and 304L SS performed very well in hot water up to 151 °C

5.1.6 Several mitigation methods to reduce PZ oxidation were tested in the SRP pilot plant. Most of them had minor effects on corrosion compared to temperature and flow velocity.

NO_2 injection, N_2 sparging in the absorber sump, increased warm bypass residence time, and removal of PZ degradation products by a carbon bed were evaluated in the SRP 2021 campaign. Most of these operations seemed to slightly alter the oxidation state of the PZ solvent but did not show a significant effect on CS or SS corrosion. Longer period for each operation is recommended for the future pilot testing.

5.2 CORROSION IN PZAS ABSORBER AND WATER WASH

Corrosion of carbon steel (C1010) and stainless steels (304, 316L, 430) was measured at absorber and water wash conditions on the bench-scale. Corrosion rate decreases with increasing piperazine (PZ). With more than 0.003 m PZ in solution, carbon steel has acceptable corrosion performance. Corrosion of carbon steel increases with increasing partial pressure of CO_2, suggesting loading is another dominant parameter for carbon steel corrosion. The effect is more significant for dilute PZ; therefore, untreated flue gas with high CO_2 content should be avoided in the water wash. Temperature has a less significant effect than PZ concentration and loading. Carbon steel corrosion increases with increasing flow velocity at both absorber and water wash conditions.

5.2.1 Carbon steel is a promising material candidate for 5 m PZ at absorber conditions and can also be used for a water wash with caution. Stainless steels (304, 316L, and 430) have excellent corrosion resistance at absorber and water wash conditions.

C1010 CS performs well (<300 μm/yr) in 5 m PZ under normal operating conditions in a PZAS absorber (40–75 °C, 0.04–12% CO_2 in gas) and can be a good candidate construction material for the absorber. The low amine concentration and high level of dissolved CO_2 in the water wash can cause CS corrosion by carbonic acid. Some restrictions of operating conditions are required for a water wash built with CS. Stainless steels, including 304, 316L, and 430, all show great corrosion performance (<60 μm/yr), and are ideal materials for the PZAS absorber and water wash.

5.2.2 Carbon steel corrosion decreases as more PZ is present in solution. The decrease of solution corrosivity can be explained by the increase in solution pH.

C1010 carbon steel corroded significantly (~750 μm/yr) when the solution has lower than 0.003 m PZ with an inlet gas of 1.5% CO_2 in air at 60 °C. Corrosion decreases as the PZ in the solution increases. The correlation between C1010 corrosion rate (CR, μm/yr) and PZ molality (C_{PZ}) can be expressed as:

$$CR = 2.4 \times C_{PZ}^{-0.68}$$

As more PZ is added, the solution becomes less acidic, and fewer protons were available for the cathodic corrosion reaction to occur, and results in lower corrosion rates. pH measurement of the water wash solution can be an easy tool for monitoring CS corrosion in the water wash during operation.

5.2.3 0.01 m PZ can be sufficient to protect carbon steel at normal operating conditions for a PZAS water wash, but untreated flue gas with high CO_2 content might cause corrosion if entering the WW.

When the PZ concentration increases to 0.01 m, the performance of C1010 is acceptable (<300 μm/yr). Therefore, maintaining at least 0.01 m PZ in the water wash solution can allow for carbon steel construction of a PZAS water wash under normal operating conditions.

C1010 corrosion is a strong function of loading at absorber and water wash conditions. The dependence of corrosion rate on loading (ldg) and temperature (T, K) can be expressed as:

$$\ln(CR) = 8.5(ldg) - 3337\left(\frac{1}{T} - \frac{1}{333}\right) + 0.9$$

5.2.4 Operating temperature in the water wash is varied to maintain water balance of the PZAS process. Data suggest 40 °C is the optimal operating temperature for the water wash.

Higher operating temperature in the water wash may cause higher corrosion by increasing the reaction kinetics. High temperature also results in lower equilibrium CO_2 content in solution and therefore may reduce corrosion. The experiment results suggest that 40 °C is a better operating temperature for the PZAS absorber and water wash than 60 or 75 °C.

Temperature affects PZ concentration in the water wash. When the absorber is operated at higher temperature, more volatile PZ leaves from the absorber top and enters the water wash column. Meanwhile, higher water wash temperature leads to more water vapor leaving the water wash column with the CO_2-depleted flue gas. Therefore, PZ concentration in the water wash is higher at higher temperature, which is expected to reduce CS corrosion.

5.2.5 Flow-enhanced corrosion of CS was observed in 0.01 m and 5 m PZ at high velocity.

Within the low velocity range (0.6–1.6 m/s), the corrosion rate of carbon steel in 0.01 m PZ was almost constant. In the high velocity region (1.6–3.0 m/s), corrosion of CS increased more rapidly. The corrosion rates measured in 5 m PZ showed a similar trend with flow velocity. Extra turbulence inside pipe elbows increases corrosion.

5.2.6 Stainless steels (304L, 316L, and 430) have excellent performance at absorber and water wash conditions.

Three stainless steels (304L. 316L. and 430) were evaluated at representative absorber and water wash conditions. All three materials exhibited very low corrosion rates (~1 μm/yr) with occasional higher but still acceptable corrosion (~50 μm/yr).

5.3 CARBON STEEL PROTECTED BY SIDERITE IN THE ADVANCED STRIPPER

This section summarizes the study of the siderite ($FeCO_3$) protective film on CS corrosion at representative conditions in the Advanced Stripper. Corrosion of carbon steel was evaluated in two bench-scale apparatuses, the corrosion loop and the pump-around corrosion loop (PACL), using electrical resistance (ER) measurements and corrosion coupons. Both apparatuses provided an environment with high temperature and pressure (120 °C, up to 150 psi), which was rarely seen in corrosion literature using electrochemical corrosion measurements, and PACL enabled the study of the effect of liquid flow on siderite films. The results focus on the effects of PZ degradation and flow velocity on the protection by siderite films.

5.3.1 Siderite films can deposit on the surface of CS in CO_2-loaded PZ solution at temperatures >100 °C and protect CS from corrosion. The protection may fail in degraded PZ.

Siderite was the dominant corrosion product on the surface of carbon steel from corrosion loop experiments at 120 °C. Siderite films were observed in 5 m clean PZ and 3–5 m degraded PZ from pilot plants. With clean and slightly degraded PZ solvent, the siderite films protected the CS substrates and resulted in very low corrosion rate (<80 μm/yr) at 120 °C.

The siderite films were not protective when they were formed in severely degraded PZ solvent. A discontinuity of CS corrosion was observed at a critical level of degradation. Without effective protection, CS corroded at significantly higher rates (2400 μm/yr) at 120 °C.

Although some siderite films were not protective due to insufficient thickness and compactness, this work confirmed the frequent formation of siderite films on CS in PZ and

expanded the understanding of this protective film to the extremely reducing stripper conditions.

5.3.2 Ethylenediamine (EDA) is one of the major contributors for the loss of film protectiveness or can be the surrogate for the effect of PZ degradation on siderite film protection.

5 m clean PZ with varying EDA showed similar discontinuity of CS corrosion behavior. Therefore EDA itself may be a cause of the failure of protective films. The effect is hypothesized as a result of EDA adsorption on the steel surface. The adsorbed EDA might form a mass transfer barrier between Fe^{2+} from the steel surface and CO_3^{2-} from bulk liquid and impede the formation of siderite films.

5.3.3 Denser siderite films provide better protection to the CS substrate. The apparent density of siderite films decreases with increasing flow velocity and decreasing CO_2 loading.

There is competition between CS corrosion and siderite precipitation. If the rate of siderite precipitation is higher than the rate of CS corrosion, a dense siderite film will form and act as an effective diffusion barrier between CS surface and corrosive species in bulk liquid. On the contrary, if the rate of siderite precipitation is lower, only a porous film is formed, which provides less protection. Lower CO_2 loading results in less CO_3^{2-} available to react with Fe^{2+}. Higher flow velocity may cause higher mass transfer of Fe^{2+} away from CS surface and break local supersaturation of $FeCO_3$. Therefore, siderite precipitation rate may be lower at low loading and high flow velocity, leading to lower film density and protectiveness.

Chapter 6: Recommendations

6.1 Material Recommendations for PZAS

A simplified flow diagram of PZAS showing material recommendations for each unit operation is given in Figure 6-1. Recommendations are made based on an industrially accepted corrosion standard (300 μm/yr) for process equipment and piping. 304 stainless steel had great performance (<10 μm/yr) at all tested locations at pilot plants and in all bench-scale experiments and can be acceptable for the entire PZAS process. To reduce capital costs, carbon steel is recommended wherever appropriate (<300 μm/yr).

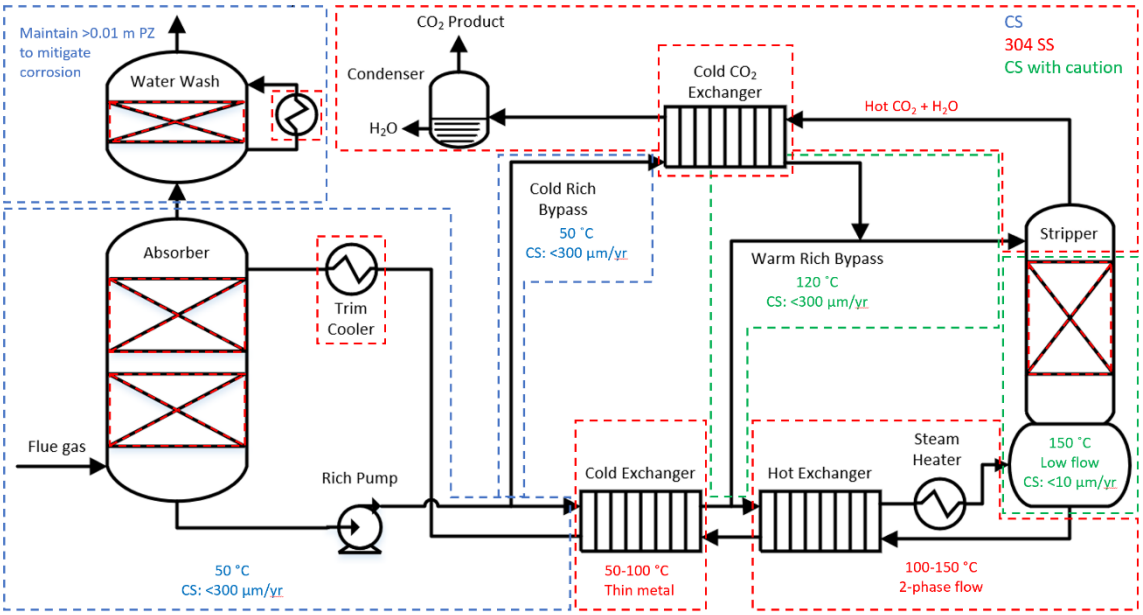

Figure 6-1: Material recommendations for PZAS; blue: CS construction recommended; green: CS construction with caution; red: SS construction required.

In the absorber area, carbon steel (C1010) generally performs well. CS corrosion rate was very low at absorber mid bed (<1 μm/yr). Corrosion was higher in the absorber sump at pilot plants (up to 298 μm/yr), possibly due to locally high CO_2 content near the

flue gas inlet, but still within the acceptable range. Overall, CS is recommended for the wall of absorber column. Problems may occur at locations that are not wetted with PZ—the absorber top/outlet gas piping from the absorber and the absorber walls below chimney trays. At these locations, the column and piping walls may see condensed water with dissolved CO_2 and experience carbonic acid corrosion. Linings made of 304 SS, which typically has great resistance to carbonic acid corrosion, should be considered at the absorber overhead to protect the CS wall from corrosion problems. Structured packing and some parts of other column internals (distributors, chimney trays, etc.) are very thin (< 1 mm) and can only tolerate much lower corrosion rates. Therefore, 304 SS is recommended for these parts with thin metal structures to ensure sufficient lifetime for the equipment.

CS is likely acceptable in low temperature piping (50 °C) between the absorber and the cold exchanger. In the cold lean piping, C1010 corrosion was moderate (200 μm/yr) at pilot plants. Performance in the cold rich bypass was higher but still acceptable (290 μm/yr). The moderate performance of C1010 here suggests that it may be acceptable for most of the piping and some equipment (pump, carbon bed vessel, etc.) in this area. CS corrosion rates may still be too high for the heat exchanger tubes and plates with small thickness. Therefore, 304 SS is recommended for the trim cooler and the intercooler.

Corrosion measurement at the bench scale suggests CS corrosion is significantly lower when there is sufficient PZ in the water wash solution. CS is recommended for the water wash column wall and circulation piping if PZ concentration is maintained at least 0.01 m. The exchanger tubes of the water wash cooler are in contact with the process liquid, and 304 SS would be more appropriate due to the thin tube walls. On the other hand, the shell side of the cooler only contacts cooling water or air, and CS may be adequate for the exchanger shell.

CS is likely appropriate for some equipment in the regions at elevated temperature. C1010 performance was good (<150 μm/yr) in the warm rich bypass and in the stripper sump (<10 μm/yr). The good performance of C1010 at elevated temperature is due to the presence of protective siderite films. However, the long-term performance of these protective films is not clear, especially when PZ is being degraded over time. Therefore, although CS is proposed for the warm rich bypass and the stripper sump, cautions need to be taken and long-term testing of CS at these locations should be done before making final decisions. 316L SS was sometimes attacked (490 μm/yr) in the stripper sump due to high temperature and reducing conditions. The occasional vulnerability of SS suggests that CS may be a preferable material of construction for the stripper sump.

All three major exchangers (cold exchanger, hot exchanger, and cold CO_2 exchanger) are plate-and frame exchangers, and the plates can be as thin as only 0.5 mm. They require very low corrosion and should be built with 304 SS or other materials (2205 duplex SS) with excellent corrosion resistance.

In high temperature (150 °C) piping, siderite films are not adequate to protect carbon steel, resulting in very poor performance of CS in the hot lean stream (700 μm/yr) and the hot rich stream (9600 μm/yr). 304 SS is specified for the hot piping.

6.2 RECOMMENDATIONS FOR FUTURE CORROSION STUDY FOR CO_2 CAPTURE

6.2.1 Strengthen link between stainless attack and reducing conditions with better measurement of solution potential.

316L SS corrosion was observed in the stripper area at pilot plants and occasionally in the bench-scale corrosion loop apparatus. The extremely reducing condition was assumed to be the cause of SS de-passivation, but no good measurement of solution

potential has been made to support this hypothesis. For future study, measurement of solution oxidation-reduction potential (ORP) should be made with measurement of SS corrosion. Injection of oxidizing (e.g. H_2O_2) or reducing agents (e.g. SO_3^-) to PZ solvent allows an artificial change of solution potential and can help with the study.

6.2.2 Evaluate the effect of PZ degradation products other than ethylenediamine (EDA) in CS corrosion.

Although EDA has been identified as a contributor to the loss of carbon steel protection by siderite, EDA is not the only species that is responsible. Also, CS showed higher corrosion during the NO_2 injection period during the SRP 2021 campaign, indicating some products of NO_2-induced degradation (like nitrosamine) may affect CS corrosion. As more reliable analytical methods are developed in labs, correlation between CS corrosion and levels of degradation products can be established to better understand the effect of PZ degradation on the properties of siderite films.

6.2.3 Test durability of siderite protective films in long-term pilot testing.

Bench-scale results suggest siderite protective films fail when formed in severely degraded PZ solvent. This effect of PZ degradation has not been observed in previous pilot testing due to insufficient level of accumulated corrosion products over the test period. CS should be evaluated for extended period in warm bypass and stripper sump, where CS was found well protected by siderite in previous campaigns. Any sign of decrease of film protectiveness over time due to PZ degradation should be monitored.

6.2.4 Extend operating hours for PZ oxidation mitigations at future pilot testing to evaluate their effects on corrosion.

Several operations related to the study of PZ oxidation were performed during the SRP 2021 campaign, including the introduction of NO_2 in flue gas, increased residence time in the warm rich bypass, N_2 sparging in the absorber sump, and removal of degradation products by carbon adsorption. However, the effects of these operations on corrosion were not clear due to the short operating period during the campaign. Longer period for each operation is recommended for future pilot testing for more obvious effects to be observed.

6.2.5 Suggested corrosion test plans for future NCCC campaign

A pilot plant campaign will take place at the National Carbon Capture Center pilot plant. Some recommendations for corrosion testing are provided for this pilot testing activity. Figure 6-2 shows a simplified flow diagram of NCCC pilot plant, marking the locations for corrosion coupon insertion. Each circle on the diagram represents one disc coupon holder which can hold up to four disc coupons (Metal Samples CO220 type) at a time. Each square represents a trip coupon holder which can hold up to two strip coupons (Metal Samples CO118 type). There are 16 existing coupon locations that have been used in previous campaigns, and 7 have been added for future campaign. All the new locations are installed at elbows where higher turbulence is believed to cause more serious corrosion problems. A detailed procedure for installing the coupon holders has been documented by Fischer (2018).

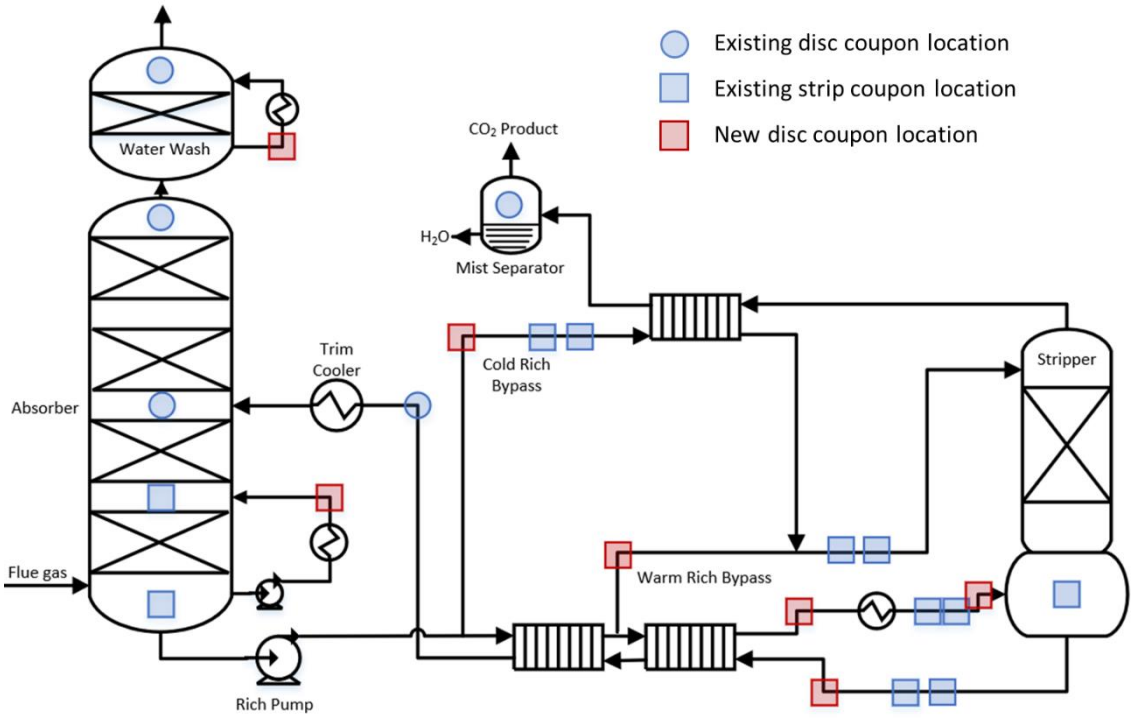

Figure 6-2: Simplified flow diagram of NCCC pilot plant with corrosion coupon locations

Coupons will be batched to increase the number of coupons that can be evaluated. Coupons should be changed out when major change in operating condition occurs. Each batch should stay in the system for at least 5–7 days to get representative corrosion results—preferably last for an extended period of time (4–6 weeks) at a relatively constant operating condition. In addition to the batched (short-term) coupons, at least one long-term coupon for each location that stays through the entire campaign should be considered because it provides valuable long-term corrosion results that are very difficult to replicate at the bench-scale.

A list of coupon materials recommended for each location in the absorber and water wash area at NCCC is given in Table 6-1. CS showed acceptable corrosion performance in the low temperature region of PZAS, including the absorber, water wash, and cold piping,

in previous bench- and pilot-scale experiments. The main focus of corrosion evaluation in the next pilot plant campaign will be to reassure that CS is acceptable, and therefore, only CS will be evaluated here. There are two coupon slots for each location at a time, but up to two more coupons can be added to each disc coupon locations if more coupons need to be evaluated. There is one long-term (LT) CS planned for each location that will stay through the entire campaign. Another slot will be for the batched short-term (ST) coupons which will be changed out several times during the campaign.

Table 6-1: Proposed test materials in the absorber and water wash at NCCC

Location	Coupon type	Slot 1	Slot 2
Water wash column	Disc	LT CS	ST CS
Water wash piping	Strip	LT CS	ST CS
Absorber top	Disc	LT CS	ST CS
Bed 2-3	Disc	LT CS	ST CS
Bed 1-2	Strip	LT CS	ST CS
Absorber sump	Strip	LT CS	ST CS
Cold lean	Disc	LT CS	ST CS
Intercooler	Strip	LT CS	ST CS

Table 6-2 summarizes the recommendation for materials to be evaluated in the Advanced Stripper for the next NCCC campaign. Most of the corrosion test locations, except stripper sump and the hot rich stream between hot exchanger and steam heater, have three ports for corrosion coupon insertion. One of the three ports at each location is at a pipe elbow, and the coupon slots at these elbows are referred to as Elbow 1 & 2. The other two ports on in straight pipe sections, and the coupon slots are referred to as Straight 1 & 2 and Straight 3 & 4. In the cold rich bypass, similar to other low temperature locations,

CS will be tested. One LT and one ST CS coupons are planned for the elbow port and one of the straight pipe ports. The second straight pipe port can be used if other materials or more coupons need to be tested. CS will also be tested in the warm rich bypass using the same arrangement. The second straight pipe port here will be used to test 304L and 316L SS. There is only one elbow port in the stripper sump and the hot rich line between the hot exchanger and the steam heater. ST 304L and 316L SS will be tested side by side at these two locations so that direct comparison between the corrosion performance of these two materials at 150 °C can be drawn. In the hot lean stream and the hot rich stream between the steam heater and stripper sump, in addition to ST 304L and 316L at the elbow port, LT SS will be tested at one straight pipe port. The second straight pipe port can be used to test other materials, such as Ni alloys, duplex SS or others.

Table 6-2: Proposed test materials in the Advanced Stripper at NCCC

Location	Elbow 1	Elbow 2	Straight 1	Straight 2	Straight 3	Straight 4
Cold rich bypass	LT CS	ST CS	LT CS	ST CS		
Warm rich bypass	LT CS	ST CS	LT CS	ST CS	LT 304L	LT 316L
Hot rich HX-Stm H	ST 304 L	ST 316L	-	-	-	-
Hot rich Stm H-stripper	ST 304 L	ST 316L	LT 304L	LT 316L	Ni alloys, duplex SS, or other	
Stripper sump	ST CS	ST 304 L	-	-	-	-
Hot lean	ST 304 L	ST 316L	LT 304L	LT 316L	Ni alloys, duplex SS, or other	

Appendix

A. Standard Operating Procedure for the Pump-Around Corrosion Loop

By Ching-Ting Liu

Sep 9, 2021

Process Description

The new corrosion loop mainly consists of a gear pump and a 1.5”/0.5” pipe loop. There are four ports for electrical resistance (ER), linear polarization resistance (LPR), and oxidation reduction potential (ORP) measurements on the vertical section downstream of the pump and 9 ports for cylindrical coupons at the elbows on the upper right corner. Immediately downstream of the ER/LPR probe location, there is an oxidizer injection port to enable the change of solvent oxidation potential during an experiment. The section of 1.5” pipe downstream of the pump discharge is wrapped with a heating cable, which is controlled in the DeltaV control system at SRP based on the measurement of a resistance temperature detector (RTD). An armored level gauge and a level switch is installed on the upper left of the loop to monitor the solvent inventory. An N_2 line with a manual gas flow regulator, a 1-way check valve, and a back-pressure regulator will be used to control system pressure. A liquid sampling loop using Swagelok quick-connect fittings and flexible stainless steel tubing will be installed across the pump.

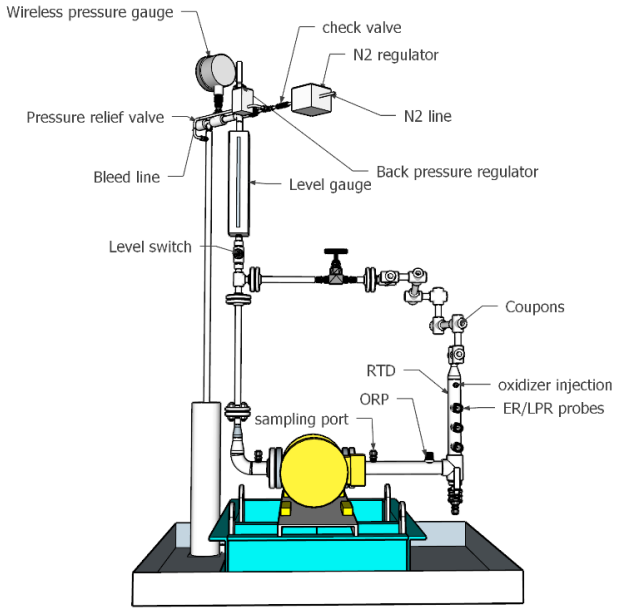

Figure A-1: Schematic of the new corrosion loop

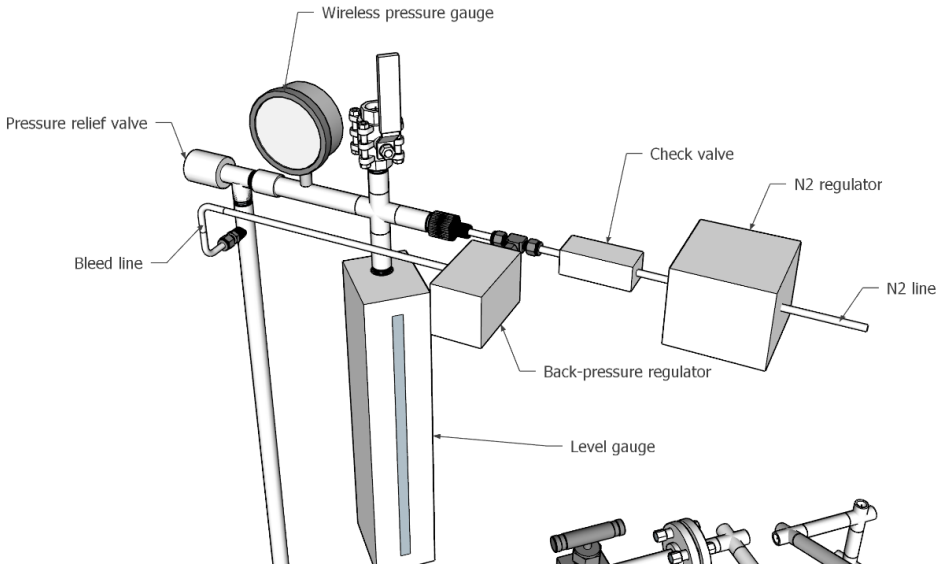

Figure A-2: Pressure control system on the new corrosion loop

List of chemicals

Piperazine, anhydrous
Water
Degraded PZ solution from pilot plants
Carbon dioxide, from pressurized cylinder
Nitrogen, from pressurized cylinder

Process & Analytical Measurements

Measurement	**Type**	**Equipment**
Temperature	Process	Rosemount RTD (TT-CL1)
Pressure	Process	Rosemount wireless pressure gauge (PT-CL1)
Electrical resistance (ER)	Corrosion	Metal Samples retractable ER probes (AI-CL1~2)
Linear polarization resistance (LPR)	Corrosion	Metal Samples retractable LPR probe (AI-CL3)
Oxidation-reduction potential (ORP)	Corrosion	Rosemount ORP probe (AI-CL4)

PFD/P&ID

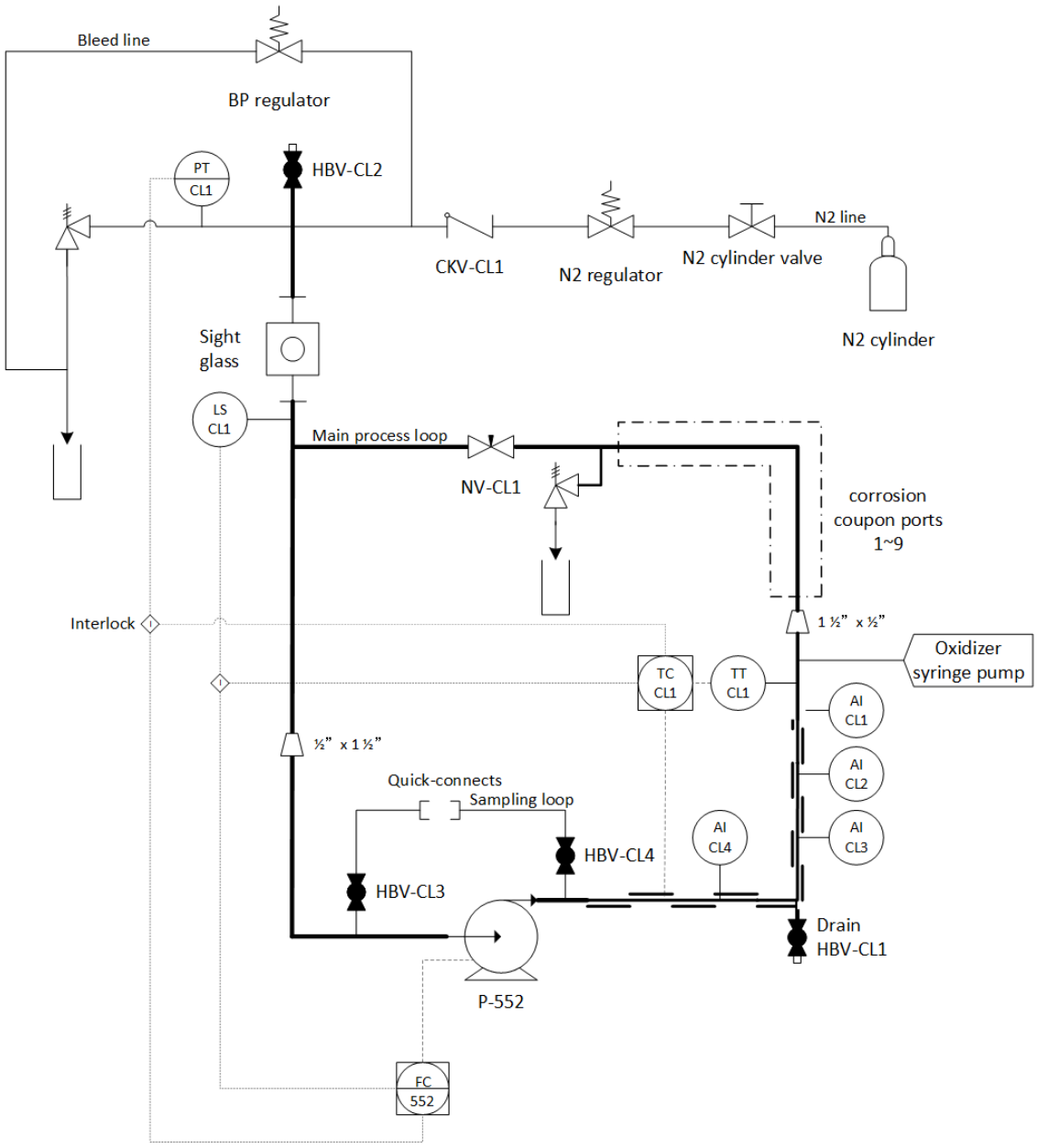

Figure A-3: New corrosion loop piping and instrumentation diagram

Pre-Start Up

1. Water testing
   1.1. Shut and plug the bottom drain valve (HBV-CL1), cap four corrosion probe ports and nine coupon ports.
   1.2. Load DI water into the corrosion loop from the top valve (HBV-CL2), and leave the valve open. Open the needle valve fully.
   1.3. Start P-552. Circulate liquid until no more air bubbles come out. (If level drops below level switch (LS-CL1), P-552 would shut down. Put in more liquid and restart the pump.) Stop the pump when all the entrained air is removed. Close and cap the top valve (HBV-CL2).
   1.4. Open nitrogen cylinder valve and set pressure to 130 psig. Set back-pressure regulator on the bleed line to 130 psig. Set pressure relief valve to 150 psig. Check if liquid level is still visible in the sight glass.
   1.5. Start P-552.
   1.6. Start heating cable and set temperature to 150 °C (302 °F)
   1.7. Adjust VFD of pump P-552 and the position of needle valve (NV-CL1) to test their effect on temperature control.
   1.8. Shut down by turning off heating cable and P-552. Shut the nitrogen cylinder valve and regulator. Wait for the system to cool to approximately 40 °C. Release residual pressure by slowly opening the top ball valve.
   1.9. Drain water via the bottom drain valve (HBV-CL1).

Start-Up

1. Load the corrosion loop with piperazine (PZ)
   1.1 Insert ER/LPR probes (AI-CL1~3), an ORP probe (AI-CL4) and corrosion coupons along with coupon holders to the designated locations. Cap other unused ports. Make sure the bottom drain ball valve (HBV-CL1) is closed and plugged.
   1.2 Connect the sample cylinder to the sampling loop, and open both valves on the loop (HBV-CL3 & HBV-CL4). Open the top ball valve (HBV-CL2), put in PZ solution through the valve using a funnel. Leave the top valve open.
   1.3 Start P-552. Circulate liquid until no more air bubbles come out. (If level drops below level switch (LS-CL1), P-552 will shut down. Put in more liquid and restart the pump.) Stop the pump when all the entrained air is removed. Close and cap the top valve (HBV-CL2). Close HBV-CL3 & HBV-CL4 and disconnect sample cylinder.
2. Pressurize the loop
   1.4 Open the valve on the nitrogen cylinder, turn the regulator knob to adjust outlet pressure. The pressure should be 15% higher than the operating pressure of the

system and not exceed 150 psig (maximum working pressure of the wireless pressure gauge). Shut nitrogen cylinder valve and regulator.

1.5 Monitor the pressure and liquid level in the level gauge for 15 minutes. Search for any solvent leaks or gas leaks using soapy water at any joints. If leakage is observed, slowly open the top ball valve (HBV-CL2) to depressurize, re-tighten the leaking connections, close the ball valve, and repeat steps 2.1 and 2.2.

1.6 Open nitrogen cylinder valve and adjust the nitrogen regulator and the back-pressure regulator on the bleed line to get the desired operating pressure.

2. Start solvent circulation and heating.

2.1 Adjust the pump (P-552) flow rate and the throttling valve position to reach target flow rate.

2.2 Turn on the heating element and perform hourly check until the temperature reaches set point.

Steady-State Operation

1. Keep monitoring the temperature (TT-CL1), pressure (PT-CL1), and liquid level (sight glass).
2. Collect data from the on-line measurements: ER, LPR, and ORP.
3. Collect liquid samples. The sampling line ties into the pump discharge line where samples are drawn and returns solvent to the suction side of the pump.

3.1. Fill the sample cylinder with PZ in the lab to make up the volume to be taken out. Connect the sample cylinder to the stainless steel braided hose downstream of the isolation valves by applying pressure to the quick connect joints.

3.2. Open the high pressure isolation valve (HBV-CL4) downstream of the pump discharge. Then open the low pressure isolation valve (HBV-CL3) upstream of the pump suction.

3.3. Let sample run through the cylinder for approximately 20 seconds to clean the sample cylinder out and rinse the cylinder with fresh sample.

3.4. Close the low pressure isolation valve (HBV-CL3) upstream of the pump suction. Then close the high pressure valve (HBV-CL4) downstream of the pump discharge.

3.5. Disconnect the sample cylinder from the stainless steel braided hose. Operators should use towels and face shields to minimize PZ spray and exposure when taking samples.

3.6. Once all samples have been collected, place the stainless steel sample cylinders in a freezer for approximately 30 minutes. Sample cooling helps prevent the flashing of any hot PZ solution.

3.7. Use a syringe to remove liquid from the sample cylinders and place the sample in sealed glass vials for analysis.

4. Inject oxidizer (30% aqueous hydrogen peroxide) to control solvent oxidation potential
    4.1. Inject oxidizer through the 1/8" Swagelok port above the corrosion probe locations using a syringe pump or a metering pump. (Calculations and experiments are required to determine the injection rate.)
    4.2. Closely monitor the system temperature and pressure since the oxidation of the solvent can cause a rapid rise in temperature and thus over-pressurize the loop. If the temperature goes beyond the set point, remove part of the piping insulation to help cool the loop.

Shutdown Procedure

1. Turn off the pump and the heater. Shut the cylinder valve and nitrogen regulator. Wait for the loop to cool.
2. After the solvent cools to approximately 40 ˚C, slowly open the top ball valve (HBV-CL2) to release any residual pressure.
3. Drain the solvent from the bottom drain valve (HBV-CL1) and store it in sealed jars.
4. Rinse the loop with water
    4.1. Close the drain valve (HBV-CL1) and put in water at the top ball valve (HBV-CL2).
    4.2. Start P-552 to circulate the water for 5 minutes.
    4.3. Turn off P-552 and drain the water.
    4.4. Repeat 4.1 to 4.3 until the drained water is clear.
5. Pull out the corrosion probes and coupons. Rinse them with DI water and acetone and let them dry. Wrap the coupons with the original packaging and store them in the glass desiccator for future analysis.

Emergency Shutdown Procedure

All power to the system, including the pump, heating cable, and LPR/ORP transmitters is from the electrical enclosure box right next to the New Corrosion Loop rig. In the event of emergency, shut off the breaker (Sec. 3 of 3) in the control room to cut the power. A power switch on the outside of the electrical enclosure box can serve as a secondary power shutdown mechanism.

References

Billingham MA, Lee CH, Smith L, Haines M, James SR, Goh BKW, Dvorak K, Robinson L, Davis CJ, Peralta-Solorio D. "Corrosion and Materials Selection Issues in Carbon Capture Plants." *Energy Proc.* 2011;4;2020–2027. doi.org/10.1016/j.egypro.2011.02.083.

Bonis MR, Ballaguet JP, Rigaill C. "A Critical Look at Amines: a Practical Review of Corrosion Experience Over Four Decades." Presented at the 83rd Annual GPA Convention, New-Orleans, LO, 14-17 March 2004.

Bottoms RR. Process for Separating Acidic Gases. In: Google Patents. 1930.

Campbell KLS, Zhao Y. Hall JJ, Williams DR. "The Effect of CO_2-Loaded Amine Solvents on the Corrosion of a Carbon Steel Stripper." *Int. J. Greenh. Gas Control.* 2016;47;376–385. doi.org/10.1016/j.ijggc.2016.02.011.

Chang H, Shih C-M. "Simulation and Optimization for Power Plant Flue Gas CO_2 Absorption-Stripping Systems." *Sep. Sci. Technol.* 2005;40;877–909.

Chen E, Zhang Y, Lin Y, Nielsen P, Rochelle, GT. "Review of Recent Pilot Plant Activities with Concentrated Piperazine." *Energy Proc.* 2017;114;1110-1127. doi:10.1016/j.egypro.2017.03.1266

Chokshi K, Sun W, Nešić S. "Iron Carbonate Scale Growth and the Effect of Inhibition in CO_2 Corrosion of Mild Steel." *CORROSION*. 2005.

Cousins A, Cottrell A, Lawson A, Huang S, Feron PHM. "Model Verification and Evaluation of the Rich-Split Process Modification at an Australian-Based Post Combustion CO_2 Capture Pilot Plant." *Greenhouse Gases: Science and Technology.* 2012;2(5);329–345. doi:10.1002/ghg.1295

Cousins A, Ilyushechkin A, Pearson P, Cottrell A, Huang S, Feron PHM. "Corrosion Coupon Evaluation under Pilot-Scale CO_2 Capture Conditions at an Australian Coal-Fired Power Station." *Greenh. Gases Sci. Technol.* 2013;3;3;169–184. doi.org/10.1002/ghg.1341.

Cousins A, Nielsen PT, Huang S, Rowland R, Edwards B, Cottrell A, Feron PHM. "Pilot-Scale Evaluation of Concentrated Piperazine for CO_2 Capture at an Australian Coal-Fired Power Station: Nitrosamine Measurements." *Int. J. of Greenh. Gas Control.* 2015;37; 256-263. doi:10.1016/j.ijggc.2015.03.007

Danaee I, Niknejad Khomami M. “Effect of Ethylenediamine on Corrosion of AISI 4130 Steel Alloy in 30% Ethylene Glycol Solution Under Static and Hydrodynamic Condition.” *Mat-wiss uWerkstofftech.* 2012;43;942–949.

De Waard C, Milliams DE. "Carbonic Acid Corrosion of Steel." *Corrosion.* 1975;31(5);177–182.

Dugstad A. “Mechanism of Protective Film Formation during CO_2 Corrosion of Carbon Steel.” Presented at the CORROSION 98. NACE International. 1998.

Dunlop AK, Hassel HL, Rhodes PR. “Fundamental Considerations in Sweet Gas Well Corrosion.” *Pap. Corros.* 1983;24.

Dupart MS, Bacon TR, Edwards DJ. “Understanding and Preventing Corrosion in Alkanolamine Gas Treating Plants.” Proceedings of the 41st Laurance Reid Gas Conditioning Conference. March 4–6, 1991. Norman, Oklahoma.

Dupart MS, Bacon TR, Edwards DJ. “Understanding Corrosion in Alkanolamine Gas Treating Plants: 1. Proper Mechanism Diagnosis Optimizes Amine Operations.” *Hydrocarb Process.* 1993a;72;75–79.

Dupart MS, Bacon TR, Edwards DJ. “Understanding Corrosion in Alkanolamine Gas Treating Plants: 2. Case Histories Show Actual Plant Problems and Their Solutions.” *Hydrocarb Process.* 1993b;72;89–94.

EPA. *Inventory of US Greenhouse Gas Emissions and Sinks: 1990–2016*. 2018

Fakeeha AH, Abdelaleem FA. “The Interaction between Corrosion Processes and Mass Transfer at Rough Surfaces.” *J. King Saud Univ. Eng. Sci.* 1996;8(1);51–69.

Fine NA. “Nitrosamine Management in Aqueous Amines for Post-Combustion Carbon Capture.” Ph. D. Dissertation, The University of Texas at Austin, TX, 2015

Fischer KB, Daga A, Hatchell D, Rochelle GT. “MEA and Piperazine Corrosion of Carbon Steel and Stainless Steel.” *Energy Proc.* 2017;114;1751–1764. doi.org/10.1016/j.egypro.2017.03.1303.

Fischer KB. “Corrosion of Stainless and Carbon Steel in Aqueous Amine for CO_2 Capture.” Ph. D. Dissertation, The University of Texas at Austin, Austin, TX, 2019.

Flø NE, Faramarzi L, Iversen F, Kleppea ER, Graverc B, Bryntesend HN, Johnsen K. “Assessment of Material Selection for the CO_2 Absorption Process with Aqueous MEA Solution Based on Results from Corrosion Monitoring at Technology Centre Mongstad.” *Int J Greenh Gas Control.* 2019;84;91–110. doi.org/10.1016/j.ijggc.2019.02.004

Fontana MG. *Corrosion Engineering* 3rd Edition. McGraw-Hill. 1986.

Frailie PT. "Modeling of Carbon Dioxide Absorption/Stripping by Aqueous Methyldiethanolamine/Piperazine." Ph.D. Dissertation, The University of Texas at Austin, TX, 2014.

Freeman SA. "Thermal Degradation and Oxidation of Aqueous Piperazine for Carbon Dioxide Capture." Ph.D. Dissertation, The University of Texas at Austin, TX, 2011.

Fytianos G, Grimstvedt A, Knuutila H, Svendsen HF. "Effect of MEA's Degradation Products on Corrosion at CO_2 Capture Plants." *Energy Proc.* 2014;63;1869–1875.

Fytianos G, Ucar S, Grimstvedt A, Hyldbakk A, Svendsen HF, Knuutila HK. "Corrosion and Degradation in MEA Based Post-Combustion CO_2 Capture." *Int. J. Greenh. Gas Control* 2016;46;48–56.

Gao K, Yu F, Pang X, Zhang G, Qiao L, Chu W, Lu M. "Mechanical Properties of CO_2 Corrosion Product Scales and Their Relationship to Corrosion Rates." *Corros. Sci.* 2008;2796–2803.

Gao J, Wang S, Zhou S, Zhao B, & Chen C. "Corrosion and Degradation Performance of Novel Absorbent for CO_2 Capture in Pilot-scale." *Energy Proc.* 2011;4;1534–1541. doi:10.1016/j.egypro.2011.02.022

Gao, T.; Selinger, J. L.; Rochelle, G. T. "Demonstration of 99% CO_2 Removal from Coal Flue Gas by Amine Scrubbing." *Int. J. Greenh. Gas Control* 2019;83;236–244. https://doi.org/10.1016/j.ijggc.2019.02.013.

Gunasekaran P, Veawab A, Aroonwilas A. "Corrosivity of Single and Blended Amines in CO_2 Capture Process." *Energy Proc.* 2013;37;2094–2099. doi.org/10.1016/j.egypro.2013.06.088.

Gunasekaran P, Veawab A, Aroonwilas A. "Corrosivity of Amine-Based Absorbents for CO_2 Capture." *Energy Proc.* 2017;114;2047–2054. xdoi.org/10.1016/j.egypro.2017.03.1339.

Hackerman N, Makrides AC. "Action of Polar Organic Inhibitors." *Ind. Eng. Chem*. 1954;46;523–527.

Hjelmaas S, Storheim E, Flø NE, Thorjussen ES, Morken AK, Faramarzi L, deCazenove T, Hamborg ES. "Results from MEA Amine Plant Corrosion Processes at the CO_2 Technology Centre Mongstad." *Energy Proc.* 2017;114;1166–1178. doi.org/10.1016/j.egypro.2017.03.1280.

Hwang GS, Stowe HM, Paek E, Manogaran D. “Reaction Mechanisms of Aqueous Monoethanolamine with Carbon Dioxide: A Combined Quantum Chemical and Molecular Dynamics Study.” *Phys. Chem. Chem. Phys.* 2015;17;2;831–839. doi.org/10.1039/c4cp04518a.

Idem R, Wilson M, Tontiwachwuthikul P, Chakma A, Veawab A, Aroonwilas A, Gelowitz D. “Pilot Plant Studies Of The CO2 Capture Performance of Aqueous MEA and Mixed MEA/MDEA Solvents at The University of Regina CO_2 Capture Technology Development Plant and The Boundary Dam CO_2 Capture Demonstration Plant.” *Ind. Eng. Chem. Res.* 2006;45;2414–2420.

Ikeda A, Mukai S, Ueda M. “CO_2 Corrosion Behavior of Carbon and Cr Steels.” *Sumitomo Search* 1985;91–102.

IPCC. *Special Report on Global Warming of 1.5 °C*. 2018

Jung J, Jeong YS, Lim Y, Lee CS, Han C. “Advanced CO_2 Capture Process Using MEA Scrubbing: Configuration of a Split Flow and Phase Separation Heat Exchanger.” *Energy Proc*. 2013;37;1778–1784.

Kayafas I. “Technical Note: Corrosion Product Removal From Steel Fracture Surfaces for Metallographic Examination.” *CORROSION.* 1980;36;8;443-445. doi:10.5006/0010-9312-36.8.443

Khakharia P, Mertens J, Huizinga A, De Vroey S, Sanchez Fernandez E, Srinivasan S, Goetheer, E. “Online Corrosion Monitoring in a Postcombustion CO_2 Capture Pilot Plant and its Relation to Solvent Degradation and Ammonia Emissions.” *Ind Eng Chem Res.* 2015;54(19);5336–5344. doi:10.1021/acs.iecr.5b00729.

Kennedy G. “WA Parish Post-Combustion CO_2 Capture and Sequestration Demonstration Project Final Technical Report.” Petra Nova Power Holdings LLC. 2020.

Kohl A L, Nielsen R. *Gas Purification.* Elsevier. 1997.

Kittel J, Idem R, Gelowitz D, Tontiwachwuthikul P, Parrain G, Bonneau A. “Corrosion in MEA Units for CO_2 Capture: Pilot Plant Studies.” *Energy Proc.* 2009;1(1);791–797. doi:10.1016/j.egypro.2009.01.105.

Kittel J, Gonzalez S. “Corrosion in CO_2 Post-Combustion Capture with Alkanolamines – A Review.” *Oil Gas Sci. Technol.* 2014;69(5); 915–929.

Kladkaew N, Idem R, Tontiwachwuthikul P, Saiwan C. “Corrosion Behavior of Carbon Steel in The Monoethanolamine−H_2O−CO_2−O_2−SO_2 system.” *Ind. Eng. Chem. Res.* 2009a;48;8913–8919.

Kladkaew N, Idem R, Tontiwachwuthikul P, Saiwan C. “Corrosion Behavior of Carbon Steel in The Monoethanolamine−H_2O−CO_2−O_2−SO_2 System: Products, Reaction Pathways, and Kinetics.” *Ind. Eng. Chem. Res.* 2009b;48;10169–10179.

Lawal AO, Idem RO. “Kinetics of the Oxidative Degradation of CO_2 Loaded and Concentrated Aqueous MEA-MDEA Blends during CO_2 Absorption from Flue Gas Streams.” *Ind. Eng. Chem. Res.* 2006;45(8);2601-2607.

Le Moullec Y, Kanniche M. Screening of Flowsheet Modifications for an Efficient Monoethanolamine (MEA) Based Post-Combustion CO_2 Capture.” *Int. J. Greenh. Gas Control.* 2011;5;727–740.

Li W, Landon J, Irvin B, Zheng L, Ruh K, Kong L, Pelgen J, Link D, Figueroa JD, Thompson J. “Use of Carbon Steel for Construction of Post-Combustion CO_2 Capture Facilities: A Pilot-Scale Corrosion Study.” *Ind. Eng. Chem. Res.* 2017;56;16;4792–4803. doi.org/10.1021/acs.iecr.7b00697.

Lin Y-J, Rochelle GT. “Approaching a Reversible Stripping Process for CO_2 Capture.” *Chem. Eng. J.* 2016;283;1033–1043. doi.org/10.1016/j.cej.2015.08.086.

Liu C-T, Fischer KB, Rochelle GT. “Corrosion of Carbon Steel by Aqueous Piperazine Protected by $FeCO_3$.” *Int. J. Greenh. Gas Control* 2019;85;23–29. doi.org/10.1016/j.ijggc.2019.03.027.

Liu C-T, Fischer KB, Rochelle GT. “Corrosion by Aqueous Piperazine at 40–150 °C in Pilot Testing of CO_2 Capture.” *Ind Eng Chem Res.* 2020;59;7189–7197.

Mangalapally HP, Notz R, Hoch S, Asprion N, Sieder G, Garcia H, Hasse H. “Pilot Plant Experimental Studies of Post Combustion CO_2 Capture by Reactive Absorption with MEA and New Solvents.” *Energy Proc.* 2009;1;1;963–970.

McCafferty E, Hackerman N. “Double Layer Capacitance of Iron and Corrosion Inhibition with Polymethylene Diamines.” *J. Electrochem. Soc*. 1972;119;146–154.

Meuleman E, Artanto Y, Jansen J, Osborn M, Pearson P, Cottrell A, Feron P. “CO_2 Capture Performance of MEA and Blended Amine Solvents in CSIRO’s Pilot Plant with Flue Gas From a Brown Coal-fired Power Station.” 2010.

Metz B, Davidson O, de Coninck H, Loos M, Meyer LA. *IPCC Special Report on Carbon Dioxide Capture and Storage*, 1st Edition. Cambridge University Press, Cambridge, United Kingdom. 2005.

Moser P, Schmidt S, Uerlings R, Sieder G, Titz J-T, Hahn A, & Stoffregen T. “Material Testing for Future Commercial Post-Combustion Capture Plants – Results of the

Testing Programme Conducted at the Niederaussem Pilot Plant." *Energy Proc*. 2011;4;1317–1322. doi:10.1016/j.egypro.2011.01.189

NACE. "Preparation, Installation, Analysis, and Interpretation of Corrosion Coupons in Oilfiled Operations." In *SP0775-2013*. Houston, TX: NACE International, 2013.

Nešić S, L Lunde. "Carbon Dioxide Corrosion of Carbon Steel in Two-Phase Flow." Presented at the CORROSION 50. NACE International, 1994.

Nielsen PT, Li L, Rochelle GT. "Piperazine Degradation in Pilot Plants." *Energy Proc.* 2013;37;1912–1923.

Nielsen PT. *"Oxidation of Piperazine in Post-Combustion Carbon Capture.*" Ph.D. Dissertation, The University of Texas at Austin, TX, 2018.

Nyborg R. "Initiation and Growth of Mesa Corrosion Attack during CO_2 Corrosion of Carbon Steel." Presented at the CORROSION 98. NACE International, 1998.

Nyborg R, Dugstad A. "Mesa Corrosion Attack in Carbon Steel and 0.5% Chromium Steel." Presented at the CORROSION 98. NACE International, 1998.

Pacala S, Socolow R. "Stabilization Wedges: Solving the Climate Problem for the Next 50 Years with Current Technologies." *Science* 2004;305;5686;968–972. doi.org/10.1126/science.1100103.

Rochelle GT. "Amine Scrubbing for CO_2 Capture." *Science* 2009;325;5948;1652–1654. doi.org/10.1126/science.1176731.

Rochelle GT, Chen E, Freeman S, Van Wagener D, Xu Q, Voice A. "Aqueous Piperazine as the New Standard for CO_2 Capture Technology." *Chem. Eng. J.* 2011;171;725–733.

Rochelle GT, Wu Y, Chen E, Akinpelumi K, Fischer KB, Gao T, Liu C-T, Selinger JL. "Pilot Plant Demonstration of Piperazine with the Advanced Flash Stripper." *Int. J. Greenh. Gas Control* 2019;84;72–81. doi.org/10.1016/J.IJGGC.2019.03.014.

Rochelle GT, Akinpelumi K, Gao T, Liu C-T, Suresh A, Wu Y. "Pilot Plant Results with the Piperazine Advanced Stripper at NGCC Conditions." Presented at the 15th Greenhouse Gas Control Technologies Conference 15-18 March 2021 (GHGT-15).

Rooney PC, DuPart MS. "Effect of Heat Stable Salts on MDEA Solution Corrosivity." *Hydrocarb. Process*. 1997;76;4;65.

Preston C, Bruce C, Monea M. "An Update on the Integrated CCS Project at SaskPower's Boundary Dam Power Station." Presented at the14th Greenhouse Gas Control Technologies Conference Melbourne, 2018.

Ruzic V, Veidt M, Nešić S. “Protective Iron Carbonate Films—Part 1: Mechanical Removal in Single-Phase Aqueous Flow.” *CORROSION.* 2006;62;419–432.

Sadeek SA, Williams DR, Campbell KLS. “Using Sodium Thiosulphate for Carbon Steel Corrosion Protection against Monoethanolamine and Methyldiethanolamine.” *Int. J. Greenh. Gas Control*. 2018;74;206–218.

Schmitt G. "Fundamental Aspects of CO_2 Corrosion." *Advances in CO_2 Corrosion.* 1985a;1. NACE, Houston.

Schmitt G. "CO_2 Corrosion of Steels: An Attempt to Range Parameters and Their Effects." *Advances in CO_2 Corrosion.* 1985b;1. NACE, Houston.

Sharma SS, Fischer KB, Rochelle GT. “Fe^{2+} Solubility and Siderite Formation in Monoethanolamine and Piperazine Solvents.” Presented at the 14th International Conference on Greenhouse Gas Control Technologies, Melbourne, Australia, 21-25 October 2018.

Soosaiprakasam IR, Veawab A. “Corrosion and Polarization Behavior of Carbon Steel in MEA-Based CO_2 Capture Process.” *Int. J. Greenh. Gas Control.* 2008;2;553–562.

Soosaiprakasam IR, Veawab A. “Corrosion Inhibition Performance of Copper Carbonate in MEA–CO_2 Capture Unit.” *Energy Proc*. 2009;1;225–229.

Selinger JL. “Pilot Plant Modeling of Advanced Flash Stripper with Piperazine.” M. S. thesis, The University of Texas at Austin, Austin, TX, 2018.

Stec M, Tatarczuk A, Więcław-Solny L, Krótki A, Spietz T, Wilk A, Śpiewak D. “Demonstration of a Post-Combustion Carbon Capture Pilot Plant Using Amine-Based Solvents at the Łaziska Power Plant in Poland.” *Clean Technol. Environ. Policy.* 2018;18;151–160.

Sun W, Chokshi K, Nešić S, Gulino DA. “A Study of Protective Iron Carbonate Scale Formation in CO_2 Corrosion.” Presented at AIChE Annual Meeting, 2004.

Sun W, Nešić S, Woollam RC. “The Effect of Temperature and Ionic Strength on Iron Carbonate ($FeCO_3$) Solubility Limit.” *Corros. Sci.* 2009;5;6;1273–1276. doi.org/10.1016/j.corsci.2009.03.009.

Tanthapanichakoon W, Veawab A, McGarvey B. “Electrochemical Investigation on the Effect of Heat-Stable Salts on Corrosion in CO_2 Capture Plants Using Aqueous Solution of MEA.” *Ind. Eng. Chem. Res.* 2006;*45*;2586–2593. doi.org/10.1021/ie050575a.

Tomoe Y, Shimizu M, Kaneta H. “Active Dissolution and Natural Passivation of Carbon Steel in Carbon Dioxide-loaded Alkanolamine Solutions.” Presented at Corrosion 96, Houston, Texas, 1996.

Tomson MB, Johnson ML. “How Ferrous Carbonate Kinetics Impacts Oilfield Corrosion.” Presented at the SPE International Symposium on Oilfield Chemistry. Society of Petroleum Engineers, February 1991.

Uhlig HH, Revie RW. *Corrosion and Corrosion Control,* 3rd Ed. John Wiley & Sons, New York. 1985.

Veawab A, Tontiwachwuthikul P, Chakma A. “Influence of Process Parameters on Corrosion Behavior in a Sterically Hindered Amine-CO_2 System.” *Ind Eng Chem Res.* 1999;38(1);310–315.

Veawab A, Aroonwilas A. “Identification of Oxidizing Agents in Aqueous Amine-CO_2 Systems Using a Mechanistic Corrosion Model.” *Corros Sci.* 2002;44(5);967–987.

Veawab A, Tontiwachwuthikul P, Chakma A. “Investigation of Low-Toxic Organic Corrosion Inhibitors for CO_2 Separation Process Using Aqueous MEA Solvent.” *Ind. Eng. Chem. Res.* 2011;40;4771–4777.

Wagner R, Judd B. “Fundamentals – Gas Sweetening.” Proceedings of the 56th Laurance Reid Gas ConditioningConference, Norman, OK, 2006.

Wei L, Pang X, Gao K. “Effect of Flow Rate on Localized Corrosion of X70 Steel in Supercritical CO_2 Environments.” *Corros. Sci.* 2018;136;339–351.

Williams E, Leckie HP. “Corrosion and its Prevention in a Monoethanolamine Gas Treating Plant.” *Materials Protection.* 1968;7(7);321–326.

Wong HA, Kohler R, Kosseim AJ, Kubek DJ, McCullough JG. "Corrosion-inhibition System Passes Severest Test at Chevron's Princess MEA plant," *Oil Gas J.* 1985;11(83);100–108.

Wu, Y., Nielson, P.T., Rochelle, G.T., 2018. Oxidation of Piperazine in the Advanced Flash Stripper. Presented at the 14th Greenhouse Gas Control Technologies Conference, Melbourne, 21-26 October 2018 (GHGT-14).

Wu Y, Rochelle GT. “ Effects of Carbon Treating on Piperazine Oxidation in Pilot Plant Testing of PZAS™.” *Int. J. Greenh. Gas Control* 2021;112;4. doi.org/10.1016/j.ijggc.2021.103502

Xiang Y, Choi Y-S, Yang Y, Nešić S. “Corrosion of Carbon Steel in MDEA-Based CO_2 Capture Plants Under Regenerator Conditions: Effects of O_2 and Heat-Stable Salts.” *CORROSION.* 2014;71(1);30–37. doi:10.5006/1354.

Yang Y, Brown B, Nesic S, Elena Gennaro M, Molinas B. “Mechanical Strength and Removal of a Protective Iron Carbonate Layer Formed on Mild Steel in CO_2 Corrosion.” Presented at CORROSION 2010 Conference, 2010.

Yu LCY, Sedransk Campbell KL, Williams DR. Using Carbon Steel in the Stripper and Reboiler for Post-Combustion CO_2 Capture with Aqueous Amine Blends. *Int. J. of Greenh,.Gas Control.* 2016;51;380–393. doi:10.1016/j.ijggc.2016.04.031

Zheng L, Landon J, Zou W, Liu K. “Corrosion Benefits of Piperazine as an Alternative CO_2 Capture Solvent.” *Ind. Eng. Chem. Res.* 2014a;53;29;11740–11746. doi.org/10.1021/ie501346z.

Zheng L, Landon J, Matin NS, Li Z, Qi G, Liu, K. “Corrosion Behavior of Carbon Steel in Piperazine Solutions for Post-Combustion CO_2 Capture.” *ECS Trans.* 2014b;20;81–95.

Zheng L, Landon J, Matin NS, Thomas GA. Liu K. “Corrosion Mitigation via a pH Stabilization Method in Monoethanolamine-Based Solutions for Post-Combustion CO_2 capture.” *Corros. Sci.* 2016a;106;281–292. doi.org/10.1016/j.corsci.2016.02.013.

Zheng L, Matin NS, Landon J, Thomas GA, Liu K. “CO_2 Loading-Dependent Corrosion of Carbon Steel and Formation of Corrosion Products in Anoxic 30 wt.% Monoethanolamine-Based Solutions.” *Corros. Sci.* 2016b;102;44–54. doi.org/10.1016/j.corsci.2015.09.015.

Vita

Ching-Ting Liu was born and raised in Tainan, Taiwan. She attended National Tsing Hua University in Hsinchu, Taiwan and received her B.S. in Chemical Engineering. While there, she researched on synthesis of polybenzoxazine polymers and fabrication of electrospun membranes for oil-water separation under Dr. Ying-Ling Liu's supervision. After receiving her B.S., she began her graduate studies in Chemical Engineering under the supervision of Dr. Gary Rochelle at the University of Texas at Austin in 2017. Upon graduation, she will begin employment with Taiwan Semiconductor Manufacturing Company, Taiwan.

Permanent email: chingting.liu529@gmail.com

This dissertation was typed by Ching-Ting Liu.